# Comprehensively defining cellular specializations for initiating parallel auditory pathways in the mouse cochlear nucleus

Junzhan Jing[1, 2,*], Ming Hu[1, 2,*], Tenzin Ngodup[3,*], Qianqian Ma[1, 2], Shu Ning Natalie Lau[1, 2], Cecilia Ljungberg[1, 4], Matthew J. McGinley[1, 2], Laurence O. Trussell[3, †] and Xiaolong Jiang[1, 2, 5†]

## Summary

The cochlear nucleus (CN), the starting point for all central auditory processing, comprises a suite of neuronal cell types that are morphologically and biophysically specialized for initiating parallel pathways, yet their molecular distinctions are largely unknown. To determine how functional specialization is defined at the molecular level, we employed a single-nucleus RNA sequencing analysis of the mouse CN to molecularly define its constituent cell types and then related them to well-established cell types with classical approaches. We reveal a one-to-one correspondence between molecular cell types and all previously described major types, defining a cell-type taxonomy that meaningfully reconciles anatomical position, morphological, physiological, and molecular criteria. Our approach also yields continuous and/or discrete molecular distinctions within several major principal cell types that account for hitherto unresolved distinctions in their anatomical position, morphology, and physiology. This study thus provides a higher-resolution and thoroughly validated account of

[1]Jan and Dan Duncan Neurological Research Institute at Texas Children's Hospital, Houston, TX, USA.
[2]Department of Neuroscience, Baylor College of Medicine, Houston, TX, USA
[3]Oregon Hearing Research Center and Vollum Institute, Oregon Health and Science University, Portland, OR, USA
[4]Department of Pediatrics, Baylor College of Medicine, Houston, TX, USA
[5]Department of Ophthalmology, Baylor College of Medicine, Houston, TX, USA
*Equally contributed
[†]Correspondence to xiaolonj@bcm.edu, trussell@ohsu.edu

cellular heterogeneity and specializations in the CN from the molecular to the circuit level, opening a new window for genetic dissection of auditory processing and hearing disorders with unprecedented specificity.

**Keywords:** Cochlear nucleus, snRNA-seq, Patch-seq, phenotype, bushy cell, stellate cell, octopus cells, fusiform cells, interneurons, transcriptome.

## Introduction

The cell type is a fundamental concept in neuroscience. In the auditory system in particular, this concept assumes extreme importance. Prior to thalamocortical processing, auditory signals are refined through multiple, interacting brain regions, including the cochlear nuclei (CN), superior olive, lemniscal nuclei, and inferior colliculus. Within each region, distinct neuronal cell types with unique biophysical properties are linked to specific circuit functions, which in turn extract specific acoustic information (Oertel et al., 2009). Nowhere is this clearer than in the CN (Figure 1A), the first station for central auditory processing, where bushy, stellate, fusiform, and octopus cells each carry specific ascending signals needed for all high-level sound localization and identification (Palmer, 1987; Rhode and Greenberg, 1992; Yin et al., 2019). These cell types, and the interneurons that control their activity, have been defined through a variety of approaches, including classical Golgi stains, in vivo and in vitro recordings and cell labeling, and tracer studies of anatomical pathways. Despite these thoroughgoing explorations, our understanding of the function of cell types in the CN is limited. For example, given the high degree of convergence of information streams in the midbrain and beyond, the specific contribution of any given cell type in the CN to sound representations in the primary auditory cortex is unknown. Indeed, it is uncertain whether existing definitions of cell types are of sufficient resolution to account for the variety of anatomical projections and physiological responses observed in downstream circuits. In addition, we do not understand the molecular changes cell types undergo in response to hearing loss or other pathologies of peripheral hearing function. Thus, a much deeper level of understanding of CN cell types is needed, including a genetic "handle" on each cell type and a definitive census of all of the cell types.

Recent advance in single-cell RNA sequencing (scRNA-seq) offers a new approach to define cell types in the brain (Macosko et al., 2015; Saunders et al., 2018; Zheng et al., 2017), and large-scale efforts in this respect have provided a fairly exhaustive list of transcriptomically defined cell types in many brain regions (Callaway et al., 2021; Kozareva et al., 2021; Mickelsen et al., 2019; Tasic et al., 2018).

Despite this progress, one of the biggest challenges is to relate each transcriptomically defined cell type (the 'T-type') to the more classically-defined types described in the literature using accepted morphological and electrophysiological criteria (the 'ME-type'), and therefore to infer and explore their putative functions. While a match between T-types and ME-types is expected (Kozareva et al., 2021; Shekhar et al., 2016), a strict one-to-one correspondence across modalities appears to be rare (Gouwens et al., 2020; Parpaite et al., 2021; Scala et al., 2021). It remains to be determined if the incongruence across modalities is due to technical noise and analytical bias or reflects a true biological reality. For example, in many brain regions, there is still no consensus on the number of neuronal cell types defined with classical approaches, and it is unclear whether distinctions based on morphological, molecular, and physiological properties agree with each other (DeFelipe et al., 2013; Petilla Interneuron Nomenclature et al., 2008), and even the definition of the cell type is not clear in some areas (Campbell et al., 2017; Kim et al., 2019). The cochlear nucleus (CN) is one of a very few brain regions whose constituent cell types have been thoroughly studied and established with classical approaches and related to *in vivo* signals of known behavioral significance (Yin et al., 2019). Each CN cell type resides in a specific subregion and exhibits stereotypical morphological and electrophysiological properties, and thus could be discriminated with a high degree of confidence. Therefore, the CN is especially well suited to provide a template for examining the correspondence among distinct criteria and integrating functional, morphological, and molecular classification into a comprehensive classification scheme. We therefore employed unbiased single-nucleus RNA sequencing (snRNA-seq) analysis of CN to generate a transcriptomic taxonomy of cell types. To relate molecular cell types defined by transcriptomic profiling with known CN types, we used Patch-seq (Cadwell et al., 2016), previously described type-specific markers, and a validation method that combines fluorescent in situ hybridization (FISH) with transgenic mouse lines. Together, these approaches allowed us to match molecularly defined cell types with previously established CN cell types with one-to-one correspondence, defining a cell-type taxonomy that meaningfully reconciles

anatomical position, morphological, physiological, and molecular criteria. Importantly, we also find that transcriptomic classifications can be used to reveal hitherto unresolved distinctions in the morphology and physiology of cell types, indicating conventional categories may not be robust enough to account for true cellular heterogeneity (Gates et al., 1996; Hancock and Voigt, 2002). Many previous studies established a link between each CN cell type to a putative functional role in higher-level auditory processing including sound localization and identification (Yin et al., 2019), and defining these cell types by their molecular specializations thus permits the genetic dissection of auditory processing with unprecedented specificity.

## Results

### Identification of transcriptionally distinct cell populations in mouse cochlear nucleus

To investigate transcriptional and cellular heterogeneity within the cochlear nucleus (CN), we used the 10x Chromium platform to perform RNA sequencing on individual nuclei isolated from the CN of both male and female C57BL/6 mice (postnatal day (P) 22-28) (Figure S1A). Analysis of the sequence reads revealed on average ~4,000 uniquely detected transcripts from ~1,900 genes for each nucleus. After filtering out the doublets and the nuclei with limited numbers of detected genes as well as removing the nuclei from adjoining regions (Methods and Method S1), our dataset contained 61,211 nuclei from the CN. Following data integration, unsupervised dimensionality reduction techniques identified 14 major transcriptionally distinct cell populations (Figure S1B-C; Table S1). Calculation of the local inverse Simpson's index (Korsunsky et al., 2019) demonstrated that these populations were well mixed and contained cells from each sample, indicating successful integration (Data S1). Our analysis indicated few sex-dependent differences and the data from both sexes were thus pooled for subsequent analyses (Data S1).

By inspecting the expression of known markers we first identified all non-neuronal cell types in CN (Figure S1B-C; Table S1). Using pan-neuronal marker *Snap25*, we identified 31,639 neuronal nuclei

that expressed either vesicular glutamate transporters (*Slc17a7* or *Slc17a6*, encoding VGLUT1 and VGLUT2, respectively) or glycine transporters (*Slc6a5*, encoding glycine transporter 2, GlyT2), exhibiting a dichotomy based on the expression of genes necessary for the synthesis and packaging of glutamate and glycine (Figure S1B-C). Clustering analysis of the neuronal nuclei resulted in 13 major molecularly distinct populations including seven glutamatergic/excitatory clusters (*Slc17a7*$^+$ and or *Slc17a6*$^+$) and six glycinergic/inhibitory clusters (*Slc6a5*$^+$, Figure 1B). By inspecting the expression of known markers we were able to assign some of these neuronal clusters to known CN cell types. Among the glutamatergic clusters is a large cluster enriched with *Gabra6*, a marker gene for granule cells (GCs) in the CN and cerebellum (Campos et al., 2001; Kato, 1990; Varecka et al., 1994), thus corresponding to GCs in CN (Figures 1B-C, S1D). The GC population is one of two glutamatergic clusters that express only *Slc17a7*, while other excitatory clusters either express both *Slc17a7* and *Slc17a6* or only *Slc17a6* (Figure 1B-C). Another *Slc17a7*$^+$ only cluster is specified by a high expression of *Tbr2*/*Eomes* (encoding eomesodermin, Figure 1B-C), a canonical gene marker for unipolar brush cells (UBCs) in the brain (Englund et al., 2006; Kozareva et al., 2021), and thus corresponds to UBCs in the dorsal cochlear nucleus (DCN). This cluster was also characterized by the graded and inversely correlated expression of excitatory metabotropic glutamate receptor 1 (mGluR1) and inhibitory mGluR2/3 pathways enriched in ON-UBCs and OFF-UBCs respectively (Figure S1F), further substantiating this cluster as UBCs from the CN (Borges-Merjane and Trussell, 2015; Guo et al., 2021; Kozareva et al., 2021). Differentially expressed gene (DEG) analysis identified *Smad3* (encoding sterile alpha motif domain-containing protein 3) as another specific marker gene for UBCs in the CN (Figure 1B-C), which was validated with RNA fluorescent in situ hybridization (FISH) staining (Figure S1D). Surprisingly, *Grm2* (encoding mGluR2), a marker gene used to label all UBCs (Borges-Merjane and Trussell, 2015; Watanabe et al., 1998), did not have a strong expression in our

UBC cluster, yet was enriched in one of six glycinergic clusters. This *Grm2*$^{+}$ glycinergic cluster corresponds to Golgi cells in CN granule cell regions (Figures 1B-C, S1E), as Golgi cells are the only

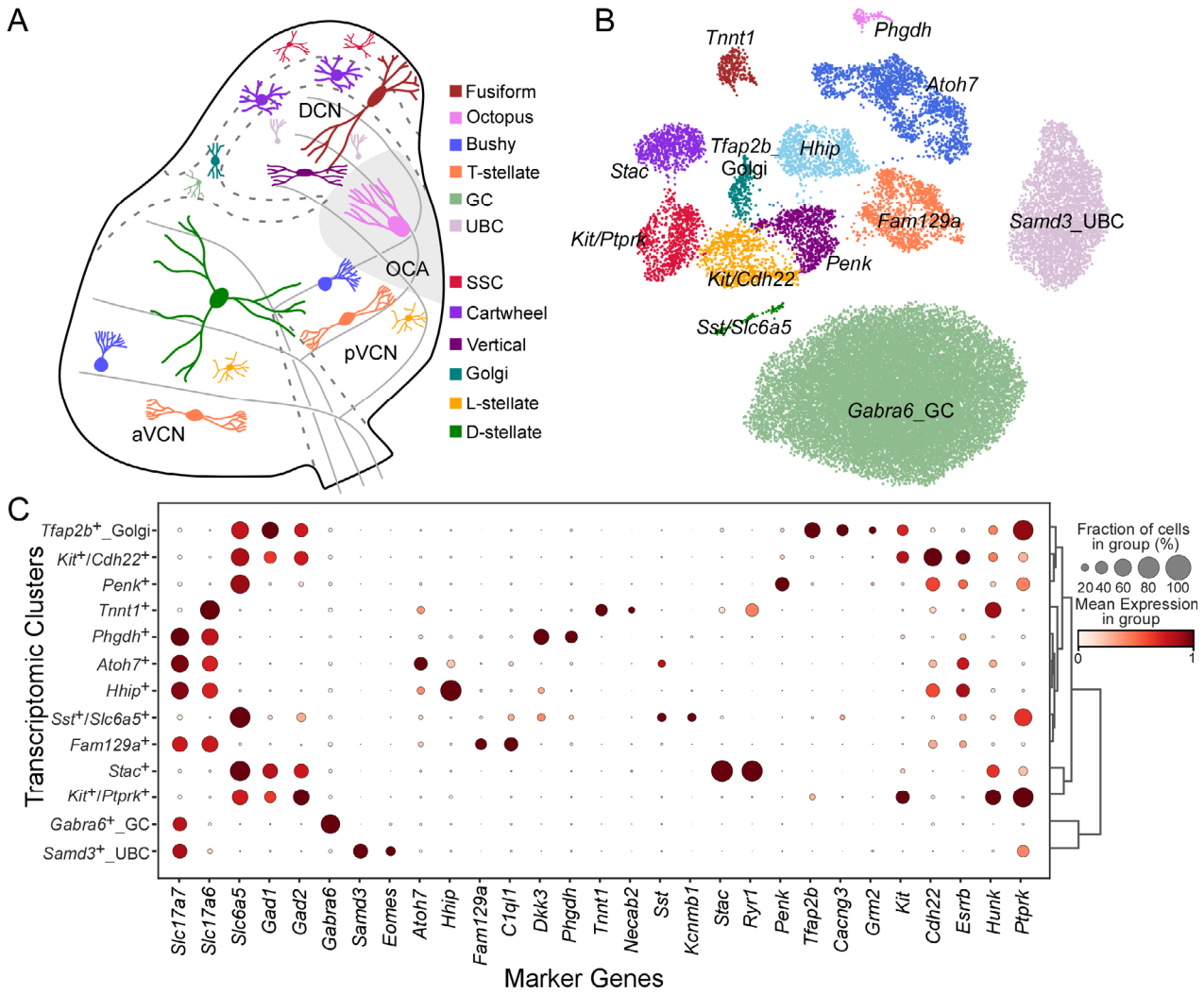


**Figure 1. Comprehensive transcriptional profiling of cell types across the mouse cochlear nucleus (CN).** (**A**) Cartoon depiction of distinct neuronal cell types across the subregions of the mouse cochlear nucleus (CN), colored by cell type identity. (**B**) UMAP visualization of 31,639 nuclei from the CN neurons clustered by the over-dispersed genes, colored by cluster identity. Each cluster is labeled by one or two marker genes. **(C)** Dendrogram indicating hierarchical relationships between clusters (right) with a dot plot (left) of scaled expression of selected marker genes for each cluster shown in (**B**); also see Table S1. The size of each circle depicts the percentage of cells in the cluster in which the marker was detected (≥ 1 UMI), and its color depicts the average transcript count in expressing cells (nTrans). See Figure S1 and Data S1 for more technical details and annotations.

inhibitory CN cell type expressing mGluR2 (Irie et al., 2006; Yaeger and Trussell, 2015). Further DEG analysis identified and validated with FISH staining *Cacng3* and *Tfap2b* as more specific marker genes for auditory Golgi cells (Figures 1B-C, S1E).

The other major clusters we identified were unknown in terms of their potential correspondence to well-studied CN cell types (Figure 1A) and thus required further analysis (see below). We tentatively labeled them based on candidate marker expression (Figure 1B-C; Table S1), though some lacked a

unique marker and were annotated instead by a combination of markers. Five unknown excitatory clusters include a cluster marked by high levels of *Hhip* (encoding hedgehog interacting protein, *Hhip*$^+$ cluster), a cluster marked by *Atoh7* (encoding atonal homolog BHLH transcription factor 7, *Atoh7*$^+$ cluster), a cluster marked *by Fam129a* (encoding niban apoptosis regulator 1, *Fam129a*$^+$ cluster), a cluster marked by *Tnnt1* (encoding troponin T1, *Tnnt1*$^+$ cluster), and a cluster marked by *Phgdh* (encoding phosphoglycerate dehydrogenase, *Phgdh*$^+$ cluster). Five unknown glycinergic clusters include a cluster marked by high levels of *Stac* (encoding SH3 and cysteine-rich domain-containing protein, *Stac*$^+$ cluster), and a cluster marked by *Penk* (encoding proenkephalin, *Penk*$^+$ cluster). The other three glycinergic clusters lack a unique marker but could be annotated with a combination of two genes, including a small cluster labeled by *Sst* (*Sst*$^+$/*Slc6a5*$^+$) and two larger clusters labeled by *Kit* (encoding tyrosine-protein kinase Kit, *Kit*$^+$/*Ptprk*$^+$ *and Kit*$^+$/*Cdh22*$^+$). Each cluster could be discriminated with additional marker genes (Table S1).

Among six glycinergic/inhibitory clusters, four clusters (including the Golgi cell cluster) expressed both *Slc6a5* and *Gad1/2* (encoding GABA synthetic enzymes; Figure 1C), consistent with the contention that many CN inhibitory populations are capable of co-release or co-synthesis of glycine and GABA (Apostolides and Trussell, 2014; Golding and Oertel, 1997; Kolston et al., 1992; Yaeger and Trussell, 2015). Each of these glycine/GABA combinatorial clusters expressed both GABA synthetic enzyme genes *Gad1* (encoding GAD67) and *Gad2* (encoding GAD65), an expression pattern similar to cortical GABAergic interneurons rather than many subcortical GABAergic neurons (Blum et al., 2021; Kim et al., 2019; Phillips et al., 2022). The other two glycinergic clusters, *Slc6a5*$^+$/*Sst*$^+$ and *Penk*$^+$ clusters, expressed only *Slc6a5* (Figure 1C), indicating that they are pure glycinergic populations. The *Slc6a5*$^+$/*Sst*$^+$ cluster may correspond to D-stellate cells in the ventral cochlear nucleus (VCN), as D-stellate cells are a pure glycinergic population with specific expression of *Sst* (Kolston et al., 1992; Ngodup et al., 2020). The *Penk*$^+$ cluster may correspond to vertical cells (also known as tuberculoventral cells) in the DCN, as vertical cells are another pure glycinergic population in CN

(Saint Marie et al., 1991; Wickesberg and Oertel, 1990). To further examine these correspondences and to explore the relationship between other "mystery" clusters with well-established cell types in CN with accepted morpho-electric criteria (ME-types) (Rhode and Greenberg, 1992), we performed Patch-seq across all CN sub-regions to link the transcriptome of each neuron to their morpho-electric properties (Cadwell et al., 2016).

**Annotation of transcriptomic excitatory cell types**

The VCN contains three known excitatory projection neuronal populations including bushy cells, T-stellate cells and octopus cells, the DCN contains two excitatory cell types, fusiform cells and giant cells, while a broad granule domain houses excitatory interneurons including GCs and UBCs (Figure 1A) (Rhode and Greenberg, 1992). To perform Patch-seq on these excitatory cell types, we targeted each of them (except for GC, UBC and giant cells) via their known anatomical location aided by transgenic mouse lines for patch-clamp recording (see Methods). Their characteristic electrophysiological responses to current injections were recorded, cytosol and nucleus mRNA was then extracted and reverse transcribed, and the resulting cDNA was sequenced (Data S1, Methods). The morphology of each neuron was post hoc recovered and reconstructed.

In addition to the difference in anatomical locations, each excitatory CN cell type exhibits stereotypical morpho-electric properties (Figures 1A, 2A-B; Table S2), allowing experienced patch clampers to assign each recorded neuron to a cell type with high confidence (Manis et al., 2019). To validate this expert classification and support cell-type assignment of each Patch-seq neuron, we extracted electrophysiological and morphological features from each Patch-seq neuron (for morphological feature extraction, only cells with a sufficient morphological recovery were included), and an additional set of neurons from regular patch-clamp recordings were also included in the same analysis (Figure 2C-D, Table S2). We trained a random forest classifier to distinguish between any two types of CN excitatory neurons as labeled manually based on either electrophysiology or morphology (Figures

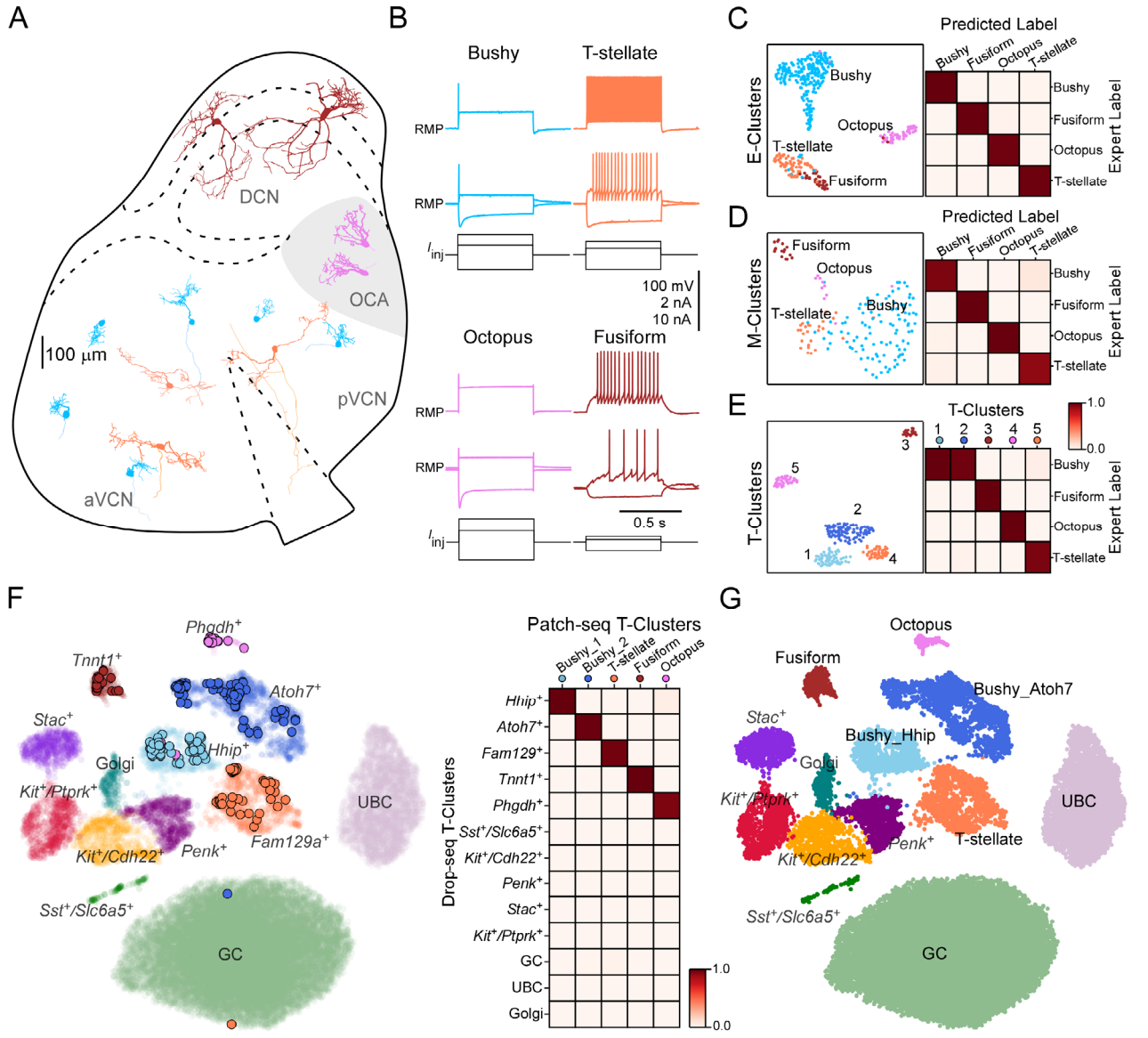


**Figure 2. Using Patch-seq to relate transcriptomically defined cell types (T-type) to the ME-types in CN**. (**A**) Representative morphology of each cell type in distinct subregions of the mouse CN (a sagittal view), colored by the cell type identity. Dendrites are in darker colors than axons. (**B**) Example membrane responses of different CN excitatory cell types to current steps. The bottom traces show the injected currents. Scale bar, vertical 100 mV for the potential, 2 nA for the injected currents for all cells except for octopus cells, and 10 nA for octopus cells only. (**C**) Left: UMAP visualization of 404 CN excitatory neurons clustered by select electrophysiological features (E-cluster), colored by the expert cell type. n = 243 for Bushy, n = 67 for T-stellate, n = 58 for Octopus, n = 36 for Fusiform. Right: Confusion matrix shows the performance (an average of 99.2% accuracy) by the cell-type classifier trained with electrophysiological features. (**D**) Left: UMAP visualization of 157 CN excitatory neurons clustered by select morphological features (M-cluster), colored by the expert cell type. n = 105 for Bushy, n = 16 for T-stellate, n = 10 for Octopus, n = 26 for Fusiform. Right: Confusion matrix shows the performance (an average of 95.5% accuracy) by the classifier trained with morphological features. (**E**) Left: UMAP visualization of 293 Patch-seq samples from excitatory neurons clustered by the over-dispersed genes, colored by the transcriptomic cluster (T-cluster). Right: the matrix shows the proportion of Patch-seq cells assigned to a specific cell type (the expert classification) in each T-cluster. All cells in T-cluster 1 (n= 67/67, 100%) and almost all cells in T-cluster 2 (n = 111/113: 98.2%) are bushy cells; All cells in T-cluster 3 are fusiform cells (n = 22/22: 100%); All cells in T-cluster 4 are octopus cells (n = 43/43: 100%); Almost all cells in T-cluster 5 are T-stellate cells (n = 46/48: 95.8%). (**F**) Left: Patch-seq cells (n = 187) mapped to the UMAP space of 31,639 sequenced neuronal nuclei as shown in Figure 1B (13 clusters). Right: The matrix shows the proportion of Patch-seq cells assigned to each T-cluster in (**E**) mapped to one of 13 distinct clusters in the UMAP space. (**G**) Annotation of each molecular excitatory cell type with well-studied ME-types in the mouse CN. See Data S2 for more details.

2C-D, Data S2). The classifier could separate almost all cell type pairs by either electrophysiology (Figure 2C, right) or by morphology (Figure 2D, right), supporting our expert manual classification. In

addition, clustering analysis using either set of properties indicated the cells labeled as the same type clustered together with very few cells confused with other cell types (Figure 2C-D, left; Data S2), further supporting the expert classification. To note, the classification performance was better by physiological features than by morphological features, with no single cell from one cell type confused with other cell types (Figures 2C, Data S2). This analysis indicates the physiology alone can be used as a reliable criterion to distinguish these major excitatory neurons, allowing us to assign those Patch-seq samples with poor-quality (or no) morphology to a cell type with high confidence. In total, we had 180 Patch-seq cells assigned as bushy cells, 48 as T-stellate cells, 43 as octopus cells, and 22 as fusiform cells. UMAP projection of these Patch-seq cells resulted in six transcriptomic clusters, and the cells labeled as the same type clustered together with few confused with another cluster (Figure 2E), except for bushy cells, which fall into the two clusters. This analysis indicates there is a high degree of congruence across three modalities in CN excitatory neuron classification, but also reveals molecular heterogeneity among bushy cells. Using the gene expression profiles, we then mapped these Patch-seq neurons to the transcriptomic clusters (the T-types) identified via snRNA-seq (Figure 1B), following the same method as we used previously (Cadwell et al., 2020; Scala et al., 2018). All Patch-seq cells labeled as fusiform cells were mapped to the *Tnnt1*$^{+}$ cluster (22/22 cells = 100.00%), strongly suggesting that this cluster corresponds to fusiform cells (Figure 2F-G). Almost all cells labeled as octopus cells were mapped to the *Phgdh*$^{+}$ cluster (41/43 cells = 95.35%), which thus corresponds to octopus cells (Figure 2F-G). Almost all T-stellate cells were mapped to *Fam129a*$^{+}$ cluster (47/48 cells = 97.9%), suggesting this is the T-stellate cell cluster (Figure 2F-G). All Patch-seq bushy cells were mapped to one of two clusters, the *Hhip*$^{+}$ cluster and the *Atoh7*$^{+}$ cluster (Figure 2F-G). Importantly, those Patch-seq bushy cells clustering together as Cluster 1 in Patch-seq UMAP space (Figure 2E) were all mapped to the *Hhip*$^{+}$ cluster (67/67 cells = 100.0%), while almost all bushy cells in Cluster 2 (Figure 2E) were mapped to the *Atoh7*$^{+}$ cluster (112/113 cells = 99.1%). This analysis indicates that the bushy cell population is composed of two molecularly distinct subpopulations (also see below).

To substantiate the molecular correspondence for each cell type, we performed DEG analysis to find the putative marker genes for each cell cluster (Table S1), and then used a two-color RNA fluorescent in situ hybridization (FISH) protocol to label all CN regions with identified gene transcripts and confirmed that patterns of labeled somata across the whole CN were consistent with the location of previously established cell types (Methods). A suite of discriminatory markers was identified for the *Phgdh* cluster (octopus cells) including *Phgdh, Dkk3, Ass1, Efemp1, Ano1, Col5a3, Egflam, Prima1*, suggesting novel marker genes for octopus cells (Figures 3A, S2 and Table S1), a group of unique projection neurons restricted to the most posterior part of VCN and specialized for detecting rapid sequences of auditory inputs (Lu et al., 2022; McGinley et al., 2012). In line with our analysis, FISH *Phgdh* signals largely overlapped with *Slc17a6* signals (i.e., expressed in excitatory neurons), and *Phgdh*$^+$ neurons (i.e., *Phgdh*$^+$/*Slc17a6*$^+$ cells) were exclusively restricted to the octopus cell area (OCA) of the CN (Figure 3B, Data S3). In addition, Phgdh-immunopositive cells with a large soma (i.e., neurons) were restricted to the OCA (Figure S3C1), further substantiating *Phgdh* as a novel marker for octopus cells. Finally, we performed patch-clamp recordings from the OCA to label octopus cells with biocytin and perform *post hoc* immunohistochemistry for Phgdh, and the vast majority of labeled cells (~92%, 12 out of 13 neurons) were immunopositive for Phgdh, indicating this novel maker gene labels almost the entire population of octopus cells (Figure 3C). With FISH, we also validated *Dkk3, Ass1* and *Efemp1* as additional marker genes for octopus cells, each of which exhibits a slight selectivity difference (Figures 3B, S2D, S3A, Data S3). Taken together, we confirmed that octopus cells, a morphologically and biophysically specialized cell population in CN, are transcriptomically distinct and can be distinguished by the molecular specialization.

To confirm the molecular correspondence for fusiform cells, we identified a list of discriminatory genes for the *Tnnt1* cluster including *Necab2, Ppfibp1, Tnnt1, Net1, Drd3, Nts, Gfra1, Gpc3, Adad2, Kcna4, Htr1b, Irx2, Plxdc1* (Figures 3D, S2B and Table S1). In line with our analysis, the patterns of

labeled neurons with *Necab2*, *Ppfibp1*, *Net1*, *Nts*, *Drd3*, or *Gfra1* signals across the CN were all

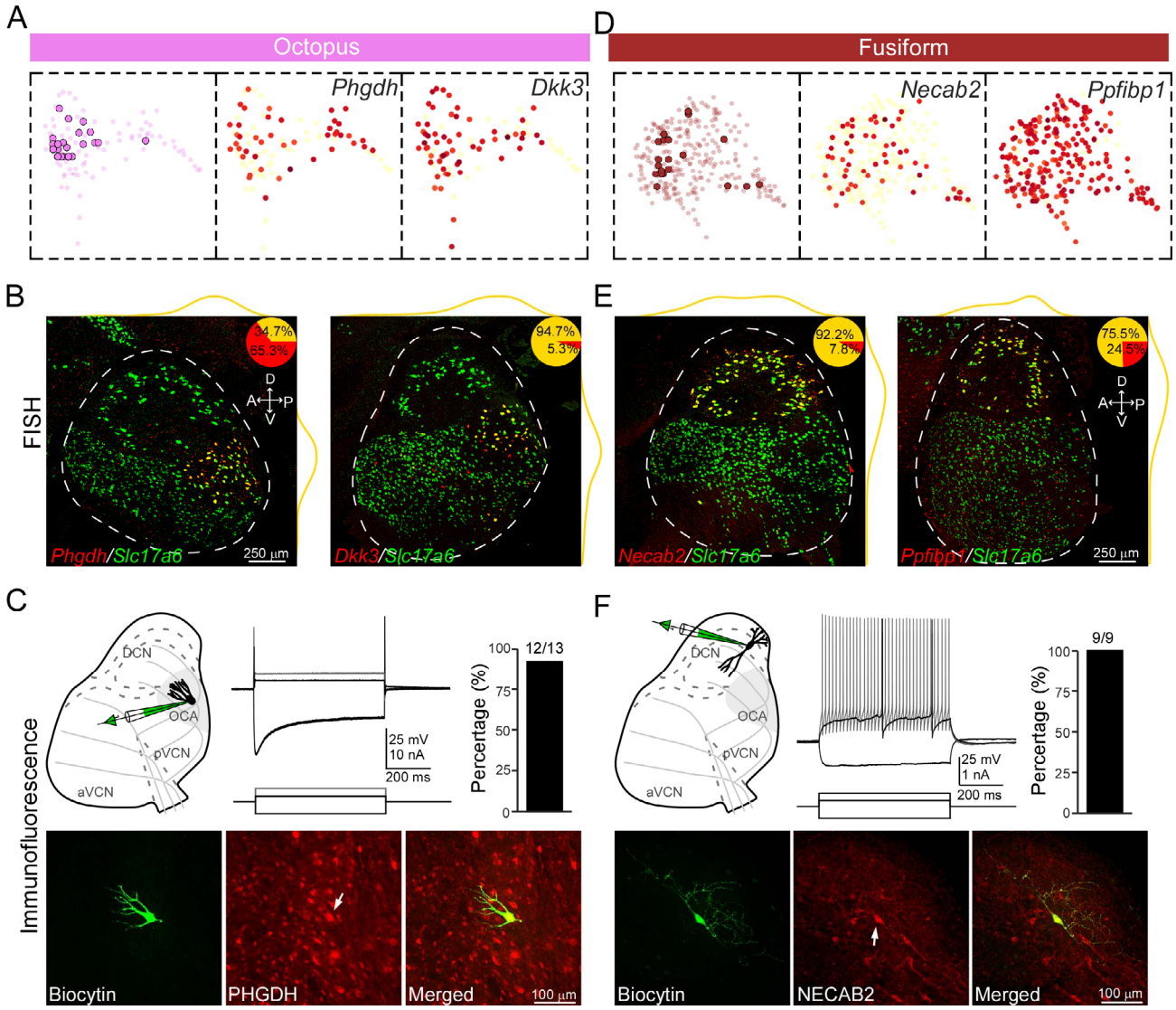


**Figure 3**. **Novel marker genes for excitatory neuronal cell types in CN.** (**A**) Left: UMAP visualization of all neurons in the *Phgdh*$^+$ cluster (n = 88) and all Patch-seq cells assigned to octopus cells positioned on the UMAP space. Middle and Right: UMAP visualization of the normalized expression of discriminatory markers for octopus cell cluster (*Phgdh* in the middle, *Dkk3* on the left). **(B)** FISH co-staining for *Slc17a6* and *Phgdh* (left), or *Slc17a6* and *Dkk3* (right) in sagittal sections of the CN. D, dorsal; V, ventral; A, anterior; M, posterior. Inset pie charts show the percentage of double-labeled cells (*Phgdh*$^+$/*Slc17a6*$^+$ or *Dkk3*$^+$/*Slc17a6*$^+$) in single-labeled cells (*Phgdh*$^+$ or *Dkk3*$^+$). Yellow lines along FISH images show the density of double-labeled neurons (yellow) along two axis of the CN. **(C)** Top left: a diagram showing patch recording and labeling with biocytin for octopus cells. Top middle: example membrane responses of an octopus cell to current steps. Scale bar, vertical 25 mV for the potential, 10 nA for the injected currents. Top right: the proportion of octopus cells immunopositive for Phgdh. Bottom: one example octopus cell filled with biocytin (green) shows positive signals for Phgdh (red). **(D)** Left: UMAP visualization of all neurons in the *Tnnt1*$^+$ cluster (n = 274) and all Patch-seq cells assigned to fusiform cells positioned on the UMAP space. Middle and Right: UMAP visualization of the normalized expression of discriminatory markers for fusiform cells (*Necab2* on the middle, *Ppfibp1* on the left). **(E)** FISH co-staining for *Slc17a6* and *Necab2* (left), or *Slc17a6* and *Ppfibp1* (right) in CN sagittal sections. Inset pie charts show the proportion of double-labeled cells (*Necab2*$^+$/*Slc17a6*$^+$ or *Ppfibp1*$^+$/*Slc17a6*$^+$) in single-labeled cells (*Necab2*$^+$ or *Ppfibp1*$^+$). Yellow lines along FISH images show the density of double-labeled neurons (yellow) along two axis of the CN. **(F)** Top left: a diagram showing patch recording and labeling with biocytin for fusiform cells. Top middle: example membrane responses of a fusiform cell to current steps. Scale bar, vertical 25 mV for the potential, 1 nA for the injected currents. Top right: The proportion of fusiform cells immunopositive for Necab2. Bottom: One example fusiform neuron filled with biocytin (green) shows positive signals for Necab2 (red).

consistent with the location of fusiform cells (i.e., the pyramidal cell layer of DCN) (Figures 3E, S2D, S3B1-3, S3B5 and Data S3), confirming the molecular correspondence established by our Patch-seq

analysis and validating novel maker genes for fusiform cells. Immunostaining for Necab2 provided translation-level evidence for *Necab2* as a highly selective marker (Figure S3C2). Importantly, this gene can label the entire population of fusiform cells, as all fusiform cells identified via patch-clamp recordings (100%, 9 out of 9) were immunopositive for Necab2 (Figure 3F). To note, *Tnnt1* is another highly selective marker gene predicted by our snRNA-seq (Figure S2D), but FISH staining appears to label additional neuronal populations in the VCN (Figure S3B4), inconsistent with our snRNA-seq data. This might reflect a developmental-dependent expression pattern, as *Tnnt1* expression appears to be exclusively restricted to the pyramidal cell layer of DCN at adult ages (Data S3).

**Two transcriptomic subtypes for bushy cells**

Patch-seq analysis identified two transcriptomically distinct bushy cell populations (*Atho7*$^+$ and *Hhip*$^+$), which may correspond to spherical and globular bushy cells (SBCs and GBCs, respectively), a conventional classification of bushy cells (Yin et al., 2019). To explore this correspondence and validate the marker genes for two molecular subtypes (Table S1), we performed RNA FISH staining for *Atoh7* and *Hhip*, two discriminatory genes for the subtypes. Given that *Sst* is specifically expressed in the *Atoh7* subtype rather than the *Hhip* subtype (Figure 4B) and may be expressed preferentially in SBCs rather than GBCs in the VCN (Romero, 2021), we also performed FISH co-staining for *Sst* and *Atoh7*, and for *Sst* and *Hhip*. Both *Atoh7* and *Hhip* signals were almost exclusively detected in excitatory neurons and were restricted to the VCN (Figure 4C), in line with our snRNA-seq data (Figure S2A-B, S2D) and Allen ISH data (Data S3). Furthermore, *Atoh7*$^+$ neurons were predominantly localized in the rostral AVCN, while *Hhip*$^+$ neurons densely populated the PVCN and caudal AVCN, and less so rostrally (Figure 4C), reminiscent of SBCs and GBCs in terms of their typical locations (Lauer et al., 2013; Martin, 1981; Webster and Trune, 1982). In addition, *Sst* signals mostly overlapped with *Atoh7* with much less overlapping with *Hhip*, and the double-labeled cells (*Sst*$^+$/*Atoh7*$^+$and *Sst*$^+$/*Hhip*$^+$) were restricted to the rostral AVCN (Figure 4C), further validating two molecularly

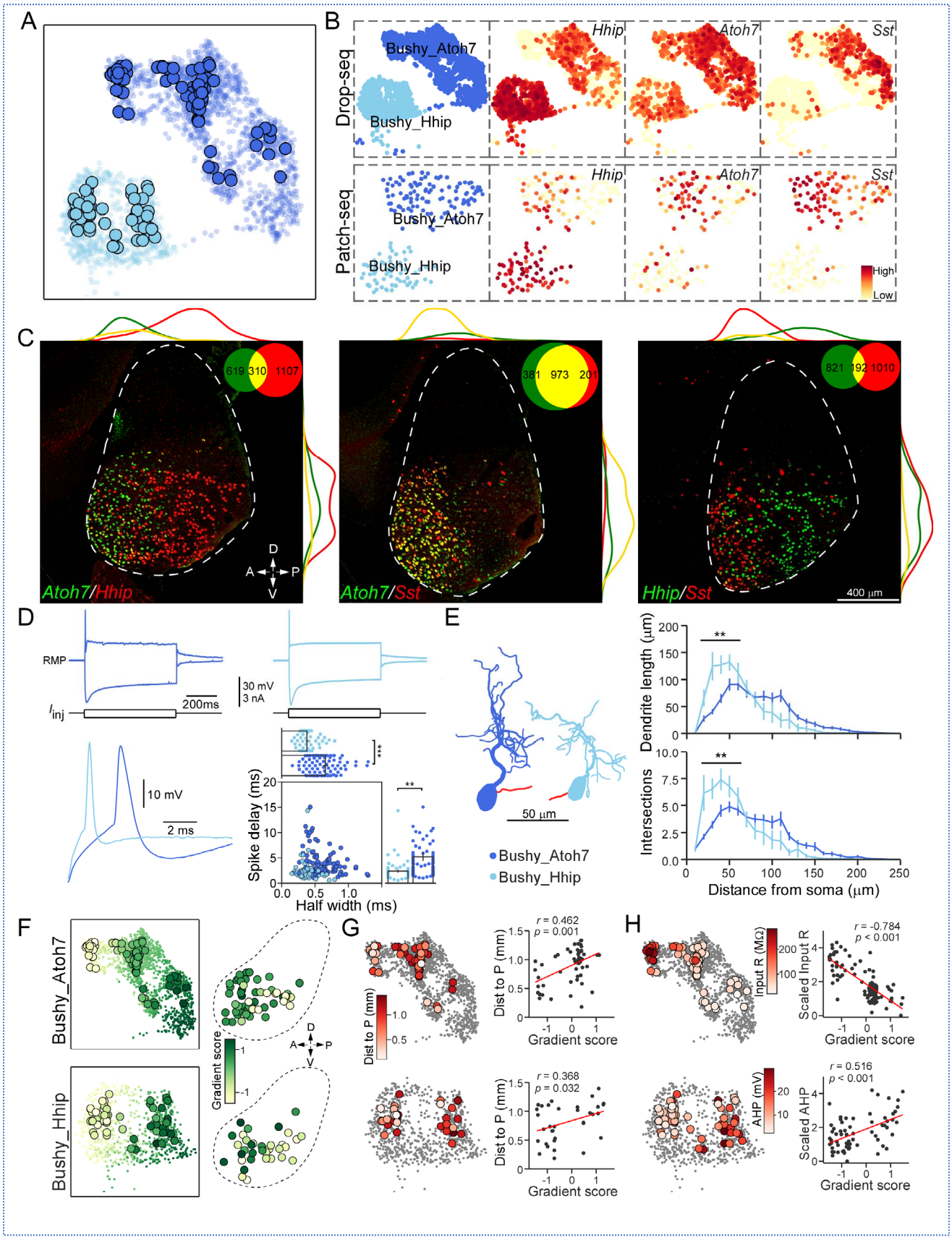


distinct bushy cell subtypes marked with the expression level of *Atoh7* or *Hhip*. Based on the preferential location of each molecular subtype with their differential *Sst* expression, the *Atoh7* subtype

**Figure 4. Two distinct molecular cell types of bushy cells**. (**A)** UMAP visualization of *Hhip*$^+$ and *Atoh7*$^+$ clusters and the distribution of the Patch-seq cells assigned to bushy cells in the UMAP space, colored by the cluster. (**B**) Top row: UMAP visualization of two bushy cell clusters (snRNA-seq) and normalized expression of their marker genes, *Hhip*, *Atoh7,* and *Sst*. Bottom row: UMAP visualization of Patch-seq cells assigned to bushy cells and normalized expression of the marker genes, *Hhip*, *Atoh7,* and *Sst*. All Patch-seq cells mapped to the *Hhip*$^+$ cluster (colored by light blue) cluster together and are separated from cells mapped to the *Atoh7*$^+$ cluster (colored by dark blue). (**C)** FISH co-staining for *Atoh7* and *Hhip* (left), *Atoh7* and *Sst* (middle), or *Hhip* and *Sst* (right) in CN representative sagittal sections. Insets show the total number of single-labeled cells and double-labeled cells. The lines along FISH images show the density of single-labeled or double-labeled cells along the two axis of the CN. The scale bar applies to all images. **(D)** Top: example membrane responses of a Patch-seq cell assigned to *Atoh7*$^+$ bushy cell (left, dark blue) or *Hhip*$^+$ bushy cell (right, light blue) to a hyperpolarized current step and a near-threshold depolarizing current step ($I_{inj}$). Scale bar: Vertical 5 nA for current injections ($I_{inj}$), 50 mV for membrane potentials. Bottom left: individual APs from the *Hhip*$^+$ and *Atoh7*$^+$ bushy cells (as shown on the top) aligned with respect to the onset of depolarizing current injections. Bottom right: two most discriminating electrophysiological features for *Hhip*$^+$ bushy cells and *Atoh7*$^+$ bushy cells, spike delay and spike duration (half-width). Plotting spike delay against the half-width separates the majority of *Hhip*$^+$ bushy cells from *Atoh7*$^+$ bushy cells. $^{**}p < 0.01$; $^{***}p < 0.001$ with the T-test. (**E)** Left: A representative morphology of the *Hhip*$^+$ or *Atoh7*$^+$ bushy cell. The dendrite and soma in blue and the axon in red. The axon is shown only partially. Right: Sholl analysis of dendritic arbors of *Hhip*$^+$ or *Atoh7*$^+$ bushy cells. Top: length; Bottom: intersection. $^{**}p < 0.01$, with two-way mixed model ANOVA. (**F)** Left: Patch-seq bush cells mapped to the *Atoh7*$^+$ (top) or *Hhip*$^+$ (bottom) cluster, colored by the RNA gradient score (see Methods). Right: 2D spatial projection of each Patch-seq cell assigned to *Hhip*$^+$ or *Atoh7*$^+$ bushy cells to a representative sagittal view of the CN, colored by gradient score. (**G)** Left: Patch-seq bushy cells mapped to the *Atoh7*$^+$ (top) or the *Hhip*$^+$ (bottom) cluster, colored by their distance to the posterior edge of the CN (the farther away from the posterior, the darker the color red). Right: Correlation between gradient score and the distance to the posterior edge (P). **(H)** Left: Patch-seq bushy cells mapped to the *Atoh7*$^+$ (top) or *Hhip*$^+$ (bottom) cluster, colored by their select electrophysiological features (input resistance for *Atoh7*$^+$ bushy cells; AHP for *Hhip*$^+$ bushy cells). Right: Correlation between gradient score with the selected electrophysiological features. See Figure S4 for more electrophysiological features.

may correspond to SBCs, while the *Hhip* subtype may correspond to GBCs.

To further explore this correspondence, we examined the properties of each Patch-seq cell that was assigned to the *Atoh7* or *Hhip* subtype. The electrophysiological characteristics of the two molecular subtypes showed numerous distinctions. *Hhip* bushy cells tended to fire few action potentials followed by a flat depolarization and responded to hyperpolarizing currents with deep sags, whereas *Atoh7* bushy cells were more likely to fire more action potentials and have slower and shallower sags (Figure 4D and Table S3). In addition, *Hhip* bushy cells tended to have lower input resistances and shorter membrane time constant than *Atoh7* bushy cells, as well as faster depolarization and repolarizations (larger dV/dt) resulting in a shorter delay in onset of firing and a narrower spike (Figure 4D and Table S3). UMAP embedding of bushy cells based on the electrophysiological features indicated that the two subtypes were largely non-overlapping (Figure S5A), with spike delay and half-width as the two most discerning features (Figure 4D). Such differences between *Hhip* cells and *Atoh7* cells are similar to the electrophysiological differences between GBC-like bushy cells recorded near the root of the auditory nerves and SBC-like bushy cells recorded somewhat more dorsally in mice (Cao and Oertel, 2010; Cao et al., 2007). As for their synaptic inputs, *Hhip* cells tended to receive fewer spontaneous excitatory

synaptic events but more inhibitory synaptic events than *Atoh7* cells with no significant differences in characteristics of either excitatory or inhibitory events (Figure S4A-B).

We examined the location of each Patch-seq bushy cell in the brain slice and found that, consistent with FISH data, *Atoh7* bushy cells were predominantly localized in the rostral AVCN, while more *Hhip* bushy cells were located dorsally in the VCN. We then examined the morphology of each Patch-seq cell assigned to either *Atoh7* bushy cells or *Hhip* bushy cells. Interestingly, there was no significant difference in any parameters gauging the soma size and shape between *Hhip* neurons and *Atoh7* neurons (Table S3). Both subtypes exhibited typical "bushy-like" dendritic morphology, but there were differences in their dendritic arborization (Figure 4E and Table S3). While the majority of *Hhip* bushy cells have only one primary dendrite (85%, 17 out of 20 cells), more than half of *Atoh7* bushy cells have two or even three primary dendrites (~53%, 27 out of 51 cells), each with its own secondary and filamentous branches (Table S3). In addition, *Hhip* bushy cells had short dendritic trunks capped with relatively compact dendritic tufts, while *Atoh7* bushy cells had longer dendritic trunks that bifurcated and sent off diffuse, thin dendritic processes (Figure 4E and Table S3). Dendrites of either *Atoh7* bushy cells or *Hhip* bushy cells were not oriented in any particular direction within the VCN.

**Continuous variation within bushy cells**

Subclustering analysis revealed distinct subpopulations within each of two bushy cell subtypes, including two subpopulations in *Hhip*$^+$ bushy cells (*Hhip*/*Calb1* and *Hhip*/*Galnt18*) and three subpopulations in *Atoh7*$^+$ bushy cells (*Atoh7*/*Dchs2*, *Atoh7*/*Tox*, and *Atoh7*/*Sorcs3*) (Figure S5C). However, they rarely formed isolated groups within each bushy cell subtype, and their marker genes showed no obvious demarcation separating the neurons into distinct subpopulations (Figure S5C). Indeed, latent factor analysis shows continuously varying gene expression in either *Atoh7*$^+$ bushy cells or *Atoh7*$^+$ bushy cells (Figure S5D, Methods). We performed a gene expression gradient analysis and assigned each cellular transcriptional profile a gradient score to quantify how much the expression of

genes deviates relative to the middle of the UMAP gene space (Methods) (Li et al., 2020). Application of the gradient score revealed a continuous shift in gene expression in either *Atoh7*$^+$ bushy cells or *Hhip*$^+$ bushy cells. Such graded gene expression was characteristics of UBCs (Figures S1F, S5D) (Guo et al., 2021; Kozareva et al., 2021), but many other CN cell types including T-stellate cells (see below) and cartwheel cells did not exhibit this pattern of gene expression (Figure S5D). Further scoring of the genes by their correlation to the gradient (or latent factor) identified two negatively correlated transcriptional profiles (Figure S5E); the first profile was highly expressed on one side of the gradient, and the second profile was highly expressed on the other side of the gradient. For *Atoh7*$^+$ bushy cells, the first profile consisted of increased expression of *Ryr3*, *Sorcs3,* and more than 600 other genes, including *Kcnq5*, a gene encoding voltage-activated potassium channels impeding repetitive firing in some neurons (Lehman et al., 2017), and the second consisted of increased expression of *Dchs2* and many other genes including *Grid1* and *Grid2*, which encodes glutamate receptor delta subunit 1 and 2 that make glycine-binding delta iGluRs (Figure S5E). For *Hhip*$^+$ bushy cells, the first profile consisted of increased expression of *Galnt18* and more than 400 other genes, including *Gabrg3*, *Kcnq5*, *Grin2b*, *Cacna1c*, and *Kcnj6*, and the second consisted of increased expression of *Calb1* and many other genes including *Kcnq3*, a gene encoding voltage-activated potassium channels mediating M-currents (Figure S5E).

A transcriptomic gradient in a cell type often reflects spatial gradients of gene expression and defining anatomical location, as well as variation in physiological properties such as excitability and spiking properties of neurons (Cembrowski et al., 2016; Muñoz-Manchado et al., 2018; Scala et al., 2021; Stanley et al., 2020). Bushy cells are known to be arranged in a spatial gradient (in a dorsal to ventral progression) according to their response to the different sound frequencies (Karmakar et al., 2017; Muniak et al., 2013; Ryugo and Parks, 2003; Shepard et al., 2019), reflecting the tonotopic map of auditory nerve fibers (ANF) in the CN. A transcriptomic gradient in either of the two bushy cell subtypes may encode a spatial gradient of the soma location and variation of

morphological/electrophysiological features along the dorsal-to-ventral tonotopic axis. To test this hypothesis, we estimated the spatial location of each Patch-seq bushy cell (see Methods) in the CN and also assigned them a gradient score based on the subtypes they were mapped to (Figure 4F, Methods). RNA expression covaried continuously with soma location along the anterior-to-posterior, but not the dorsal-to-ventral axis (the tonotopic axis), which was particularly the case for the *Atoh7* subtype (Figure 4G). The gradient score (relative to the *Dchs2*-expressing neurons as the negative gradient extreme for *Atoh7*$^+$ bushy cell, *Calb1*-expressing neurons as the negative gradient extreme for *Hhip*$^+$ bushy cells, Figure S5C-D) of each bushy cell was positively correlated with their distance to the posterior edge of VCN (anteroposterior axis) ($r = 0.462$, $p = 0.001$ for *Atoh7*$^+$ bushy cell and $r = 0.368$, $p = 0.032$ for *Hhip*$^+$ bushy cells) (Figure 4G), but not with the distance to the dorsal edge of VCN (Figure S4C-D). For example, those bushy cells that were transcriptomically close to *Dchs2*-expressing neurons (the negative gradient extreme, Figure S5C-D) were located at the more anterior part of VCN, whereas bushy cells that were transcriptomically close to another extreme were located at the more posterior part of VCN (Figure 4G). We also found that electrophysiological properties of bushy cells varied continuously across the transcriptomic landscape; the input resistance, for example, had its largest values in those cells with the highest *Dchs2* expression and gradually decreased towards those cells with the highest *Sorcs3* expression in the *Atoh7* subtype (Figures 4H, S5C-D); AHP has its largest value in those cells with high *Galnt18* expression and gradually decreased towards those cells with the high *Calb1* expression in the *Hhip* subtype (Figures 4H, S5C-D). We observed the same in many other individual electrophysiological features (Figure S4C-D). To quantify this effect, we computed an electrophysiological score (Methods) for each Patch-seq bushy cell to reflect how much their electrophysiology deviates relative to the one extreme of the UMAP space and plotted the score against their gradient score, and we found that these two measures were correlated ($r = 0.708$ for *Atoh7* bushy cells, $r = -0.368$ for *Hhip* bushy cells; Figure S4C-D). The correlation was observed within both two subtypes and for many individual electrophysiological features (Figures 4H, S4C-D). These results

indicate that within the *Atoh7* and *Hhip* subtypes of bushy cells, there is a gradation in molecular and electrophysiological features that do not correlate with the sound frequency that each cell encodes, but instead varies with cell location in the rostro-caudal axis.

**Two transcriptomic subtypes of T-stellate cells**

Our Patch-seq mapping indicated the *Fam129a*$^+$ cluster corresponds to T-stellate cells. This cluster comprised two visibly separate lobes on the UMAP map, suggesting the possibility of sub-populations of T-stellate cells. These two putative subclusters were distinguished by applying the SCANPY algorithm with Benjamini-Hochberg correction (Figure 5A), with more than 1100 DEGs identified for them (>2-fold expression difference and $p < 0.01$). The top 20 DEGs include *Kcnmb2*, *Dchs2*, *Kcnd2*, *Shisa9*, *Kcnb2*, *Caln1*, *Gm41414*, *Rreb1*, *Tmem132d* that are highly expressed in one subcluster, and *Bmp6*, *4930401C15Rik*, *Lama3*, *Fn1*, *Sorcs3*, *Stxbp6*, *Kcnq4*, *Kcnh8*, *Kctd16, Kcnh5* that are highly expressed in the other subcluster. Many genes were expressed exclusively in one of the two subclusters (Figures 5A-B, S5F-G), suggesting T-stellate cells comprise two subpopulations. To test this idea, we performed RNA FISH co-staining for *Fam129a* and *Dchs2*, and for *Fam129a* and *Fn1*. *Fam129a* is a general marker for T-stellate cells predicted by our analysis (Figures 2F, S2A-B, S2D), while *Dchs2* and *Fn1* were expressed almost exclusively in one of the two putative sub-populations with high coverage (Figures 5B, S5F-G). FISH *Fam129a* signals were restricted to the VCN (Figure 5C) and almost exclusively detected in excitatory neurons (data not shown), in agreement with the snRNA-seq data (Figure S2A-B, S2D) and Allen ISH data (Data S3). *Fam129a* expression extended across the entire VCN while bushy cells, another major excitatory cell type in the VCN, were devoid of *Fam129a* (Figure S6H), validating *Fam129a* as a general marker gene for T-stellate cells. Co-staining indicated that only a subset of *Fam129a*$^+$ neurons co-expressed *Fn1* (*Fam129a*$^+$/*Fn1*$^+$), and these double-labeled neurons were exclusively localized in the AVCN (Figure 5C). Similarly, only a subset of *Fam129a* $^+$

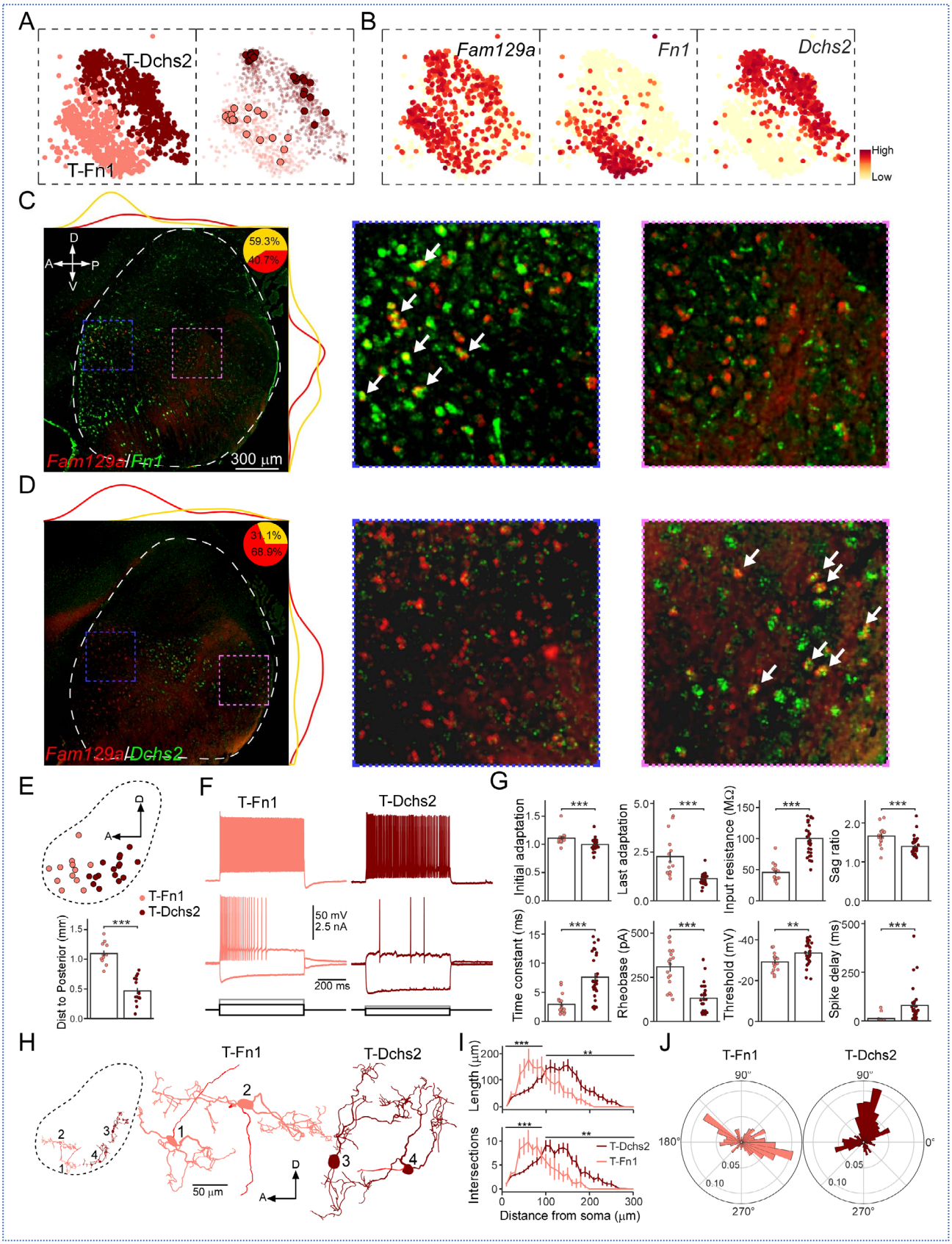


neurons co-expressed *Dchs2*, and these *Fam129a*$^{+}$/*Dchs2*$^{+}$neurons were restricted to the nerve root area (also known as the interstitial area) of the VCN and to the PVCN (Figure 5D). Therefore, FISH

**Figure 5**. **Two distinct molecular subtypes of T-stellate cells**. (**A**) Left: UMAP visualization of two subclusters of *Fam129a*$^+$ neurons (marked by the high expression of *Dchs2* or *Fn1,* see B), colored by the subcluster. Light brown for *Fn1*$^+$ T-stellate (T-Fn1) and dark brown for *Dchs2*$^+$ T-stellate (T- Dchs2). Right: All Patch-seq cells mapped to the *Fam129a*$^+$ cluster on the left. (**B**) UMAP visualization of normalized expression of discriminatory markers for all T-stellate cells and its two subclusters (*Fam129a*, *Fn1*, *Dchs2*). (**C**) FISH co-staining for *Fam129a* and *Fn1* in a CN sagittal section. The inset pie chart shows the proportion of double-labeled cells in single-labeled cells (*Fam129a*$^+$). The lines along FISH images show the density of the single-labeled (*Fam129a)* or double-labeled (*Fam129a*$^+$*/Fn1*$^+$) neurons along the two axis of the CN. The two images on the right are the zoom-in views of boxed regions of the two images on the left. Arrows indicate double-labeled cells. (**D**) RNA FISH co-staining for *Fam129a* and *Dchs2* in a CN sagittal section. Inset pie chart shows the proportion of double-labeled cells in single-labeled cells (*Fam129a*$^+$). Red and yellow lines along FISH images showed the density of single-labeled (*Fam129a)* or double-labeled (*Fam129a*$^+$*/Dchs2*$^+$) neurons along two axis of the CN. Two images on the right are the zoom-in views of boxed regions of the images on the left. Arrows indicate double-labeled cells. (**E**) Top: 2D spatial projection of each Patch-seq cell assigned to *Fn1*$^+$ T-stellate subtype (T-Fn1) and *Dchs2*$^+$ T-stellate subtype (T-Dchs2) to a sagittal view of the CN, colored by the subtypes. Bottom: Comparing the distance to the CN posterior edge between T-Fn1 and T-Dchs2. *** $p < 0.001$ with the t-test.(**F**) Example membrane responses from two distinct T-stellate subtypes (T-Fn1, Left; T-Dchs2, Right) to current steps. Scale bar, vertical 50 mV for the potential, 2.5 nA for the injected currents. (G) 8 electrophysiological features between *Fn1*$^+$ (light brown) and *Dchs2*$^+$ T-stellate (dark brown) subtypes. **$p < 0.01$, ***$p < 0.001$ with the t-test. (H) Left: Representative morphology of two *Fn1*$^+$ T-stellate cells (T-Fn1) and two *Dchs2*$^+$ T-stellate cells (T-Dchs2) in a sagittal view of the mouse CN (their soma locations). Axons in red. Right: A zoom-in view of the four T-stellate cells as shown on the left. (I) Sholl analysis of dendritic arbors of T-Fn1 and T-Dchs2. Top: length; Bottom: intersection. **$p < 0.01$, ***$p < 0.001$ with two-way mixed model ANOVA. (J) The polar distribution histograms of the termination points of dendritic branches with respect to the soma of T-Fn1 (left) and T-Dchs2 (right). The terminal distribution of T-Fn1 has two peaks at 145$^o$ and 345$^o$, while the terminal distribution of T-Dchs2 has two peaks at 75$^o$ and 195$^o$. The difference between the two distributions is tested with the Kolmogorov-Smirnov test (KS statistic = 0.325, $p < 0.001$).

data suggest two spatially separated subpopulations of T-stellate cells. To further substantiate this, we took advantage of Patch-seq cells assigned to T-stellate cells. Those cells were mapped to either *Dchs2*$^+$ subcluster or *Fn1*$^+$subcluster almost equally (Figure 5A), allowing for an unbiased comparison of their spatial locations. *Fn1*$^+$ T-stellate cells were restricted to the AVCN, while *Dchs2*$^+$ T-stellate cells were predominantly localized in the PVCN and the nerve root area of the VCN. Importantly, these two subpopulations were spatially non-overlapping in the VCN (Figure 5E), suggesting T-stellate cells could be classified into distinct subtypes by their anatomical locations.

To further support two subpopulations of T-stellate cells, we examined the morphology of each Patch-seq cell that was assigned as either *Fn1*$^+$ T-stellate cells or *Dchs2*$^+$ T-stellate cells. Both T-stellate subtypes exhibited typical morphology of T-stellate cells (Figure 5H) with their dendrites ending in highly branched tufts (Oertel et al., 1990), but there were subtle differences in their dendritic arborization (Table S4). The dendrites of *Fn1*$^+$ T-stellate cells in general branched earlier and more profusely around the soma compared to that of *Dchs2*$^+$ T-stellate cells, while the dendrites of *Dchs2*$^+$ T-stellate cells arborized more extensively away from the soma with more branched, complex endings (Figure 5H-I, Table S4). In addition, the major dendrites and the terminal arbors of *Fn1*$^+$ and *Dchs2*$^+$

T-stellate cells have distinct preferential angles with respect to their soma (Figure 5J). Given that the major dendrites and the terminal arbors of T-stellate cells in general run parallel to tonotopically arranged ANFs (Figure 5H) (Doucet and Ryugo, 1997; Xie and Manis, 2017) whose direction in each subregion is well-established, such differences between two subtypes reflects their distinct anatomical location in the VCN, further substantiating the assertion that the subtypes of T-stellate cells are defined by their anatomical locations.

The top DEGs that distinguished the two T-stellate cell subpopulations are characterized by numerous genes encoding potassium channels including *Kcnh5*, *Kcnmb1*, *Kcnmb5*, *Kcnb2*, and *Kcnq4*, suggesting distinct electrophysiological properties of two subpopulations (Figure S5F-G). Indeed, UMAP embedding of Patch-seq cells based on the electrophysiological features showed that *Fn1*$^+$ T-stellate cells and *Dchs2*$^+$ T-stellate cells were mostly well separated from each other, despite the small sample of each subpopulation (Figure S5B). Two subtypes showed numerous distinctions in electrophysiological characteristics (Figure 5G, Table S4). *Dchs2*$^+$ cells are more typical of T-stellate cell electrophysiological properties as previously described (Cao and Oertel, 2011; Fujino and Oertel, 2001; Lin and Xie, 2019; Rodrigues and Oertel, 2006), including a modest input resistance and time constant, and a small sag in the response to hyperpolarizing currents; they fired non-adapting spikes and often exhibited a spiking delay in response to near-threshold current injections, resembling cortical fast-spiking neurons (Figure 5F-G and Table S4). *Fn1*$^+$ cells showed less fast-spiking-like properties than *Dchs2*$^+$ cells, including a much smaller input resistance, a much shorter time constant, a bigger sag, significant spiking adaptation, and no spike delay in response to near-threshold depolarizing currents (Figure 5F-G and Table S4). In addition, *Fn1*$^+$ cells are less excitable (i.e., a higher spike threshold and more current needed to elicit spikes) with a narrower AP and faster repolarization compared to *Dchs2*$^+$ cells (Figure 5G, Table S4). A few parameters were strikingly distinct between the two subtypes; for example, spike delay, time constant, and input resistance alone separated almost all *Dchs2*$^+$ cells from *Fn1*$^+$ cells, highlighting remarkably distinct electrophysiology between the two

T-stellate cell subtypes (Figure S5B). Such differences likely reflect differences in the expression of ion channels. Indeed, the highly expressed genes in *Fn1*$^+$ cells encoding multiple leak potential channels including *Kcnk10*, *kcnk9*, and *Kcnk12* could lead to the lower input resistance of these neurons (Figures 5G, S5G). On the other hand, the highly expressed genes encoding Kv2 and Kv3 (*Kcnb2*, *Kcnc2*) in *Dchs2*$^+$ cells may endow them with a more fast-spiking phenotype than *Fn1*$^+$ cells, consistent with the observation that auditory neurons utilize both Kv2 and Kv3 to maintain high-frequency repetitive firing (Johnston et al., 2010; Johnston et al., 2008b; Lau et al., 2000; Rudy and McBain, 2001; Wang et al., 1998a). In addition, the highly expressed genes encoding Kv4 channels (*Kcnd2/3*) and large-conductance calcium-activated potassium (BK) channels (*Kcnmb2, Kcnma1*) in *Dchs2*$^+$ cells may be the molecular basis of their other unique electrophysiological features (Johnston et al., 2008a). As for their synaptic inputs, *Fn1*$^+$ cells exhibited no significant difference from *Dchs2*$^+$ cells in any parameters of either excitatory or inhibitory events (Figure S4E-F).

**Annotation of transcriptomic inhibitory cell types**

Each CN subregion is also populated with well-established glycinergic/inhibitory cell types, including vertical cells, cartwheel cells, and superficial stellate cells (SSCs, also known as molecular layer interneurons) in DCN, and L-stellate cells and D-stellate cells in VCN (Ngodup et al., 2020 (Figures 1A, 6A). To examine if there is a same multi-modal correspondence for inhibitory neurons as for excitatory neurons, we targeted each of these known cell types (except for Golgi cells) for Patch-seq (see Methods). In addition to their difference in anatomical location (except for L- and D-stellate cells), each of these cell types exhibited unique morphological/electrophysiological features (Figure 6A-B), allowing experienced patch clampers to distinguish one type from others with high confidence (Manis et al., 2019). We performed the same analysis on these inhibitory neurons as we did on excitatory neurons to validate the expert classification and cell-type assignment of each Patch-seq cell (Figures 6B-D; Data S2). In general, the forest classifier and clustering-based k-means classifier based

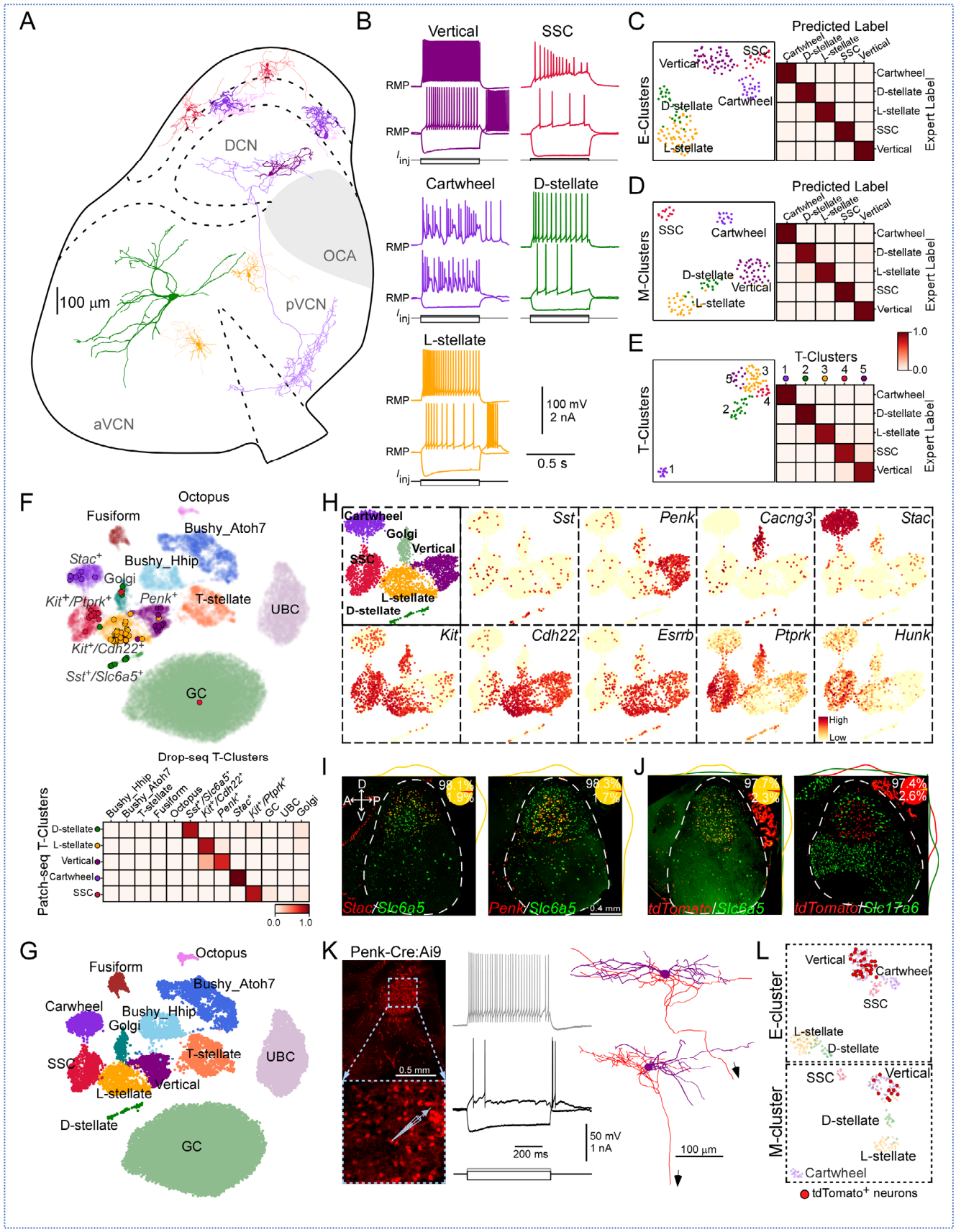


on either electrophysiology or morphology could distinguish each cell type pair with high accuracy, especially with additional location supervision (Figures 6C-D, Data S2), supporting our cell-type

**Figure 6. Annotation of molecularly distinct glycinergic cell types in CN. (A)** Representative morpholology of each inhibitory cell type in distinct subregions of the mouse CN (a sagittal view), colored by the cell type identity. Dendrites are in darker colors than axons. **(B)** Example membrane responses of different CN inhibitory cell types to current steps. Scale bar, vertical 100 mV for the potential, 2 nA for the injected currents. **(C)** Left: UMAP visualization of 163 inhibitory neurons clustered by electrophysiological features and anatomic locations. n = 41 for Vertical, n = 21 for SSC, n = 22 for Cartwheel, n = 26 for D-stellate, n = 53 for L-stellate. Each cell type is colored as in (**C**). To weigh the anatomic locations for cell type classification, we used 0 to represent VCN and 1 to represent DCN in the cluster analysis. Right: Confusion matrix shows the performance (an average of 97.8% accuracy) by the classifier trained with electrophysiological features and anatomic locations. Colored by the expert classification. See Data S2 for the analysis with electrophysiological features only. **(D)** Left: UMAP visualization of 95 CN inhibitory neurons clustered by select morphological features (M-cluster). n = 17 for Vertical, n = 13 for SSC, n = 15 for Cartwheel, n = 17 for D-stellate, n = 33 for L-stellate. Each cell type is colored as in (**C**). Right: Confusion matrix shows the classification performance (an average of 95.5% accuracy) by a classifier trained with morphological features. Colored by the expert classification. **(E)** Left: UMAP projection of 94 Patch-seq inhibitory neurons clustered by the over-dispersed genes, colored by the transcriptomic clusters (T-clusters). Right: The matrix shows the proportion of Patch-seq cells assigned to a specific cell type (the expert classification) in each T-cluster. All cells in T-cluster 1 are cartwheel cells (n=12/12: 100%); almost all cells in T-cluster 2 are D-stellate cells (n=20/21: 95.2%); all cells in T-cluster 3 are L-stellate cells (n = 35/35: 100%); almost all cells in T-cluster 4 are SSCs (n = 10/12: 83.3%), and almost all cells in T-cluster 5 are vertical cells (n=12/14: 85.7%). **(F)** Left: Patch-seq cells (n = 95) mapped to the UMAP space of 31,639 sequenced neuronal nuclei as shown in Figure 1B (13 clusters). Right: The matrix shows the proportion of Patch-seq cells assigned to each T-cluster in (**E**) mapped to one of 13 distinct clusters in the UMAP space. **(G)** Annotation of each molecular cluster with well-studied ME-types in the mouse CN. **(H)** UMAP visualization of all glycinergic neurons and normalized expression of marker genes for each cell type. Each cluster is annotated by Patch-seq. **(I)** FISH co-staining for *Slc6a5* and *Stac* (left), or for *Slc6a5* and *Penk* (right) in CN sagittal sections. Inset pie charts show the proportion of double-labeled cells (*Penk*$^+$/*Slc6a5*$^+$, *Stac*$^+$/*Slc6a5*$^+$) in single-labeled cells (*Stac*$^+$ or *Penk*$^+$). Yellow lines along FISH images show the density of double-labeled neurons (yellow) along two axes of the CN. **(J)** FISH co-staining for *Slc6a5* and *tdTomato* (left), or for *Slc17a6* and *tdTomato* (right) in CN sagittal sections in Penk-Cre:Ai9 mice. Inset pie charts show the proportion of double-labeled cells (*tdTomato*$^+$/*Slc6a5*$^+$, *tdTomato*$^+$/*Slc17a6*$^+$) in single-labeled cells (*tdTomato*$^+$). Colored lines along FISH images show the density of double-labeled neurons (yellow) or single-labeled cells (green or red) along two axes of the CN. (**K**) Left: micrographs show labeled cells in Penk-Cre:Ai9 mice that were targeted for patch-clamp recording. Middle: example membrane responses of a labeled neuron in Penk-Cre:Ai9 mice to current steps. Right: two representative morphologies of labeled neurons. Dendrites and soma in purple, and the axon in red. The arrows indicate the axonal trajectory toward the VCN. (**L**) Top: Distribution of labeled cells (red circle) in UMAP space of all CN inhibitory neurons clustered by electrophysiological features and anatomic location (as shown in Figure 6C). Almost all labeled cells (30/31) clustered with vertical cells in electrophysiological UMAP space. Bottom: Distribution of labeled cells in UMAP space of all CN inhibitory neurons clustered by morphological features (as shown in Figure 6D). All labeled cells clustered with vertical cells in morphological UMAP space.

assignment of each Patch-seq cell. In total, 14 Patch-seq cells were assigned as vertical cells, 12 as SSC, 12 as cartwheel cells, 21 as D-stellate cells, and 35 as L-stellate cells. UMAP projection of these Patch-seq cells resulted in 5 transcriptomic clusters, and the cells labeled as the same type clustered together with very few cells confused with another cluster (Figure 6E). This analysis indicates a high degree of congruence across the three modalities of CN inhibitory cell classification, as seen in excitatory neurons. Using the gene expression profiles, we then mapped these inhibitory Patch-seq neurons to the transcriptomic clusters identified via snRNA-seq (Figure 1B). All cells labeled as cartwheel cells were mapped to the *Stac*$^+$ cluster (12/12 cells = 100.0%), which thus corresponds to cartwheel cells (Figure 6F-G). Most cells labeled as vertical cells were mapped to the *Penk*$^+$ cluster (10/14 cells = 71.4%), consistent with our previous prediction that the *Penk*$^+$ cluster corresponds to vertical cells. Most Patch-seq cells labeled as D-stellate cells were mapped to the *Slc6a5*$^+$/*Sst*$^+$ cluster (18/21 cells = 85.7%), consistent with our prediction based on their specific *Sst* expression and lack of

*Gad1/2* expression (Figure 6F-G). Finally, most Patch-seq cells labeled as L-stellate cells were mapped to the *Kit*$^+$/*Cdh22*$^+$ cluster (30/35 cells = 85.7%), while most cells labeled as SSC were mapped to the *Kit*$^+$/*Ptprk*$^+$ cluster (10/12 cells = 83.3%), suggesting these two clusters corresponds to L-stellate cells and SSCs, respectively (Figure 6F-G).

To substantiate the molecular correspondence for each cell type with FISH, we identified discriminatory genes for each glycinergic cluster (cell type) in CN (Table S1). A long list of discriminatory genes was identified for the *Stac* cluster (cartwheel cells) including *Stac, Kctd12, Myo1b, Gckr, Gria1, Igfbp6, Pstpip1* (Figures 6H, S2, and Table S1). In line with our analysis, *Stac* or *Kctd12* expression was almost exclusively detected in glycinergic neurons and restricted to the pyramidal cell layer of DCN (i.e., where cartwheel cells reside) (Figure 6I, Data S3), thus validating the molecular correspondence and the novel marker genes for cartwheel cells. Three genes, *Penk*, *Greb1*, and *Serpinb1b*, were identified as discriminatory genes for the *Penk*$^+$ cluster (Figures 6H, S2). The patterns of *Penk* expression in terms of cell type and anatomical location in both wild-type mice and an existing Penk-Cre mouse line were consistent with cell type and location of vertical cells (i.e., glycinergic interneurons residing on the deep layer of DCN) (Figure 6I-J, S6E), thus validating the molecular correspondence and a novel marker gene for vertical cells. We also characterized the electrophysiology and morphology of Cre-expressing cells in Penk-Cre mice from the DCN deep layer via patch-clamp recordings (Figure 6K), and the morphological/electrophysiological features of these cells are consistent with vertical cells (Figure 6K-L), indicating Penk-Cre mice can be used to label and manipulate this specific inhibitory cell type. Interesting, in addition to labelling vertical cells, *Penk* expression was also detected in glycinergic neurons in the small-cell cap (Figures 6I-K, Data S3), a small CN region between the granule-cell and magnocellular domains of the VCN (Cant, 1993).

FISH staining further validated that the *Sst*/*Slc6a5* cluster corresponds to D-stellate cells, and could be discriminated from L-stellate cells with a combination of *Dkk3* and *Slc6a5,* in addition to a

combination of *Sst* and *Slc6a5* (Ngodup et al., 2020) (Figures S6A1-A2, S2D, and Table S1). D-stellate cells may also be discriminated with single genes including *Fam20a, Col5a2, Kcnmb1, Ighm, Mecom, and Htr4* (Figure S2E, Table S1). *Kit*$^+$*/Cdh22*$^+$and *Kit*$^+$/*Ptprk*$^+$ clusters correspond to L-stellate cells and SSCs, respectively. In addition to the *Kit/Cdh22* combination, a combination of *Kit and Esrrb (Kit/Esrrb)* could discriminate the *Kit/Cdh22* cluster, thus distinguishing L-stellate cells (Figures 6H, S2D). FISH co-staining revealed *Kit*$^+$ cells were almost exclusively glycinergic neurons (Figure S6D1-D2) and those *Kit*$^+$ glycinergic neurons labeled with *Cdh22*$^+$ or *Essrb*$^+$ (*Kit*$^+$*/Cdh22*$^+$ or *Kit*$^+$*/Essrb*$^+$) were mainly detected in the VCN (Figure S6B1-B2), thus validating that the *Kit*$^+$/*Cdh22*$^+$ cluster includes L-stellate cells. Nevertheless, double-labeled *Kit*$^+$ glycinergic neurons were also sparsely detected in DCN (Figure S6B1-B2), suggesting that the *Kit*$^+$/*Cdh22*$^+$ cluster may also include glycinergic neurons in DCNs that are neither *Stac*$^+$ nor *Penk*$^+$ (Figure S6C1-C1, S6D1-D2). Those *Stac*$^-$ and *Penk*$^-$ glycinergic neurons are much smaller in population and in soma size than *Stac*$^+$ and *Penk*$^+$ glycinergic neurons, respectively, and may thus represent a novel cell type in the DCN (Figure S6C1-C2, S6D1-D2). As for SCCs, in addition to the *Kit/Ptprk* combination, a combination of *Kit* and *Hunk (Kit/Hunk), or Kit* and *Galnt18* (*Kit/Galnt18*) could discriminate the *Kit*$^+$/*Ptprk*$^+$ cluster, thus distinguishing SSCs (Figures 6A, S2E). FISH co-staining for *Kit* and *Ptprk*, or for *Kit* and *Hunt* revealed that double-labeled glycinergic neurons (*Kit*$^+$*/Ptprk*$^+$ or *Kit*$^+$*/Hunk*$^+$) were mostly detected in the molecular layer of the DCN (Figure S6B3-B4), validating that the *Kit*$^+$/*Ptprk*$^+$ cluster is composed of SSCs as suggested by our Patch-seq mapping. Double-labeled cells were also sparsely detected at the VCN, which may reflect the expression of *Hunk* or *Ptprk* in a small subset of L-stellate cells (Figures 6H, S6B3-B4).

**Transcriptional programs underlie functional specialization of each CN cell type**

In summary, we provided compelling evidence supporting a one-one-one correspondence between T-types and well-established ME-types in CN, each of which is linked to a putative functional role in higher-level auditory processing (Figure 6G). Such a correspondence across the modalities allows for

asking how gene expression patterns determine their functional specialization. To begin with, we tested whether morphological/electrophysiological phenotypes could be predicted by gene expression across all cell types using Patch-seq data. We focused on 16 electrophysiological features and used sparse reduced-rank regression, a technique that predicts the firing properties on the basis of a low-dimensional latent space representation computed from a sparse selection of genes (Kobak et al., 2021; Scala et al., 2021). The selected model used 25 genes with a 5-dimensional latent space and achieved a cross-validated $R^2$ of 0.35. To visualize the structure of the latent space, we projected gene expression and electrophysiological properties onto the latent dimensions (Figure 7A). The cross-validated correlations between the first three pairs of projections were 0.87, 0.68, and 0.76, respectively. These first three components clearly separated nine types of neurons (Figure 7A) and illustrated those genes that are closely correlated with electrophysiological variables among these cell types (Figure 7A, right). These genes include specific marker genes identified by our prior DEG analysis (see above) and one gene that is more directly related to electrophysiological properties, *Kcnc2*, a gene encoding Kv3.2 responsible for high-frequency repetitive firing in individual cell types. A reduced-rank regression model restricted to using only ion channel and G-protein coupled receptor genes (Figure S7A) performed almost as well as the full model (cross-validated $R^2 = 0.32$ and correlations 0.83, 0.62, and 0.79, respectively, with regularization set to select 25 genes) and revealed more related genes explaining electrophysiological variability (Figure S7A). Reduced-rank regression analysis using morphological features supported the separation of major types (cross-validated $R^2 = 0.24$ and correlations 0.87, 0.61, and 0.72, respectively) and revealed a select set of genes well predicting morphological diversity (Figure 7B). Notably, some selected genes were directly related to morphological properties, such as *Sema3a*, a gene involved in the growth of apical dendrite of cortical neurons (Polleux et al., 2000; Szczurkowska et al., 2022) and Epha6, a gene involved in the regulation of spine morphology (Das et al., 2016). The *Sema3a* expression may be responsible for the unusually large dendrite trees of D-stellate cells among CN cell types.

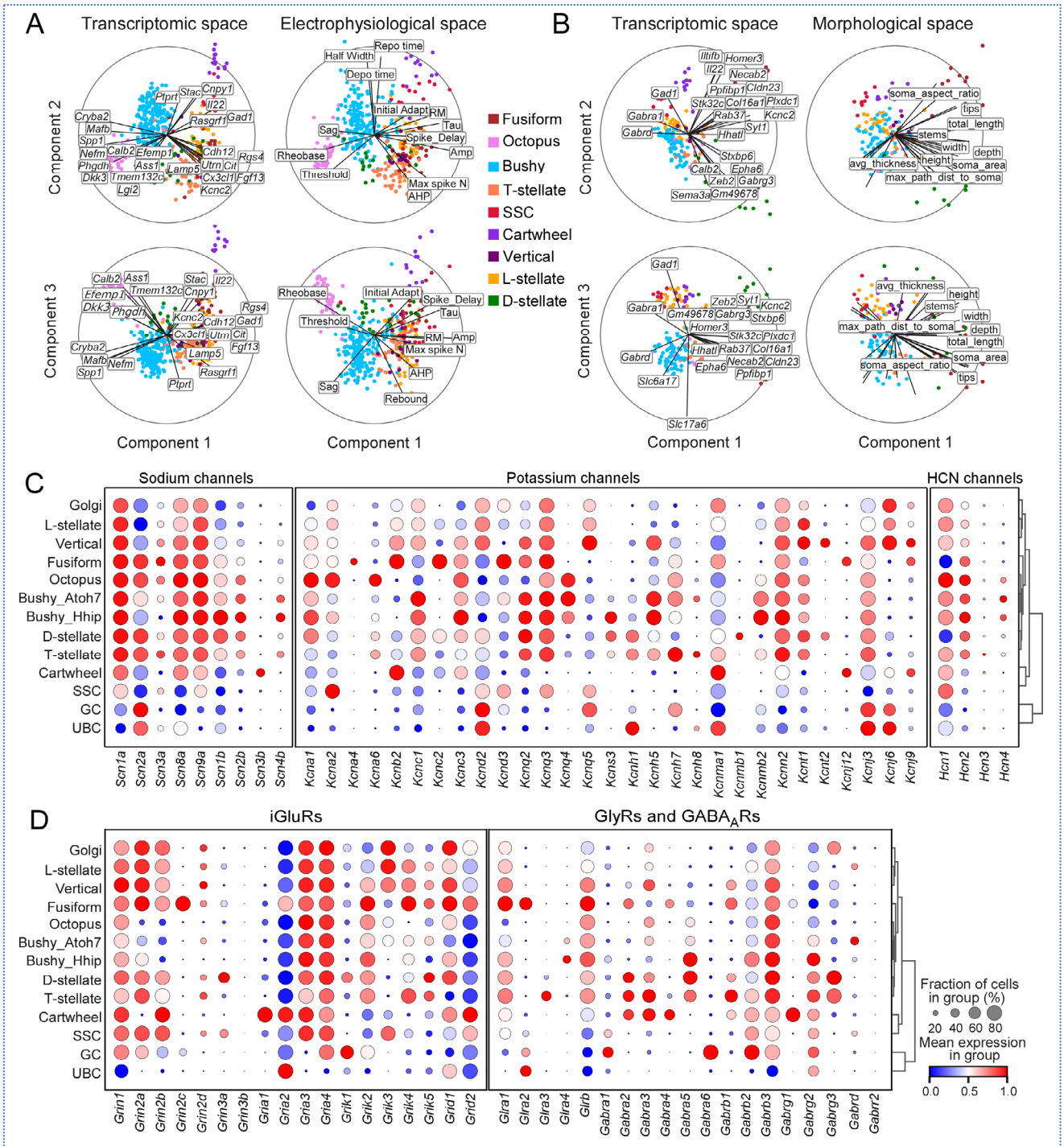


**Figure 7. Single-cell transcriptomes provide insights into functional specializations of CN cell types(A)** A sparse reduced-rank regression (RRR) model to predict electrophysiological features by the top 1,000 highly variable genes. The model selected 25 genes. The cross-correlation results were presented as a pair of biplots, or bibiplot (left: transcriptome, right: electrophysiology). In each biplot, lines represent correlations between each electrophysiological property and two components; the circle corresponds to the maximum attainable correlation ($r$ =1). Only features with an average correlation above 0.4 are shown. **(B)** A sparse reduced-rank regression (RRR) model to predict morphological features by the top 1,000 highly variable genes. The cross-correlation results were presented as a pair of biplots, or bibiplot (left: transcriptome, right: morphology). Only features with an average correlation above 0.4 are shown. **(C)** Dot plots showing scaled expression of the genes encoding ion channels across CN cell type (from snRNA-seq dataset). The genes encoding those potassium channel subtypes with low expression levels (< 20% fraction of the cell in any group) were not included in the figure. The size of each circle depicts the percentage of cells in the cluster in which the marker was detected (≥ 1 UMI), and its color depicts the average transcript count in expressing cells (nTrans). See also Figure S10. **(D)** Dot plots showing scaled expression of the genes encoding ionotropic receptors in each CN cell type. See also Figure S10.

We next analyzed the expression of genes that encode ion channels and neurotransmitter receptors

(Figures 7C-D, S7B-E). Patterns of several ion channel families, glutamate receptors, and neuromodulator receptors across cell types were highly correlated with functional specialization and thus were noteworthy.

***Determinants of biophysical properties***

Each principal cell type in the CN is biophysically specialized for the tasks they perform (Yin et al., 2019). Time-coding neurons including bushy cells and octopus cells have a number of biophysical features associated with precise spike timing, including exceptionally prominent low-voltage-activated $K^+$ conductances ($I_{KL}$, mediated by Kv1 channels) and hyperpolarization-activated conductances ($I_h$, mediated by HCN channels) (Bal and Oertel, 2000, 2001; Cao et al., 2007; Golding et al., 1999; Manis and Marx, 1991; Rothman and Manis, 2003). These neurons also have non-overshooting spikes and appear to lack somatic spikes, which may also aid in spiking fidelity precision (Yang et al., 2016). By contrast, T-stellate cells lack $I_{KL}$ and have small $I_h$ near rest, suitable for tonic firing, and thus biophysically specialized for encoding slower temporal features such as the sound envelope (Ferragamo et al., 1998; Oertel et al., 2011; Rodrigues and Oertel, 2006). As expected, octopus cells had the highest expression of Kv1 channels including Kv1.1 (*Kcna1*), Kv1.2 (*Kcna2*), and Kv1.6 (*Kcna6*), while T-stellate cells have very low Kv1 expression (Figure 7C). Notably, fusiform cells are characterized by the exclusive expression of Kv1.4 (*Kcna4*) (Figure 7C). As for $I_h$, HCN1 (*Hcn1*) and HCN2 (*Hcn2*) were two dominant HCN subunits expressed across CN cell types. HCN1, an HCN subunit with the fastest kinetics (Moosmang et al., 2001), had the highest expression in octopus cells (Figure 7C), consistent with that $I_h$ in octopus cells have fast kinetics, a depolarized voltage range of activation, and apparent insensitivity to cAMP (Cao and Oertel, 2011; Rodrigues and Oertel, 2006). Bushy cells also expressed a high level of HCN1, and a slower $I_h$ in these cells compared to octopus cells could be due to the cell-type-specific expression of HCN4 (*Hcn4*) channels, a subunit with the slowest kinetics (Figure 7C). Other cell types including fusiform cells, D-stellate cells, and T-stellate cells have a lower expression of either HCN1 or HCN2 subunit than bushy cells and octopus cells,

consistent with the kinetics and amplitude of their $I_h$ (Koch et al., 2004; Santoro et al., 2000).

The unusual spike properties in time-coding neurons suggest a cell type-specific expression pattern of distinct sodium α subunits (Yang et al., 2016), but their expression patterns were quite similar across projection cell types, characterized by a high expression of Nav1.6 (*Scna8*) and Nav1.7 (*Scna9*), a subunit thought to be expressed only in the peripheral system (Figure 7C) (Yu and Catterall, 2003). The unusual sodium conductance in time-coding neurons thus may be due to β subunits (Figure 7C), for example, a high expression of *Scn2b* or S*cn4b* in these neurons (Calhoun and Isom, 2014; Meadows et al., 2002; Smith and Goldin, 1998; Zhao et al., 2011). Other subtypes of potassium channels and other types of ion channels were differentially expressed across CN cell types, which may also contribute to their biophysical specializations (Figures 7B-C, S7B). Kv3.1 and Kv3.3 are two dominant Kv3 subunits expressed across CN types, especially in those time-coding neurons, to enable these neurons to follow high-frequency input with temporal precision (Perney and Kaczmarek, 1997; Wang et al., 1998a). A wider expression of Kv3.3 across CN cell type than Kv3.1 may explain why pathogenic Kv3.3 mutations could result in the binaural hearing deficit (Middlebrooks et al., 2013). In addition, the expression of *Kcnq4*, a gene (encoding Kv7.4) whose mutations underlie human DFNA2 hearing loss (Kharkovets et al., 2000) was exclusively restricted to time-coding neurons, suggesting that Kv7.4 helps refine the temporal precision. This expression pattern in CN also raises the possibility of a central component in the DFNA2 hearing loss.

***Synaptic transmission***

Each CN cell type also relies on synaptic specializations to fulfill their tasks and as such synaptic AMPA receptors (AMPARs) in the CN may be specialized according to the source of inputs (Gardner et al., 1999, 2001; Petralia et al., 1996). Our snRNA-seq data provide direct molecular evidence for this specialization: those cell types targeted solely by ANFs (i.e., bushy cells, T-stellate cells, octopus cells, vertical cells) share similar AMPAR composition with rapid gating kinetics, large conductance, and calcium permeability (i.e., GluR3 and GluR4) (Petralia et al., 2000; Rubio et al., 2017; Wang et

al., 1998b), and those targeted by parallel fibers only (i.e., cartwheel cells) have AMPAR composition with slow gating kinetics and calcium impermeability (i.e., GluR1 and GluR2) (Petralia et al., 1996), and those targeted by both fibers (i.e., fusiform cell) have mixed AMPAR composition (Figure 7D). This specialization rule still holds for mossy fibers: AMPARs in the mossy fiber-UBC synapse appear to form almost exclusively by GluR2 (*Gria2*, Figure 7D), an uncommon form of native AMPAR (Zhao et al., 2019) which may contribute to unique synaptic transmission characteristics of these synapses (i.e., a delayed prolonged AMPA current) (Borges-Merjane and Trussell, 2015; Lu et al., 2017).

In general, time-coding neurons including bushy cells and octopus cells have a low expression level of the other three types of ionotropic glutamate receptors (iGluRs; kainate, delta, NMDA receptors) at the age we examined compared to non-time-coding neurons (Figure 7D) (Isaacson and Walmsley, 1995; Wickesberg and Oertel, 1989). This is in agreement with prior evidence that great reduction or elimination of NMDA receptor expression from the synapses of time-coding neurons during development helps refine the temporal precision (Bellingham et al., 1998; Futai et al., 2001; Joshi and Wang, 2002; Pliss et al., 2009). In contrast, most of the non-time-coding cell types, especially those in DCN, were co-enriched with three iGluR types except for GCs and UBCs (Figure 7D). UBCs were almost devoid of all three iGluR types, while GCs had only low levels of kainate and delta receptors (Figure 7D).

Synaptic inhibition is also essential for functional specializations (Lin and Xie, 2019; Lu et al., 2008; Xie and Manis, 2013). Bushy cells receive slow glycinergic inhibition, likely due to the specific expression of the GlyRα4 subunit (*Glra4*), a subunit with slow gating kinetics (Figure 7D) (Lin and Xie, 2019). Glycine receptors in L-stellate neurons, D-stellate neurons, and vertical cells contain only GlyRα1 subunit (*Glra1*), a subunit with the fastest gating kinetics, suggesting exceptionally brief glycinergic inhibition in these cell types (Figure 7D). Glycine receptors in excitatory interneurons (GC and UBC) appear to be exclusively composed of GlyRα2 subunits (*Glra2*), a subunit predominantly

expressed in the neonatal brain (Akagi et al., 1991), while octopus cells, as expected (Wickesberg et al., 1991), were devoid of any glycine receptor subunits (Figure 7D). As for $GABA_A$ receptors, distinct CN cell types including octopus cells all expressed β2 (*Gabrb2*), β3 (*Gabrb3)*, and γ2 (*Gabrg2*) subunits, but expressed different α subunits, suggesting β2γ2 and β3γ2-containing receptors may be particularly well suited to auditory processing requirements. Octopus cells expressed $GABA_A$ receptors, suggesting that they do receive synaptic inhibition, although from unknown sources (Figure 7D). δ-$GABA_A$ receptor (*Gabrd*) was mainly restricted to *Athoh7*$^+$ bushy cells, and the expression of these subunits and α5-$GABA_A$ (*Gabra5*) raises the possibility of tonic GABAergic inhibition in bushy cells (Zheleznova et al., 2009) (Figure 7D).

Finally, Patch-seq and snRNA-seq analysis determined cell-type specific expression patterns of a wide variety of receptors for neuromodulatory transmitters released in CN (Figure S7D-E), which may underlie previous cellular and systems-level physiological observations (Goyer et al., 2016; Kossl and Vater, 1989; Trussell, 2019).

## Discussion

One of the biggest challenges in defining a cell-type taxonomy of the brain is to meaningfully reconcile definitions of cell types across the many modalities of measurement used to characterize brain cells (Zeng and Sanes, 2017). In the cochlear nucleus (CN), the first relay station in the auditory system, we found success by first defining populations using transcriptomic profiling, and then relating these populations to anatomical, physiological, and morphological features using Patch-seq combined with histology and FISH. We reveal a direct correspondence between molecularly defined cell populations and all previously defined cell types with known behavioral significance. We thus build a comprehensive and thoroughly validated atlas of cell types in the CN that harmonizes the cell type definitions across all modalities. It has been well documented that each cell type in the CN is morphologically and biophysically specialized for processing different aspects of acoustic information

and initiating complex parallel pathways that encode sound location, intensity, pitch, and saliency. Our analysis indicates that such functional specialization is bestowed by unique transcriptomic programs that can be leveraged to discriminate, target, and manipulate them. Given that parallel sensory maps have been defined in the brainstem in most sensory systems, we expect the emergence of similar basic discoveries that extend our understanding of cellular specialization in other sensory systems (Young, 1998). Genetically defining cell types crucial for initiating parallel pathways in sensory systems in general, and the auditory system in particular, opens a new window for functional dissections of parallel processing. Specifically, with novel cell type marker genes identified and validated for each cell type in the CN, the dataset will ensure the rational design of a toolbox to manipulate CN cell types with unprecedented specificity for further genetic dissection of auditory processing. In addition, precisely defining cell types by their molecular specializations in CN will also reveal hitherto unknown central components of hearing disorders and facilitate an understanding of central consequences of hearing loss at a molecular level (Butler and Lomber, 2013; Griffiths, 2002).

**Excitatory neuronal populations in mouse CN**

While excitatory neuronal populations in the CN have been well studied with classical approaches, it remains unknown if these approaches are robust and unbiased enough to cover all neuronal populations in CN and reveal their true cellular heterogeneity. We use snRNA-seq to unbiasedly profile the cellular and transcriptional heterogeneity of the whole neuronal population in the CN, resulting in 7 major molecularly distinct excitatory populations. These excitatory subpopulations correspond to all previously described cell types, indicating that the prior characterization of this population is quite thorough within the capability of the classical approaches. One exception is giant cells, for which no molecular correspondence was identified in our analysis. This could be due to two reasons. First, fusiform cells and giant cells may be genetically similar, as they share the same developmental origin and remain together in one cell mass until well after birth (Martin and Rickets, 1981; Nornes and Morita, 2011; Pierce, 1967; Schweitzer and Cant, 1985). In addition, giant cells are the rarest neurons

in the CN, and these neurons included in our transcriptomic profiling are sparse and may not be separated from the fusiform cell cluster (the *Tnnt1*$^+$ cluster).

Our combined approach reveals molecular subtypes within a classically defined cell class, indicating that conventional categories are not robust enough to account for true cellular heterogeneity. We were able to identify subtypes of bushy cells with distinct properties. In anatomical and physiological studies, bushy cells have been divided into two populations, GBCs and SBCs, based largely on differences in their axonal projections (Lauer et al., 2013). Generally, SBCs are located anteriorly in VCN while GBCs are more posterior (Yin et al., 2019), and this topographic division is mimicked by the *Atoh7*$^+$ and *Hhip*$^+$ bushy cell classes we describe here, suggesting a correspondence between SBC/*Atoh7*$^+$ and GBC/*Hhip*$^+$ groups. From the perspectives of physiology (input resistance, time constant, maximal firing number, sag, AP dynamics) and associated gene expression (Kv1, Kv3.3), *Hhip*$^+$ bushy cells are more capable of preserving temporally precise information for high-frequency sound than *Atoh7*$^+$ bushy cells (Wang and Manis, 2006; Wu and Oertel, 1984), and detecting the coincidence of multiple converging inputs (Cao and Oertel, 2010; Cao et al., 2007; McGinley and Oertel, 2006), a functional division reminiscent of GBC and SBC (Brownell, 1975; Liberman, 1991; Tolbert et al., 1982). Further work will be needed to definitively assign the classical bushy cell subtypes with these transcriptomic classes. However, in previous studies there has been evidence for subgroupings and variation in bushy cell properties. Some investigators have proposed two subtypes of SBCs (small and large), based on their axonal targets in lateral and medial superior olive (Yin et al 2019). In the avian cochlear nucleus magnocellularis, which contains solely SBC homologs, neurons vary in innervation pattern and physiology along the tonotopic axis, with the most posterior/low-frequency SBCs being distinctly different from the main population (Akter et al., 2018). In the present study we have found that within the groupings of mammalian *Atoh*$^+$ and *Hhip*$^+$ bushy cells, distinct variation exists in transcriptomic, topographic, and electrophysiological features, supporting the

concept that SBCs and GBCs are broad cell classes that each contain cells of graded properties or perhaps distinct subtypes.

T-stellate cells play remarkably diverse roles in auditory function, having axonal projections within the CN and but also extending to multiple downstream nuclei as far as the auditory midbrain (Yin et al., 2019). Such broad projections suggest broad physiological functions, yet little information supports heterogeneity with this cell class that might parallel such functions. Our finding that T-stellate cells comprise two distinct groups, characterized by gene expression, intrinsic properties, and topography within the CN is therefore particularly intriguing. In vivo recordings refer to T-stellate cells as "choppers", based on a frequency-independent, regular pattern of spikes observed in spike histograms. Interestingly, several classes of choppers have been distinguished in a wide variety of species including mice, with sustained and transient patterns being the most common (Roos and May, 2012). While it is presumed that chopping itself results from the neuron's intrinsic properties, it is not clear whether the different spike patterns result from properties of auditory nerve inputs, intrinsic properties, or synaptic inhibition. It is possible that the multiple T-stellate subtypes in the present study correspond to these different classes of chopper. Further studies of these subtypes in terms of their synaptic inputs and axonal projections will shed important light on this major class of auditory neurons.

**Glycinergic neuronal populations in mouse CN**

Until recently, the greatest diversity of inhibitory interneurons of CN was thought to be in the DCN (Trussell and Oertel, 2018). The discovery of L-stellate cells of VCN indicated that VCN may also harbor multiple interneuron subtypes besides the D-stellate cell (Ngodup et al., 2020). Here, we show that L-stellate cells, defined simply as small glycinergic neurons of the VCN, are molecularly diverse. Based on the *Penk* expression, the majority of cells in the *Kit*/*Cdh22* cluster (corresponding to the L-stellate cells*)* were devoid of *Penk*, but a small subset of cells close to vertical cells (*Penk*$^{+}$ cells) in

UMAP space expressed strong *Penk* signals (Figure 6H). In light of the expression pattern of *Penk* across CN (Figure 6I-K), this *Penk*-expressing subset of cells should correspond to L-stellate cells in the region corresponding to the small cell cap, just ventral to the granule cell lamina. This topographically unique inhibitory subgroup is thus molecularly different from other L-stellate cells and may comprise a novel class of inhibitory neurons in the CN. Within the DCN *Penk* and *Stac* were selective markers for vertical and cartwheel cells, respectively. As these two cell types play distinct roles in gating auditory and multisensory signals in DCN, the identification of markers should facilitate future studies of their role in auditory processing. In addition, we observed glycinergic neurons in the DCN that express neither *Penk* nor *Stac*, suggesting a hitherto unrecognized inhibitory cell type in the DCN. These cells are small glycinergic neurons of the DCN, genetically similar to small glycinergic neurons of the VCN (i.e., L-stellate cells). Altogether, these results highlight the power of the RNA-seq approach in revealing the complexity of inhibitory circuits in the CN.

## Acknowledgments

We thank the members of Jiang and Trussell labs for technical assistance, discussions, and comments on the manuscript. Research reported in this publication is supported by research grants R01 MH122169, R01 MH120404, R01 NS110767 (to X.J.), R01 DC004450, R35NS116798 (to L.O.T.), and R01 DC017797 (to M.J.M) from the National Institutes of Health. Research reported in this publication was also supported by the Main Street America Fund, a Shared Instrumentation grant from the NIH (1S10OD016167), and by the Eunice Kennedy Shriver National Institute of Child Health & Human Development of the National Institutes of Health under Award Number P50HD103555 for use of the Microscopy Core facilities and the RNA In Situ Hybridization Core facility at Baylor College of Medicine. We thank Dr. Dmitry Kobak and Philipp Berens for helping with the initial data analysis. The content is solely the responsibility of the authors and does not necessarily represent the official views of the National Institutes of Health.

## Author Contributions

J.J., T.N., X.J., Q.M., S.L., C.L. performed the experiments, J.J., M.H., X.J. analyzed the data. X.J., L.T. M.M. supervised all experiments and data analyses. X.J., L.T. prepared the manuscript with input from all co-authors.

## Declaration of interests

The authors declared no competing interests.

## STAR METHODS

### KEY RESOURCES TABLE

| REAGENT or RESOURCE | SOURCE | IDENTIFIER |
|---|---|---|
| Experimental Models: Organisms/Strains | | |
| Wildtype (C57BL/6) | Baylor College of Medicine | |
| GlyT2-EGFP | (Zeilhofer et al., 2005) | RRID:MGI:3835459 |
| Sst-IRES-Cre | Jackson Laboratory | RRID:IMSR_JAX:013044 |
| Penk-IRES2-Cre | Jackson Laboratory | RRID:IMSR_JAX:025112 |
| Gabra6-Cre | MMRRC | RRID:MMRRC_015966-UCD |
| Ai9 reporter | Jackson Laboratory | RRID:IMSR_JAX:007909 |
| Antibodies | | |
| Anti-Necab2 antibody | Sigma-Aldrich | HPA013998 |
| Anti-Phgdh antibody | Invitrogen | PA5-54360 |
| Goat anti-mouse Alexa-Fluor 633 | Invitrogen | A-21052 |
| Goat anti-Rabbit secondary antibody Alexa Fluor™ 647 | Invitrogen | A-21244 |
| Chemical and Reagents | | |
| Nextera XT DNA Library Preparation Kit | Illumina | FC-131-1096 |
| Nextera XT index kit v2 Set A/D | Illumina | FC-131-2001/ FC-131-2004 |
| Vectastain ABC HRP Kit | Vector Laboratories | PK-4000 |
| Chromium Next GEM Single cell 3’ Gel Bead V3.1 | 10x Genomics | PN-1000122 |
| Chromium Next GEM Single cell 3’ GEM Kit V3.1 | 10x Genomics | PN-1000123 |
| Chromium Next GEM Single cell 3’ Library Kit V3.1 | 10x Genomics | PN-1000157 |
| Kapa HiFi HotStart ReadyMix | Roche | 07958935001 |
| Recombinant RNase Inhibitor | Takara | 2313B |
| Biocytin | Sigma-Aldrich | B4261 |
| N-Methyl-D-glucamine | Sigma-Aldrich | M2004 |

| | | |
|---|---|---|
| Superscript II Reverse Transcriptase | Invitrogen | 18064071 |
| High Sensitivity DNA Kit | Agilent Technologies | 5067-4626 |
| Streptavidin Alexa Fluor™ 568 conjugate | Invitrogen | S11226 |
| Protease Inhibitor Cocktail | Promega | G6521 |
| iodixanol | Sigma-Aldrich | D1556 |
| Software and algorithms | | |
| Patchmaster 2.9.1 | HEKA | https://www.heka.com/downloads/downloads_main.html#down_patchmaster |
| Nest-o-patch | glorfin | https://sourceforge.net/projects/nestopatch/ |
| IDL 8.8 | L3Harris Geospatial | https://www.l3harrisgeospatial.com/Software-Technology/IDL |
| Python 3.7 | https://www.python.org | https://www.python.org/downloads/ |
| Scanpy 1.8.1 | (Wolf et al., 2018) | https://scanpy.readthedocs.io/en/stable/installation.html |
| Scvi-tools v0.18.0 | (Gayoso et., 2022) | https://github.com/scverse/scvi-tools |
| Scrublet | (Wolock et al., 2019) | https://github.com/swolock/scrublet |
| Scikit-learn 1.0.2 | https://scikit-learn.org/ | https://scikit-learn.org/stable/install.html |
| Ploty 5.6.0 | https://plotly.com/ | https://plotly.com/python/getting-started/ |
| Seaborn 0.11.2 | https://seaborn.pydata.org/ | https://seaborn.pydata.org/installing.html |
| Matplotlib 3.4.3 | https://matplotlib.org | https://github.com/matplotlib/matplotlib |
| Cellranger 5.0.1 | 10x Genomics | https://support.10xgenomics.com/single-cell-gene-expression/software/pipelines/latest/installation |

| | | |
|---|---|---|
| Star 2.7. 7a | (Dobin et al., 2013) | https://github.com/alexdobin/STAR |
| Featurecounts | (Liao et al., 2014) | http://subread.sourceforge.net/ |
| NLMorphologyConverter 0.9.0 | Neuronland | http://neuronland.org/ |
| MorphoPy 0.7.1 | (Laturnus et al., 2020) | https://github.com/berenslab/MorphoPy |
| Neurolucida Ver. 11 | MBF Bioscience | https://www.mbfbioscience.com/ |
| Others | | |
| Temperature Controller | Luigs & Neumann | 200-100 500 0145 |
| Manipulator | Luigs & Neumann | LN Junior Multipatch |
| Bioanalyzer | Agilent Technologies | G2939BA |
| Qubit 4.0 Fluorometer | Thermofisher | Q33238 |
| Amplifier | HEKA | EPC 10 USB Quadro |
| Micropipette Puller | Sutter | P-1000 |
| Confocal | ZEISS | LSM 710 |
| Mastercycler | Eppendorf | Pro S |
| Neurolucida Explorer | MBF | Ver. 11 |

## RESOURCE AVAILABILITY

Lead Contact

Requests for further information should be directed to the Lead Contact, Xiaolong Jiang (xiaolonj@bcm.edu).

Data and Code Availability

Original electrophysiological, morphological, and RNA-sequencing data supporting the findings of this study have been deposited to the Mendeley Data (doi:10.17632/2n8m8k6b2g.1). The original code has been deposited at GitHub (https://github.com/bcmjianglab/cn_project).

## EXPERIMENTAL MODEL AND SUBJECT DETAILS

### Animals

All experiments were performed according to the guidelines of the Institutional Animal Care and Use Committee (IACUC) of Baylor College of Medicine and Oregon Health and Science University. Wild-type mice or transgenic mice of both sexes on the C57/BL6/J background at the age of postnatal (P) 22-28 were used for single-nucleus RNA sequencing and slice electrophysiology (including Patch-seq). To help distribute our sampling across cell types and to increase the chance of recording certain specific cell types, GlyT2-EGFP mouse line were used to target glycinergic/inhibitory neuronal populations (labeled neurons), while unlabeled cells were targeted for excitatory neuron recording (Ngodup et al., 2020). SST-Cre:Ai9 mouse line was crossed with GlyT2-EGFP mice to identify D-stellate cells and L-stellate cells in the cochlear nucleus for patch clamp recordings (Ngodup et al., 2020). Some recordings from excitatory neurons were performed using wild-type mice as well. In this study, we used 222 mice in total (121 males and 101 females), including 132 wild-type mice, 61 GlyT2-EGFP mice, 17 Penk-Cre:Ai9 mice, and 3 Gabra6-Cre:Ai9 mice. Penk-Cre mice are a gift from Yong Xu Lab at Baylor College of Medicine. All animals were maintained in the animal facility with a light cycle from 6 am to 6 pm daily, with temperatures ranging from 68 to 72 °F and humidity ranging from 30% to 70%.

## METHOD DETAILS

### Single nucleus extraction and single-nucleus RNA sequencing (snRNA-seq)

Mice were deeply anesthetized with 3% isoflurane and decapitated immediately, and their brains were immediately removed from the skull and then transferred into an iced oxygenated NMDG solution (93 mM NMDG, 93 mM HCl, 2.5 mM KCl, 1.2 mM $NaH_2PO_4$, 30 mM $NaHCO_3$, 20 mM HEPES, 25 mM Glucose, 5 mM Sodium Ascorbate, 2 mM Thiourea, 3 mM Sodium Pyruvate, 10mM $MgSO_4$ and 0.5 mM $CaCl_2$, pH 7.4) for further dissection. Cochlear nuclei (CNs) were dissected from each brain under a stereoscopic microscope and then transferred into a 1.5 mL Eppendorf tube, and tubes were immediately immersed in liquid nitrogen. Brain tissues were then transferred into a -80 ºC freezer for

long-term storage. Each tissue sample was pooled from 8 to 10 mice for single-nucleus extraction and single-nucleus RNA sequencing (snRNA-seq).

Single nucleus extraction from brain tissues followed a published protocol (Krishnaswami et al., 2016). Briefly, frozen tissues were homogenized with 2 mL homogenization buffer (HB, 250 mM Sucrose, 25 mM KCl, 5 mM $MgCl_2$, 10 mM Tris, 1µM DTT, 1x Protease Inhibitor, 0.4 units/µL Rnase Inhibitor, 0.1% Triton X-100) in Wheaton Dounce Tissue Grinder. Cell debris and large clump were removed with a 40 µm cell strainer (Flowmi). The homogenate was centrifuged at 1,000 g for 5 min at 4 ºC. The palette was resuspended with 25% iodixanol in the centrifugation buffer (CB: 250 mM sucrose, 25 mM KCl, 5 mM $MgCl_2$, 10 mM Tris) and layered on top of 29% iodixanol. The mixture was centrifuged at 13,500 g for 15-30 min at 4 ºC. The supernatant was carefully removed without disrupting the nuclei pellet. The nuclei pellet was resuspended with the resuspension buffer (RB: 1 % UltraPure BSA in Rnase-free PBS).

Nuclei were counted using a hemocytometer or CellCounter (Countess II, Invitrogen) and diluted to ~ 1,000 nuclei/µL for single-nucleus capture on the 10x Genomics Chromium Next GEM Single Cell 3'v3 system following the standard user guide. Droplet-based snRNA-seq libraries were prepared using the 10x Genomics Chromium Single Cell kit according to the manufacturer's protocol and were sequenced on the Illumina NovaSeq 6000 or Hiseq 4000 platform with a pair-end 150 bp strategy (average depth 40k–50k reads/nucleus). Cell Ranger (version 5.0.1) with the *Mus musculus* genome (GRCm38) and annotation GTF (version M23) was used to generate the output count matrix.

**Slice preparation and electrophysiology**

Brain slices were prepared from the mouse cochlear nucleus as previously described with a slight modification (Jiang et al., 2015; Ngodup et al., 2015; Yang and Xu-Friedman, 2008). Briefly, mice at P22-28 were deeply anesthetized with 3% isoflurane and then immediately decapitated. The brain was removed and placed in the iced oxygenated NMDG solution (for the recipe, see above). The brain

tissue containing cochlear nucleus was sliced into 200-300 µm thick sections parasagittally in the NMDG solution with a microtome (Leica, VT1200). The slices were transferred into the oxygenated NMDG solution (34 ± 0.5 ºC) for 10 min and then incubated in the artificial cerebrospinal fluid (ACSF, 25 mM NaCl, 2.5 mM KCl, 1.25 mM $NaH_2PO_4$, 25 mM $NaHCO_3$, 1 mM $MgCl_2$, 25 mM glucose and 2 mM $CaCl_2$, pH 7.4) at 34 ± 0.5 ºC for 40-60 mins before recording.

Whole-cell recordings were obtained from cochlear nucleus neurons as previously described (Jiang et al., 2015). Borosilicate glass pipettes (3–5 MΩ) were pulled with micropipette pullers (P-1000, Sutter) and filled with intracellular solution containing 120 mM potassium gluconate, 10 mM HEPES, 4 mM KCl, 4 mM MgATP, 0.3 mM $Na_3GTP$, 10 mM sodium phosphocreatine, and 0.5% biocytin (pH 7.25). Whole-cell recordings were performed at 32 ± 0.5 ºC with the EPC 10 amplifiers (HEKA Electronics, Lambrecht, Germany). PatchMaster (HEKA) was used to operate the recording system and record the electrophysiology data. The membrane potential response of each neuron to increasing current steps (600 ms) every 1s was digitized at 25 kHz. To compare the intrinsic properties and firing pattern across cell type, their membrane responses to a hyperpolarizing current step, to the current step at the rheobase, and to a current step at 2X rheobase were recorded and shown for each cell type (Figure 2-6). Spontaneous synaptic events were recorded at -60 mV for at least 30s. Recorded neurons were then fixed for *post hoc* morphological recovery.

**Patch-seq**

Patch-seq was performed on cochlear nucleus neurons following our published protocol (Cadwell et al., 2017). Briefly, the RNA was extracted from each neuron upon completion of whole-cell recordings (including recordings of synaptic events) with a modified internal solution (110 mM potassium gluconate, 4 mM KCl, 10 mM HEPES, 0.2 mM EGTA, 4 MgATP, 0.3 $Na_2ATP$, 5 mM $Na_2$-phosphocreatine, 0.5% biocytin and 0.48 units/µL RNase inhibitor, pH 7.25). Recorded neurons were then fixed for *post hoc* morphological recovery. The RNA was reverse transcribed with Superscript II Reverse Transcriptase (Invitrogen). The cDNA samples that passed quality control were used to

generate sequencing libraries using the Nextera XT DNA Library Preparation Kit (Illumina), following the user guide. Each library was sequenced at a depth of 1~2 million pair-end 150bp reads on the Illumina NovaSeq 6000 or Hiseq 4000 platform. Raw reads were aligned to the *Mus musculus* genome (GRCm38) with annotation GTF (version M23) using STAR 2.7.7a (Dobin et al., 2013), and an expression matrix was generated with FeatureCounts (Liao et al., 2014).

**RNA fluorescence in situ hybridization**

RNA fluorescence in situ hybridization (FISH) was performed on 25 µm thick sagittal sections containing the cochlear nucleus at the RNA In Situ Hybridization Core at Baylor College of Medicine, using a previously described in situ hybridization method with slight modifications (Yaylaoglu et al., 2005). Digoxigenin (DIG) and Fluorescein isothiocyanate (FITC) labeled mRNA antisense probes were generated from reverse-transcribed mouse cDNA. Primer sequences for the probes were derived from Allen Brain Atlas (http://www.brain-map.org). DIG-labeled probes were visualized with tyramide-Cy3 Plus and FITC-labeled probes were visualized with tyramide-FITC Plus. Images were captured at 20X magnification using LSM 710 or 880 confocal microscope (Zeiss).

**Immunofluorescence staining**

GlyT2-EGFP mice at P22-28 were perfused transcardially with 20 mL PBS followed by 20 mL of 4% PFA in 0.1 M PB. The brain was removed, post-fixed in 4% PFA for 1 day, and then sagittally sectioned into 50 µm thick slices in PBS. The slices were washed 3 times in PBS before blocking with 10% goat serum and 1% Triton X in PBS for 1 hour. The slices were incubated first with mouse anti-Phgdh (Invitrogen, 1:400) or rabbit anti-Necab2 (Invitrogen, 1:500) as primary antibodies, and then incubated with Alexa-Fluor goat anti-mouse 633 or goat anti-rabbit Alexa-Fluor 647 (Life Technologies) as secondary antibodies for at least 1 hour. Slices were then mounted with the mounting medium (Abcam, ab104139). To stain Phgdh or Necab2 in recorded neurons, brain slices were immediately fixed after whole-cell recording with 4% PFA for 1 day. The slices were first incubated with primary antibodies (see above) for at least 1 hour, and then incubated with Alexa Fluor 568

conjugates of streptavidin to visualize biocytin together with those secondary antibodies (see above) to visualize putative signals of Phgdh or Necab2 in recorded neurons. Images were captured at 10× or 20× magnification using LSM 710 confocal microscope (Zeiss).

### Morphological recovery

Morphological recovery of recorded neurons and light microscopic examination of their morphology were carried out following previously described methods (Jiang et al., 2015). In brief, upon the completion of whole-cell recordings, the slices were immediately fixed in 2.5% glutaraldehyde/4% paraformaldehyde in 0.1M PB at 4 °C for 10-14 days and then processed with an avidin-biotin-peroxidase method with an ABC kit to reveal cell morphology. Recovered neurons were examined and reconstructed using a 100× oil-immersion objective lens and camera lucida system (Neurolucida, MicroBrightField).

## QUANTIFICATION AND STATISTICAL ANALYSIS

### Computational analysis of snRNA-seq data

For snRNA-seq data, we used CellRanger (version 5.0.1) to generate a barcode table, gene table, and gene expression matrix. Downstream analysis and visualization were performed using Scvi-tools and SCANPY (Wolf et al., 2018). For preprocessing, we followed the standard protocols used in the field (Luecken and Theis, 2019). Specifically, nuclei with > 5% UMIs mapped to mitochondrial genes and those with less than 200 genes detected were excluded from the analysis. We removed potential doublets sample-by-sample using Scrublet (Wolock et al., 2019). Doublet score and doublet predictions histogram of each sample were manually inspected, adjusted, and then concatenated. A putative single nucleus with a doublet score exceeding the 95$^{th}$ percentile was removed from the downstream analysis. Those putative single nuclei co-expressing multiple canonical marker genes for different cell types were also considered as doublets and were excluded for further analysis: *Mobp/Mog/Mag* (ODC), *Gabra6* (granule cell), *Ptprc/Csf1a/C1qa* (microglia), *Slc1a2/Aqp4/Gja1*

(astrocyte), *Dcn* (fibroblast), *Gad1/Gad2/Slc6a5* (inhibitory neurons), *Flt1/Cldn5* (endothelial). Counts of all the nuclei were normalized by the library size multiplied by 10,000 and then logarithmized. The top 6,000 highly variable genes, which were identified by dispersion-based methods, were used for principal component analysis. Leiden graph-clustering method and UMAP were used for clustering and visualization.

Due to the proximity of the cochlear nucleus (CN) to the cerebellum (CB), paramedian lobule (dorsal to the CN), the principal sensory nucleus of the trigeminal nerve (PSN; ventral to CN), and the dentate nucleus, our microdissection inevitably includes more or less of these adjoining tissues. To remove potential CB-derived nuclei from our dataset (Method S1), we compared our data to a recently published CB snRNA-seq dataset (Kozareva et al., 2021). By examining the expression of marker genes for each CB cell type (identified by Kozareva et al., 2021) in our snRNA-seq data, we identified several putative neuronal and non-neuronal CB clusters in our dataset. Firstly, two clusters show clear molecular signatures of Bergmann cells and Purkinje cells respectively (Method S1A-B), indicating they are contaminated nuclei from these two CB-specific cell types. Secondly, two large clusters assigned to granule cells (i.e., enriched with the canonical marker gene *Gabra6*) could be discriminated by the expression levels of *Grm4* and *Col27a1* (Method S1C). Based on the molecular signatures of CB granule cells (Kozareva et al., 2021) and Allen Brain Atlas ISH data (Method S1C), we concluded that *Grm4*$^{-}$/*Col27a1*$^{+}$ cluster corresponds to granule cells from CN, while the *Grm4*$^{+}$/*Col27a1*$^{-}$ cluster corresponds to granule cells from CB (CB_Granule). After removing these CB clusters from our dataset, we computationally isolated the neuronal population (except for granule cells and UBC) and then performed subclustering analysis to reveal distinct neuronal clusters (Method S1D). One neuronal cluster enriched with *Htr2c* and two clusters enriched with *Necab2* were first identified (Method S1E-F). As shown on Allen Brain Atlas (Method S1E), *Htr2c* expression is restricted to the dentate nucleus, and thus this *Htr2c*-enriched cluster in our dataset is from the dentate nucleus. Two *Necab2*$^{+}$ clusters are either *Tnnt1*$^{+}$ or *Tnnt1*$^{-}$, and only the *Tnnt1*$^{+}$ nuclei are from the CN

while *Tnnt1*$^{-}$ nuclei are from the PSN, based on Allen ISH data (Method S1E-F) and our FISH data (Figure S3).

We then identified two pure GABAergic clusters (*GAD1*$^{+}$/*Slc6a5*$^{-}$*)* enriched with *Tfap2b* (Method S1G), reminiscent of molecular signatures of MLI1 and MLI2 from the CB (Kozareva et al., 2021). Since pure GABAergic interneurons in the CN are absent or extremely rare (Method S1H), we concluded these two clusters are indeed MLI1 and MLI2 from the CB. We also identified two *Tfap2b*-enriched glycine/GABA combinatorial clusters reminiscent of Golgi cells (Kozareva et al., 2021), which are either *Scrg1*$^{+}$ or *Scrg1*$^{-}$. We concluded that the *Scrg1*$^{+}$ cluster results from contaminated nuclei from Golgi cells in the CB (CB_Golgi) based on the CB snRNA-seq dataset (Kozareva et al., 2021) and our FISH data (Method S1I); only the *Scrg1*$^{-}$ cluster corresponds to CN Golgi cells (CN_Golgi, Method S1I, Figure S2). We also identified a glycine/GABA combinatorial cluster enriched with both *Klhl1 and Slc36a2* (Method S1G), reminiscent of Purkinje layer interneurons (PLIs) from the CB (Kozareva et al., 2021). We conclude that this indeed corresponds to PLIs contaminated from the CB based on the expression patterns of *Klhl1 and Slc36a2* across CN and CB (Method S1J).

Removal of non-neuronal nuclei from adjoining regions was not addressed (except for Bergmann cells) since non-neuronal populations are not the focus of our analysis. Thus, the non-neuronal nuclei as shown in Figure S1B may include those from adjoining regions. The UBC population in our dataset may include CB-derived UBCs, but we believed that this contamination, if any, was minimal. Firstly, using the ratio of the UBC population versus GC population in the CB (~1: 300) (Kozareva et al., 2021), we estimated ~80 UBCs from CB might be included in our dataset (based on 24,118 CB-derived GCs in our dataset). In addition, the region of the CB close to the CN (i.e., CB paramedian lobule) has a smaller population of UBCs compared to other regions of the CB. We thus concluded that out of 3,653 UBCs in our dataset, only a very small number of them may be UBCs from the CB, which would not significantly affect our analysis.

After the removal of the nuclei from adjoining tissues, the remaining 61,211 nuclei were used for further clustering analysis, and each cluster and cell type were annotated with the commonly used marker genes as listed in Table S1 (including the marker genes for CB cell types).

**Patch-seq data Analysis**

In total, we performed Patch-seq from 438 cells (323 excitatory neurons, 115 inhibitory neurons, from 69 mice) that passed initial quality control. Among these sequenced 438 cells, 388 neurons (293 excitatory neurons, 95 inhibitory neurons) passed further quality control, yielding 2.40 ± 0.08 million (mean ± s.e.) reads and 8,025 ± 70 (mean ± s.e.) detected genes per cell (Data S1). Of these neurons, 154 had sufficient biocytin staining for their morphology to be reconstructed (97 excitatory neurons, 57 inhibitory neurons). Patch-seq data were clustered and visualized following a similar method with SCANPY. Cells with a mapping rate of < 60% and gene features of < 4000 were not included in the analysis. We used the batch-balanced KNN method for batch correction (Polański et al., 2019). Patch-seq data were mapped to the snRNA-seq data following a similar protocol as used previously (Scala et al., 2021; Scala et al., 2018). Briefly, using the count matrix of 10x Genomics snRNA-seq data, we selected 3000 "most variable" genes, as described previously (Kobak and Berens, 2019). We then log-transformed all counts with log2(x+1) transformation and averaged the log-transformed counts across all cells in each of the identified clusters in the snRNA-seq dataset to obtain reference transcriptomic profiles of each cluster (N×3000 matrix). Out of these 3,000 genes, 2,575 are present in the mm10 reference genome that we used to align reads in our Patch-seq data. We applied the same log2(x+1) transformation to the read counts of Patch-seq cells, and for each cell, computed Pearson correlation across the 2,575 genes with all clusters. Each Patch-seq cell was assigned to a cluster to which it had the highest correlation.

**DEG analysis and marker gene identification.**

To identify the DEGs in clusters and subclusters, we used SCANPY to rank genes using the T-test_overestim_var test with Benjamini–Hochberg correction. SCANPY generated logFC (with the base as 2) and FDR (False discovery rate) corrected P value. This method could detect more DEGs in

the clusters that have large numbers of cells, while in relatively small cell populations only those with much higher fold changes could be identified as DEGs.

**Electrophysiological feature extraction and analysis**

Electrophysiological data were analyzed with a python-based GUI named PatchView that we have developed (Ming Hu, 2022) or a custom-made IDL code. To access the IDL code, the raw electrophysiological data was exported to ASCII format using Nest-o-Patch. To highlight the differences in the intrinsic properties and firing patterns, the membrane responses to a hyperpolarizing current step, to the current step at the rheobase, and to a current step at 2X rheobase were shown for each cell type (Figure 2-6). 20 electrophysiological features were extracted from the electrophysiological traces following a similar method as previously described (Method S2) (Scala et al., 2021).

To calculate the time constant (Tau), all the traces in response to negative current steps (from the onset of the current step to the minimal potential during the stimulation period) were fitted with an exponential function as follows:

$$f(t) = ae^{(-t/\tau)} + C$$

Here, *f(t)* is the voltage at the time *t*, $\tau$ is the membrane time constant, *a* and *C* are two constants. The $\tau$ was calculated for each trace. Boxplot was used to remove the outliers and the mean averaged across all traces after outlier removal was used as the time constant.

We calculated the sag ratio and rebound voltage using the hyperpolarizing trace elicited by the maximal negative current injection. The sag ratio was defined as the difference between the sag trough of the trace and the resting membrane potential (RMP) ($\Delta$V1), divided by the difference between steady-state membrane voltage and the RMP ($\Delta$V2). The trace from the stimulation offset to the peak of the depolarizing trace following the offset was fitted with an exponential function, and the potential difference between the maximal value of the fitting curve and the RMP was defined as the rebound

value.

To calculate the input resistance and RMP, we measured the steady-state membrane potentials (determined by the average values of the last 100 ms of the hyperpolarization) in the traces elicited by the first five negative-going currents in the step protocol, and then plotted these values (y-axis) with each of the corresponding currents (x-axis). We fit the plot with a linear function shown as follows:

$$f(c) = R_m c + V_{rmp}$$

Here, *f(c)* steady-state voltages, c is the injected currents, *Rm* and *Vrmp* are constants that represent the slope of the linear function and the potential at the y-axis intersection, corresponding to the input resistance and the RMP respectively.

Rheobase is defined as the minimum current that could elicit any action potentials (APs) during the step-current injection. To extract the properties of action potential (AP), we used the first AP elicited by our step stimulation protocol. To calculate the threshold of the AP, the trace within 20 ms preceding the AP peak was used to calculate the third derivative and the data point with the maximal third derivative value was defined as the AP threshold (Henze and Buzsaki, 2001). The AP amplitude is the difference between the threshold potential and the peak potential of the AP. The AP half-width was defined as the time difference between the voltage at AP half-height on the rising and falling phase of the AP. The afterhyperpolarization (AHP) was defined as the potential difference between the AP threshold and the minimal value of the trough after the AP. The time difference from the stimulation onset to the first AP's threshold at the rheobase sweep was defined as the AP delay time. The depolarization time was the time difference from the AP threshold to the overshoot. The time from the overshoot to the repolarizing voltage that equaled the threshold was the AP's repolarization time.

The spike-frequency adaptation was calculated with the membrane potential trace in response to the injection of the step current at 2X Rheobase. The interspike interval (ISI) between the first two APs divided by the ISI between the second and the third APs was the initial adaptation index. The ISI

between the first two APs divided by the ISI between the last two APs was the last adaptation index.

**RNA gradient score, electrophysiological score, and latent factor calculation**

RNA gradient score was calculated from the snRNA-seq dataset as reported previously (Li et al., 2020). Briefly, pseudo-time was calculated for all the nuclei in a specific cluster with SCANPY integrated with a software package (scanpy.pp.recipe_zheng17) reported by Zheng et. al.(Zheng et al., 2017). Then, nuclei with the smallest 5% and largest 5% pseudo-time were chosen as two representative populations for the gradient extremes. For each nucleus in a cluster, the median of the Euclidean distances from this nucleus to each nucleus in the two gradient extremes in the principal component analysis (PCA) space (top 3 principal components) was calculated as a gradient score. For each Patch-seq cell mapped to the UMAP space of the snRNA-seq dataset, their gradient score was calculated as the gradient score of the nucleus that had the smallest Euclidean distance to them. To quantify the electrophysiological variance for Patch-seq cells within a cell type, we calculated and assigned an electrophysiological score for each cell as follows. We used their electrophysiological features to perform PCA analysis, and in the resulting PCA space (top 2 principal components), the Euclidean distance from a Patch-seq cell to the Patch-seq cell with the smallest principal components 1 and 2 was calculated as an electrophysiological score. Pearson correlation coefficient (r) and the p-value ($p$) were used to estimate the correlations between gradient score and electrophysiological features or spatial location. The electrophysiological features were standardized with StandardScaler from scikit-learn before performing Pearson correlation analysis. The latent factor was calculated using the FactorAnalysis (scikit-learn) to estimate the likelihood of forming a certain transcriptomic cluster (Guo et al., 2021; Harris et al., 2018; Muñoz-Manchado et al., 2018). The log normalized counts of the top 1,000 highly variable genes in a cluster were used to calculate the latent factor.

**Reduced-rank regression**

Reduced-rank regression (RRR) was analyzed as previously reported (Scala et al., 2021). In brief, we used 16 electrophysiological features and 438 Patch-seq neurons with transcriptomic features to predict

the electrophysiological features from gene expression. The gene counts were log-normalized and the top 1,000 highly variable genes were selected for RRR analysis. For Figure 7A, we used a model with rank r = 5, zero ridge penalty ($\alpha = 1$), and lasso penalty ($\lambda = 0.5$) tuned to yield a selection of 25 genes. For RRR analysis based on the ion channel and G protein-coupled receptor (GPCR) genes, a list of 1745 ion channel and GPCR genes were obtained from https://www.genenames.org/. Among these genes, 477 genes have expression in at least 10 of the Patch-seq neurons and thus were chosen for RRR analysis. A model with rank r = 5, $\alpha = 1$, and $\lambda = 0.45$ was used to yield 25 genes ($\lambda = 0.45$). To predict the morphological features from gene expression, 45 morphological features and 170 recorded neurons were used in the model (r = 5, $\alpha = 1$, and $\lambda = 0.83$) to yield 25 genes. Bibiplots were used to show the RRR analysis results (Scala et al., 2021). Only features with an average correlation above 0.4 were shown and the dots were colored by ME-types of the Patch-seq neurons in the bibiplots.

**Morphological reconstruction and analysis**

Neuronal morphologies were reconstructed with Neurolucida (MicroBrightField) and analyzed with Neurolucida Explorer (including Sholl analysis of the dendritic arbors and the soma shape analysis). For a more comprehensive morphological feature analysis, each morphology file was converted into the SWC format with NLMorphologyConverter 0.9.0 (http://neuronland.org) for feature extraction using MorphoPy (https://github.com/berenslab/MorphoPy). The features used for M-type clustering analysis were shown in Figure S3. See https://github.com/bcmjianglab/cn_project/tree/main/patchseq/M-clusters for a detailed description of the morphological features.

**Register the cell's anatomic location**

To register each Patch-seq cell to the cochlear nucleus (CN) 3D location, we first generated a 3D CN reference space based on the Allen Mouse Brain Atlas and then aligned each brain slice used for our Patch-seq recordings to this CN 3D reference space. We reconstructed a contour on each slice that

delineates the entire cochlear nucleus area in that slice, and then iteratively searched for the contour within the 3D CN reference space that best matched the reconstructed contour (i.e., estimating the 3D location and orientation of that slice). Since our slices were cut in the para-sagittal plane, we limited our grid search parameters range: pitch angle (0, -25 radians) and roll angle (0, -20 radians), median to lateral shift (0, 850 μm), in-plane orientation (-90, 90). For each parameter set, we calculated the overlapping area of the reconstructed contour with the corresponding contour in the 3D CN reference space. The parameters that result in a maximal overlapping area were used as the final parameter for estimation. We visually inspected the mapping results to rule out erroneous registration. For some ambiguous slices (i.e., having very small CN regions), we further limited the search parameter range to improve the accuracy. The location of neurons in that slice was then projected into the 3D CN reference space.

**Machine learning algorithms**

The Random Forest classifier was used to discriminate cell types based on electrophysiological and morphological features. Briefly, the electrophysiological or morphological features of each neuron were extracted, normalized, and scaled. The data were split into training and testing datasets randomly, and the classifier was trained with the training data. The accuracy in distinguishing the cell types by the classifier was evaluated with the testing dataset. The accuracy varied with different training datasets used, so we trained the classifier 10,000 times, each with a different training dataset. The classifier settings with the top 100 performance outcomes were used to weigh the electrophysiological or morphological features for cell type discrimination. The overall accuracy in discriminating cell types by the classifier was reported as the mean accuracy within the chosen settings. The top 15 most important features contributing to the performance were used for UMAP visualizations (Data S2). A confusion matrix was used to show the overall accuracy in distinguishing the cell types by the classifier.

**FISH image analysis and quantification**

Confocal images were captured from FISH-stained brain slices using LSM 710 or 880 confocal microscopes (Zeiss), and the image files (.lsm) containing image stacks were loaded into IDL for analysis of the distribution and co-localization of various mRNA transcripts. From each slice, the images were generated to capture either green fluorescence signals (FITC) or red signals (DIG). The maximum projected image was filtered with a Gaussian filter to remove background signals. To detect a cell with expression signals, cell regions were segmented using a customized IDL code. A cell region with an area smaller than 80 $\mu m^2$ or larger than 800 $\mu m^2$ was not counted as a cell. A cell region with a circularity of less than 0.4 was not counted as a cell either. The circularity of a cell was calculated using the function: $C = 4\pi a^2/p^2$. Here, $C$ is the circularity, $a$ is the area of a cell region and $p$ is the perimeter of the cell region. Cell regions outside the CN area were not included for further analysis. The spatial position of a cell was set as the median of the x or y positions of the pixels within a detected cell region. The fluorescence intensity (F) of a detected cell (either green or red) was set as the mean intensity of all pixels within a detected cell region. After removing fluorescence intensity values within a cell region, the images of each channel were then smoothed by a 60 μm length smoothing window. The smooth images were counted as the background signals of each channel. The background signals ($F_0$) of a detected cell were set as the mean values of the background intensities within a cell region. The intensity differences ($\Delta F$) between F and $F_0$ divided by $F_0$ of a detected cell from both channels (green and red) were used to generate a 2-D scatter plot in Python with each axis representing each channel. From this scatter plot, we used a method similar to the Flow Cytometry gated analysis to determine whether a cell was single-labeled or double-labeled (Method S3). The number of single-labeled and double-labeled cells was calculated across 5-8 consecutive sagittal sections of CN. The distribution of labeled cells (single or double) across CN were quantified through the A-P and D-to-V axis with Jointplot from Seaborn python package. See https://github.com/bcmjianglab/cn_project/tree/main/FISH_analysis for more details about FISH image analysis.

ISH images in Data S3 were acquired from the Allen Mouse Brain Atlas (www.mouse.brain-map.org/)(Lein et al., 2007). Single discriminatory markers were shown for each cell type, with several ISH images being repeated. ISH images were acquired with minor contrast adjustments as needed to maintain image consistency.

## Supplemental figures and legends

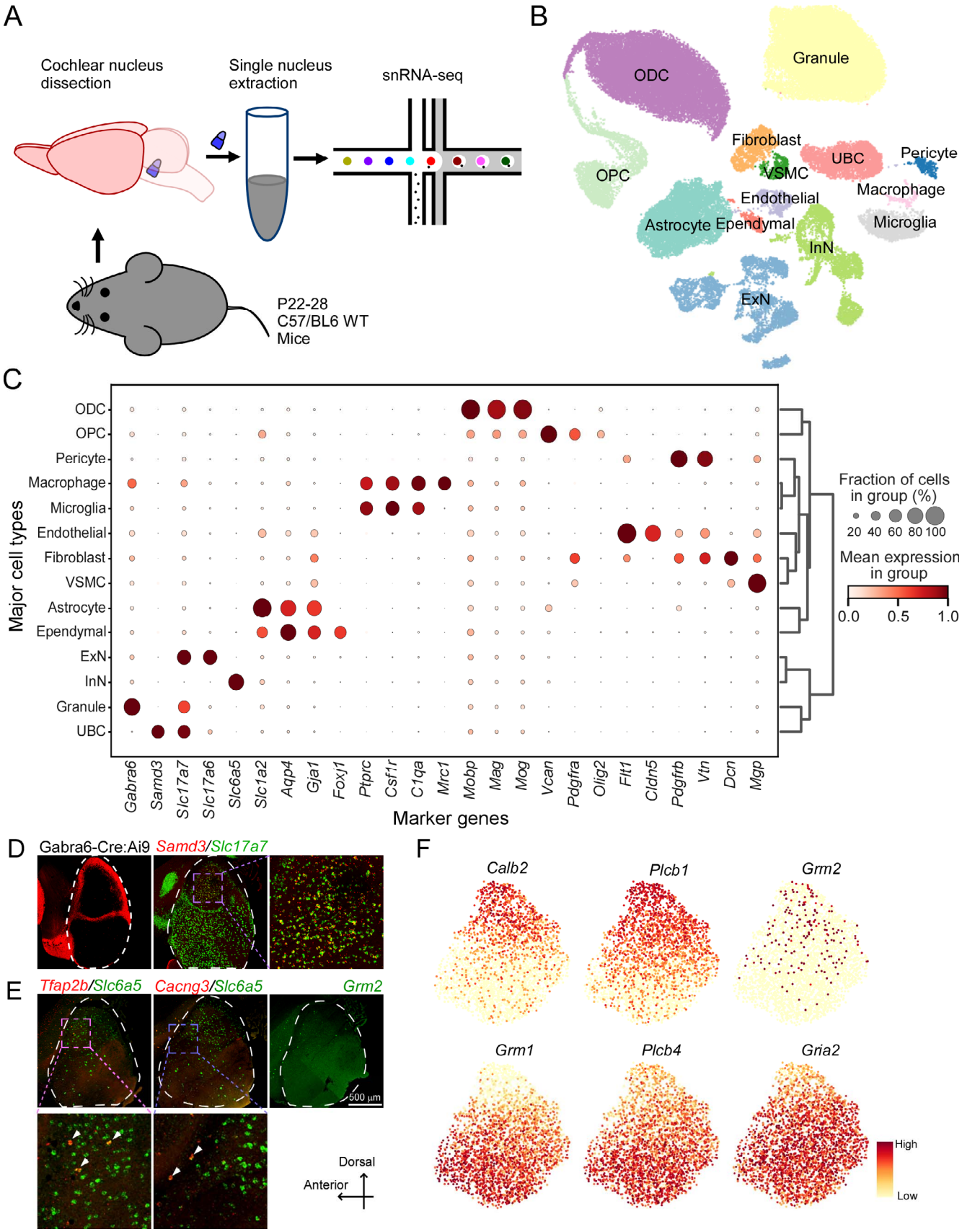

**Figure S1. Single-nucleus transcriptomic profiling of mouse cochlear nucleus. Related to Figure 1.**

**(A)** Flowchart showing an overview of snRNA-seq experimental design, including microdissection of the cochlear nucleus (CN).

**(B)** UMAP visualization of 61,211 nuclei from the CN (after profile quality control, removing nuclei from adjoining brain tissues, and cell type annotation; Methods), colored by cell type identity. ODC, oligodendrocyte; OPC, oligodendrocyte precursor cell; ExN: excitatory neurons; InN: inhibitory neurons; VSMC: vascular smooth muscle cells; Endothelial: endothelial cells; Ependymal: ependymal cells; Granule: Granule cells; UBC: unipolar brush cells.

**(C)** Dendrogram indicating hierarchical relationships between cell types (right) with a dot plot (left) of scaled expression of marker genes for major cell types as shown in (**B**). Cell type assignments, based on the expression of known marker genes, are indicated on the right (also see Table S1). The size of each circle depicts the percentage of cells in the cluster in which the marker was detected (≥ 1 UMI), and its color depicts the average transcript count in expressing cells (nTrans).

**(D)** Left: A representative confocal micrograph showing labeled cells in the CN of Gabra6-Cre:Ai9 mice. Note: labeled cells are restricted to granule cell layer. Middle: FISH co-staining for *Slc17a7* and *Samd3* in a representative sagittal section containing the CN. Note: *Samd3*$^+$ excitatory neurons (*Samd3*$^+$/*Slc17a7*$^+$, yellow signals) were restricted to the deep layer of DCN. Right: A zoom-in view of boxed region of the image in the middle.

**(E)** Top: FISH co-staining for *Tfap2b* and *Slc6a5* (left), or for *Cacng3* and *Slc6a5* (middle), and FISH single-staining for *Grm2* (right) in a representative sagittal section containing CN. Bottom: A zoom-in view of the boxed region of the images on the top. Arrows indicate double-labeled cells (*Tfap2b*$^+$/*Slc6a5*$^+$ or *Cacng3*$^+$/*Slc6a5*$^+$).

**(F)** UMAP visualization of normalized expression of marker genes for OFF UBCs (*Calb2, Plcb1,* and *Grm2*) and for ON UBC (*Grm1, Plcb4,* and *Gria2*).

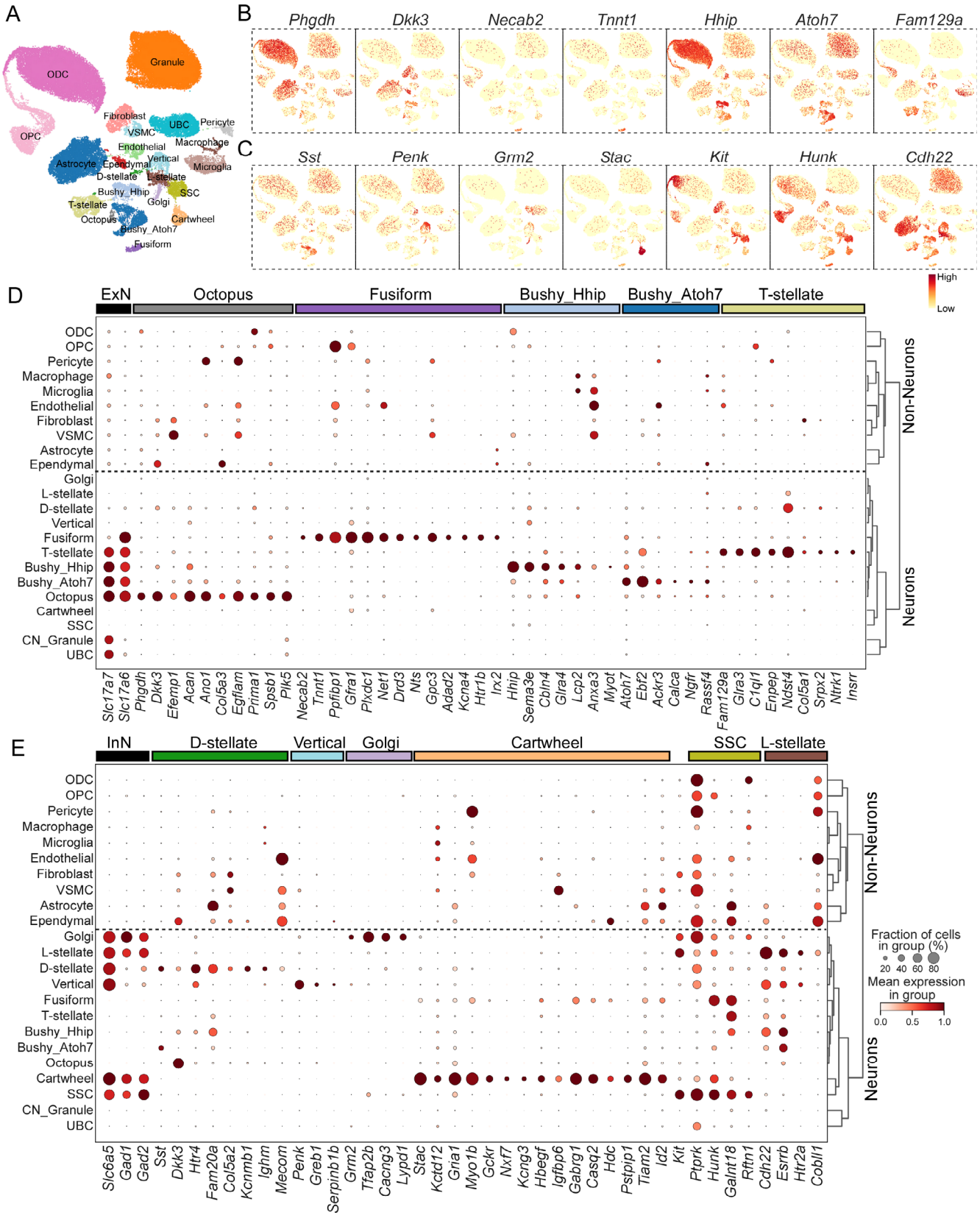


**Figure S2. The expression of marker genes for major CN neuronal types. Related to Figure 3, 4**
**(A)** UMAP visualization of all nuclei from the CN (after profile quality control and annotation; Methods), colored by cell type and cluster identity.
**(B)** UMAP visualization of the normalized expression of the key discriminatory genes for each CN

excitatory cell type across all cell types.

**(C)** UMAP visualization of the expression of the key discriminatory genes for each CN inhibitory cell type across all cell types.

**(D)** Dendrogram indicating hierarchical relationships between cell types (or clusters, right) with a dot plot of scaled expression of selected marker genes for major excitatory cell types (left).

**(E)** Dendrogram indicating hierarchical relationships between cell types (or clusters) with a dot plot of scaled expression of selected marker genes for inhibitory cell types.

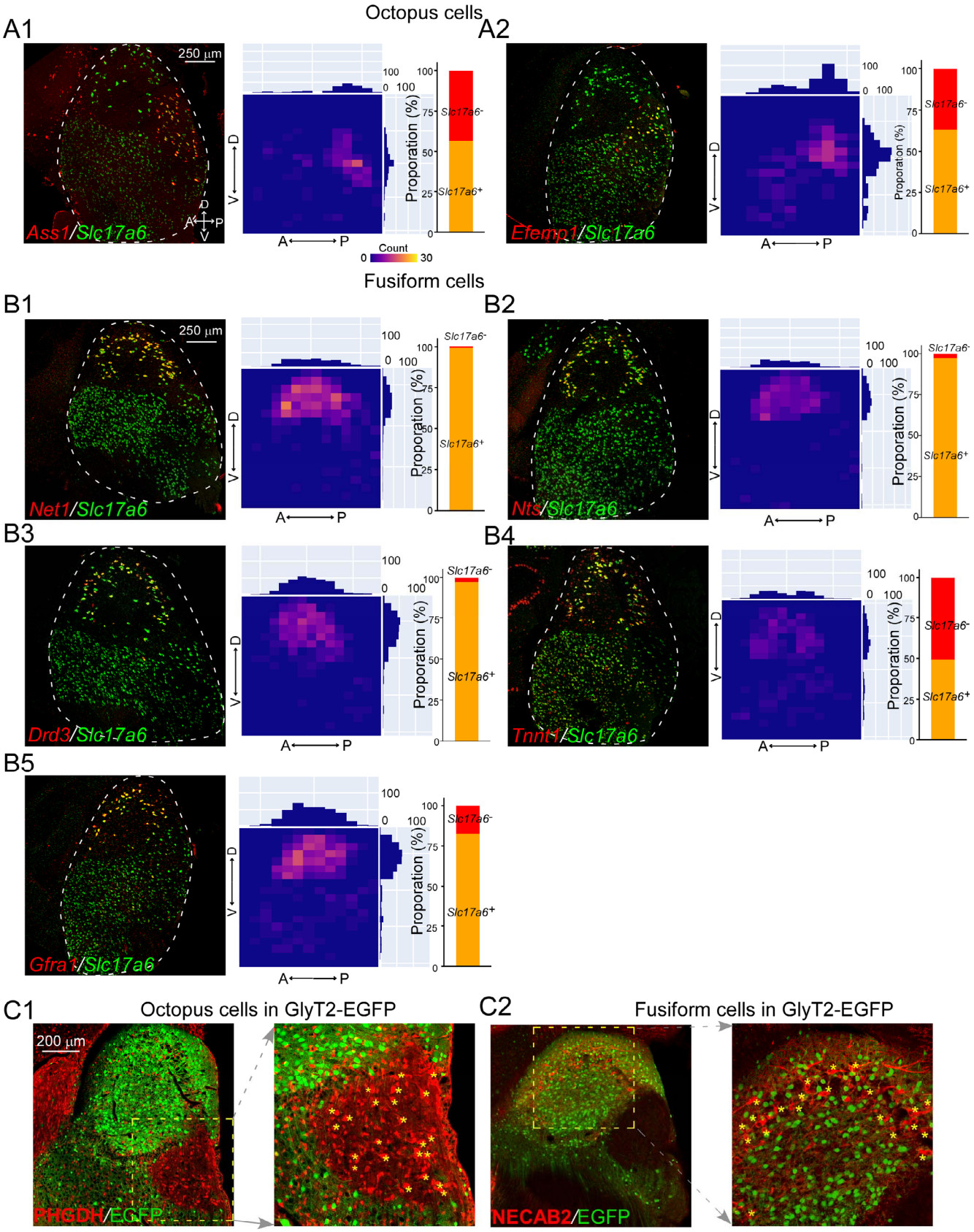


**Figure S3: FISH staining and immunostaining of additional gene markers for fusiform cells and octopus cells. Related to Figure 3.**

**(A1)** Left: FISH co-staining for *Slc17a6* and *Ass1* in a representative sagittal section containing CN. Middle: heatmap shows the density of double-labeled cells across the CN. Right: Bar graph shows the

proportion of double-labeled cells (*Ass1*$^+$/*Slc17a6*$^+$) in all *Ass1*$^+$ cells.

**(A2)** Left: FISH co-staining for *Slc17a6* and *Efemp1* in a representative CN sagittal section. Middle: heatmap shows the density of double-labeled cells across the CN. Right: Bar graph shows the proportion of double-labeled cells (*Efemp1*$^+$/*Slc17a6*$^+$) in all *Efemp1*$^+$ cells.

**(B1)** Left: FISH co-staining for *Slc17a6* and *Net1* in a representative CN sagittal section. Middle: heatmap shows the density of double-labeled cells across the CN. Right: Bar graph shows the proportion of double-labeled cells (*Net1*$^+$/*Slc17a6*$^+$) in all *Net1*$^+$ cells.

**(B2)** Left: FISH co-staining for *Slc17a6* and *Drd3* in a representative CN sagittal section. Middle: heatmap shows the density of double-labeled cells across the CN. Right: Bar graph shows the proportion of double-labeled cells (*Drd3*$^+$/*Slc17a6*$^+$) in all *Drd3*$^+$ cells.

**(B3**) Left: FISH co-staining for *Slc17a6* and *Tnnt1* in a representative CN sagittal section. Middle: heatmap shows the density of double-labeled cells across the CN. Right: Bar graph shows the proportion of double-labeled cells (*Tnnt1*$^+$/*Slc17a6*$^+$) in all *Tnnt1*$^+$ cells.

**(B4)** Left: FISH co-staining for *Slc17a6* and *Nts* in a representative CN sagittal section. Middle: heatmap shows the density of double-labeled cells across the CN. Right: Bar graph shows the proportion of double-labeled cells (*Nts*$^+$/*Slc17a6*$^+$) in all *Nts*$^+$ cells.

**(B5)** Left: FISH co-staining for *Slc17a6* and *Gfra1* in a representative CN sagittal section. Middle: heatmap shows the density of double-labeled cells across the CN. Right: Bar graph shows the proportion of double-labeled cells (*Gfra1*$^+$/*Slc17a6*$^+$) in all *Gfra1*$^+$ cells.

**(C1)** Immunostaining for Phgdh (red) in a representative CN sagittal section from GlyT2-EGFP mice (green EGFP indicates glycinergic neurons). The boxed region is magnified as a micrograph shown on the right. Star signs (*) point to each soma with Phgdh signals. Labeled neurons are restricted to the OCA, which exhibits as a dark area under the fluorescent microscope in GlyT2-EGFP mice due to a lack of glycinergic cells (Ngodup et al., 2020).

**(C2)** Immunostaining for Necab2 (red) in a representative CN sagittal section from GlyT2-EGFP mice. The boxed region is magnified as a micrograph shown on the right. Star signs (*) point to each soma with Necab2 signals.

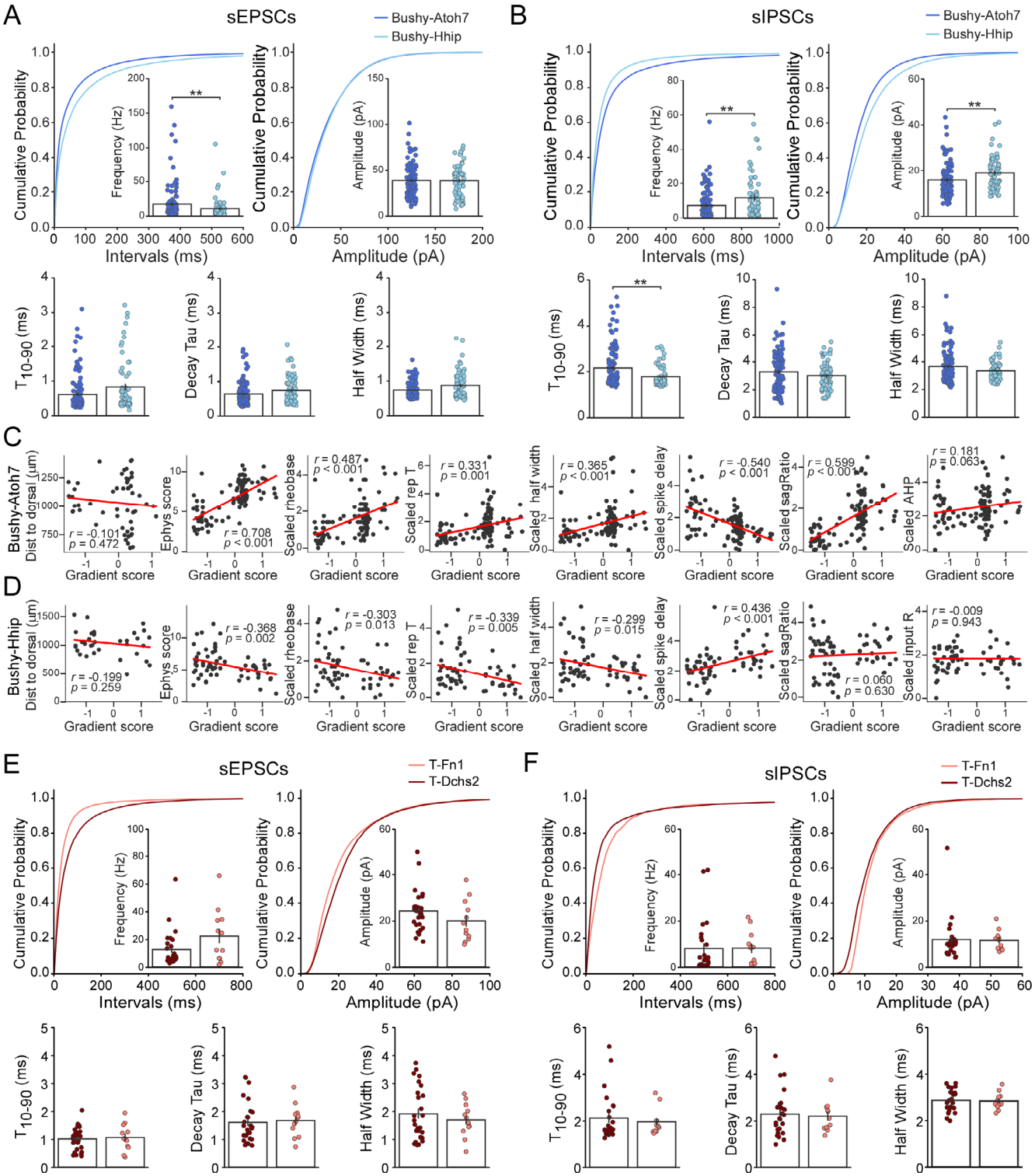


**Figure S4. Phenotypic variability of bushy cells and T-stellate cells. Related to Figure 5, 6**

**(A)** Top: Cumulative fraction analysis of amplitudes and intervals of spontaneous excitatory post-synaptic events (sEPSCs) in two bushy cell subtypes, Bushy-Atoh7 and Bushy-Hhip. Inset bar graphs show the frequency and amplitude of sEPSCs in two subtypes. **p < 0.01. Bottom: Characteristics of sEPSCs from two subtypes, including the 10-90% rise time (T10-90), decay time (decay Tau), and duration (half-width). n = 116 for Bushy-Atoh7; n = 65 for Bushy-Hhip.

**(B)** Top: Cumulative fraction analysis of amplitudes and intervals of spontaneous inhibitory post-synaptic events (sIPSCs) in two bushy cell subtypes. Inset bar graphs show the frequency and amplitude of sIPSCs in two bushy cell subtypes. **p < 0.01. Bottom: Characteristics of sIPSCs from

two subtypes, including the 10-90% rise time (T10-90), decay time (decay Tau), and duration (half-width). n = 114 for Bushy-Atoh7; n = 63 for Bushy-Hhip.

**(C)** From left to right: Correlation between RNA gradient score and the distance to the dorsal edge of VCN of *Atoh7* bushy cells, their electrophysiology score (Ephys score), rheobase values, repolarization time (rep T), AP duration (half-width), spike delay, sag (SagRatio), and AHP. Pearson's correlation test results are shown inside of each plot.

**(D)** From left to right: Correlation between RNA gradient score and the distance to the dorsal edge of VCN of *Hhip*$^+$ bushy cells, their electrophysiology score, rheobase values, repolarization time, AP duration, spike delay, sag, and input resistance (Input R). Pearson's correlation test results are shown inside each plot.

**(E)** Top: Cumulative fraction analysis of amplitudes and intervals of spontaneous excitatory post-synaptic events (sEPSCs) in two T-stellate cell subtypes, T-Fn1 and T-Dchs2. Inset bar graphs show the frequency and amplitude of sEPSCs in two subtypes. Bottom: Characteristics of sEPSCs from two subtypes, including the 10-90% rise time (T10-90), decay time (decay Tau), and duration (half-width). No significant differences were detected between the two groups of cells. n = 23 for T-Fn1; n = 11 for T-Dchs2.

**(F)** Cumulative fraction analysis of amplitudes and intervals of spontaneous inhibitory post-synaptic events (sIPSCs) in two T-cell subtypes. Inset bar graphs show the frequency and amplitude of sIPSCs in two subtypes. Bottom: Characteristics of sIPSCs from two subtypes, including the 10-90% rise time (T10-90), decay time (decay Tau), and duration (half-width). There is no significant difference between the two groups of cells. n = 23 for T-Fn1; n = 12 for T-Dchs2.

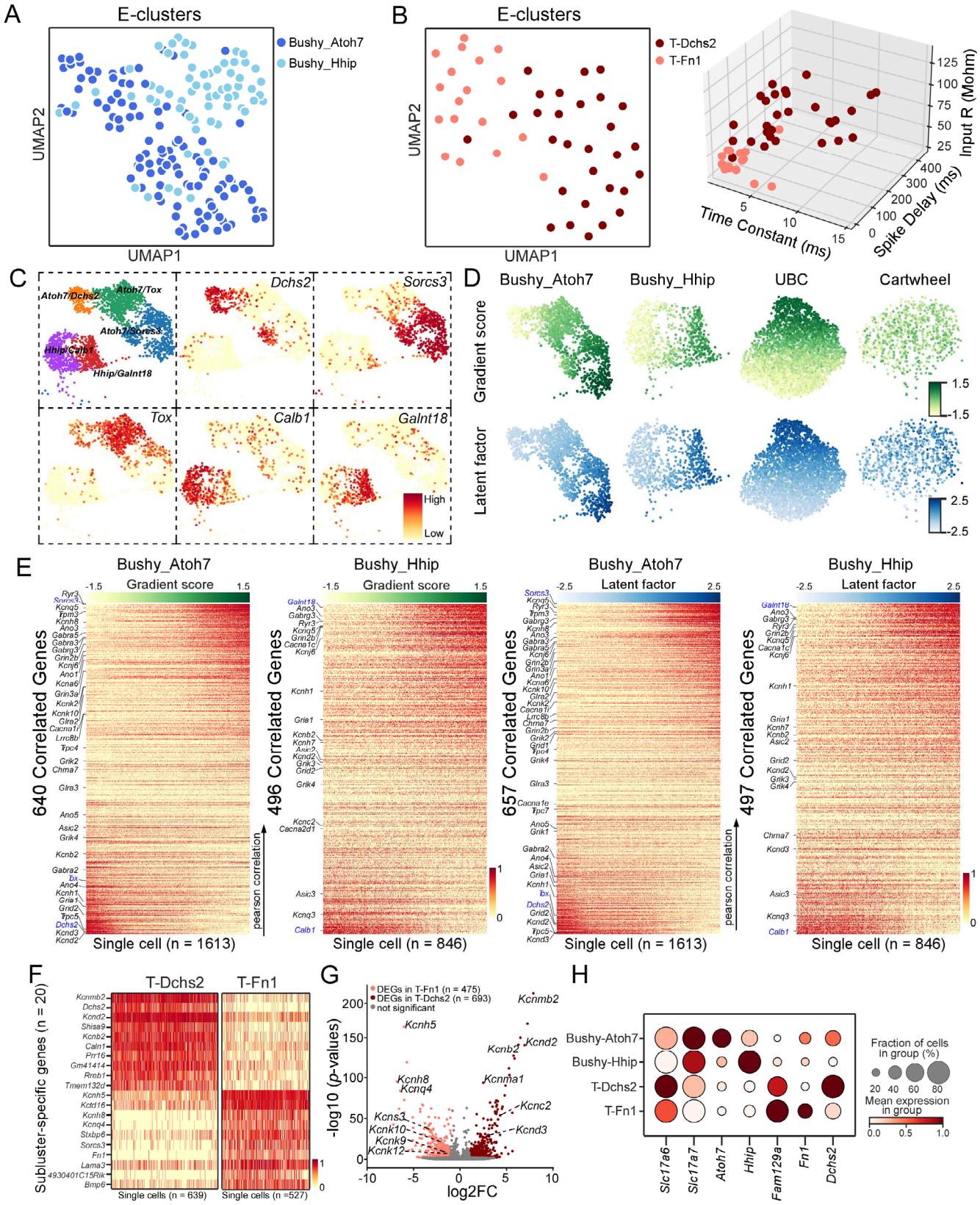


**Figure S5. Molecular variation of bushy cells and T-stellate cells. Related to Figure 5, 6**

**(A)** UMAP visualization of bushy cells clustered by over-dispersed electrophysiological features, colored by bushy cell subtypes.

**(B)** Left: UMAP visualization of T-stellate cells clustered by over-dispersed electrophysiological

features, colored by T-stellate cell subtypes. Right: 3D plot of T-stellate cell electrophysiological features.

**(C)** Top left: UMAP visualization of five bushy cell subclusters, each marked with a combination of two discriminating genes. Rest: UMAP visualization of the expression (normalized) of the marker genes (*Dchs2*, *Sorcs3*, *Tox*, *Calb1*, and *Galnt18*) for each subcluster.

**(D)** UMAP visualization of the gradient score and the latent factor of *Atoh7* bushy cells (Bushy_Atoh7), *Hhip* bushy cells (Bushy_Hhip), UBCs, and cartwheel cells.

**(E)** Left: Heat map showing normalized expression of the genes (with the top 1,000 highly variable genes) having a significant correlation with gradient scores (Pearson correlations, $r \neq 0$ and $p < 0.05$) in either *Atoh7*$^+$ or *Hhip*$^+$ bushy cell subtype. The genes encoding ion channels and the markers for the bushy cell subtypes were highlighted on the side with black and blue colors, respectively. Columns: single nuclei, ordered by the gradient score; Rows: genes, ordered by the Pearson correlations (r). Right: Heat map showing normalized expression of the genes having significant correlations with the latent factors (Pearson correlations, $r \neq 0$ and $p < 0.05$) in either *Atoh7*$^+$ or *Hhip*$^+$ bushy cell subtype. The genes encoding ion channels and bushy cell subtype markers are highlighted on the side with black and blue colors, respectively. Columns: single nuclei, ordered by the latent factor; Rows: genes, ordered by the Pearson correlations (r).

**(F)** Heat map showing normalized expression of the top 20 differentially expressed (DE) genes for two T-stellate subclusters. Scale bar: Log2 (Expression level). The cell number in each subcluster is indicated below the figure.

**(G)** Volcano plot showing the log2 fold change (log2FC) and -log10(*p*-value) (corrected for FDR) of detected genes comparing T-Fn1 to T- Dchs2. Those genes (n = 475) whose expression are significantly higher ($p < 0.01$ and log2FC < -1) in T-Fn1 are dots in light brown, and those (n = 693) with an expression significantly higher ($p < 0.01$ and log2FC > 1) in T-Dchs2 are dots in dark brown. The gray dots represent those genes that are not significantly differentiated expressed between two subtypes. Among DEGs are 13 genes related to potassium channels as labeled in the plot.

**(H)** Dot plot showing the expression patterns of bushy cells and T-stellate subtype marker genes in Patch-seq bushy and T-stellate cell subclusters.

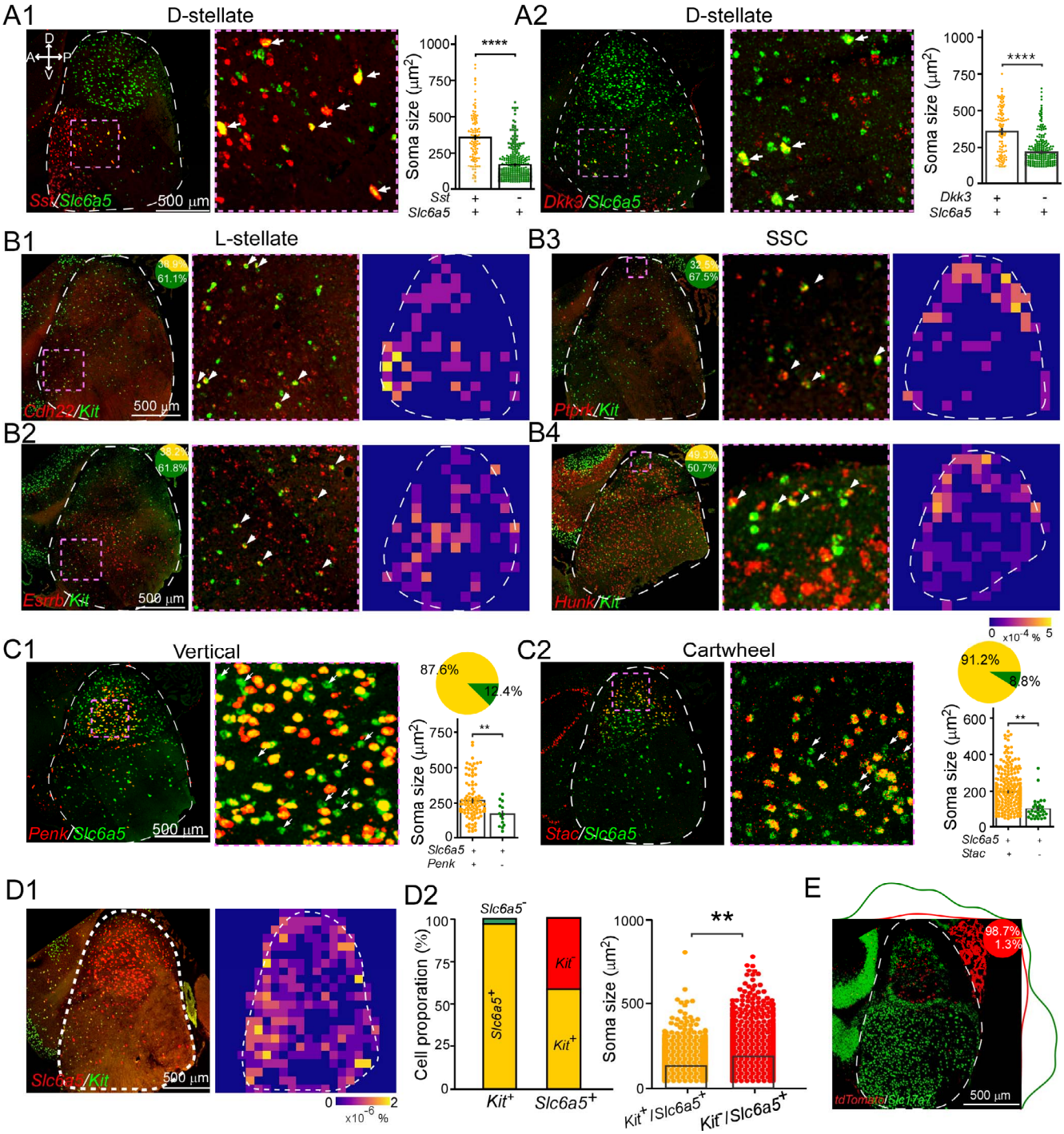


**Figure S6: FISH signals of marker genes for inhibitory cell types. Related to Figure 4.**

**(A1)** Left: FISH co-staining for *Sst* and *Slc6a5* in a representative CN sagittal section. Scale bar also applies to A2. Middle: A zoom-in view of boxed region shown on the left. Arrows point to double-labeled cells. Right: Comparison of the soma size of $Sst^+$ glycinergic neurons ($Sst^+/Slc6a5^+$) to $Sst^-$ glycinergic neurons ($Sst^-/Slc6a5^+$). ****$p < 0.0001$ with t-test.

**(A2)** Left: FISH co-staining for *Dkk3* and *Slc6a5* in a representative CN sagittal section. Middle: A zoom-in view of boxed area shown on the left. Arrows point to double-labeled cells. Right: Comparison of the soma size of $Dkk3^+$ glycinergic neurons ($Dkk3^+/Slc6a5^+$) to $Dkk3^-$ glycinergic neurons ($Dkk3^-/Slc6a5^+$). ****$p < 0.0001$ with t-test.

**(B1)** Left: FISH co-staining for *Cdh22* and *Kit* in a representative CN sagittal section. The scale bar applies to B1-B4. Inset pie chart shows the proportion of double-labeled cells ($Cdh22^+/Kit^+$) in all $Kit^+$

cells across 7 consecutive sections. Middle: A zoom-in view of boxed region shown on the left. Arrows point to double-labeled cells. Right: The distribution of the double-labeled cells across the CN.

**(B2)** Left: FISH co-staining for *Esrrb* and *Kit* in a representative CN sagittal section. Inset pie chart shows the proportion of double-labeled cells (*Esrrb*$^+$/*Kit*$^+$) in all *Kit*$^+$ cells across 8 consecutive sections. Middle: A zoom-in view of boxed region shown on the left. Arrows point to double-labeled cells. Right: The distribution of the double-labeled cells across the CN.

**(B3)** Left: FISH co-staining for *Ptprk* and *Kit* in a representative CN sagittal section. Inset pie chart shows the proportion of double-labeled cells (*Ptprk*$^+$/*Kit*$^+$) in all *Kit*$^+$ cells across 8 consecutive sections. Middle: A zoom-in view of boxed region shown on the left. Arrows point to double-labeled cells. Right: The distribution of the double-labeled cells across the CN.

**(B4)** Left: FISH co-staining for *Hunk* and *Kit* in a representative CN sagittal section. Inset pie chart shows the proportion of double-labeled cells (*Hunk*$^+$/*Kit*$^+$) in all *Kit*$^+$ cells across 8 consecutive sections. Middle: A zoom-in view of boxed region shown on the left. Arrows point to double-labeled cells. Right: The distribution of the double-labeled cells across the CN.

**(C1)** Left: FISH co-staining for *Slc6a5* and *Penk* in a representative CN sagittal section. Middle: A zoom-in view of boxed area shown on the left. Arrows point to those *Penk*$^-$/*Slc6a5*$^+$ cells. Right: The soma size of *Penk*$^-$/*Slc6a5*$^+$ cells and *Penk*$^+$/*Slc6a5*$^+$ cells. The pie chart shows the proportion of *Penk*$^-$ glycinergic neurons and *Penk*$^+$ glycinergic neurons in deep layer of DCN across 5 consecutive sections.

**(C2)** Left: FISH co-staining for *Slc6a5* and *Stac* in a representative CN sagittal section. Middle: A zoom-in view of boxed area shown on the left. Arrows point to those *Stac*$^-$/*Slc6a5*$^+$ cells. Right: The soma size of *Stac*$^-$/*Slc6a5*$^+$ cells and *Stac*$^+$/*Slc6a5*$^+$ cells. The pie chart shows the proportion of *Stac*$^-$ glycinergic neurons and *Stac*$^+$ glycinergic neurons in DCN across 6 consecutive sections.

**(D1)** Left: FISH co-staining for *Slc6a5* and *Kit* in a representative CN sagittal section. Right: The distribution of double-labeled cells (*Slc6a5*$^+$/*Kit*$^+$) across the CN.

**(D2)** Left: Bar graphs show the proportion of double-labeled cells (*Slc6a5*$^+$/*Kit*$^+$) and single-labeled cells (*Slc6a5*$^-$/*Kit*$^+$) in all *Kit*$^+$ cells across all 6 consecutive sections and the proportion of *Kit*$^+$ glycinergic neurons (*Slc6a5*$^+$/*Kit*$^+$) and *Kit*$^-$ glycinergic neurons (*Kit*$^-$/*Slc6a5*$^+$) in all glycinergic cells (*Slc6a5*$^+$) across all 6 consecutive sections. Note: only 2.8% of *Kit*$^+$ cells are *Slc6a5*$^-$. Right: The soma size of *Kit*$^+$ glycinergic neurons (*Kit*$^+$/*Slc6a5*$^+$) and *Kit*$^-$ glycinergic neurons (*Kit*$^-$/*Slc6a5*$^+$). **$p < 0.01$ with t-test.

**(E)** FISH co-staining for *Slc17a7* and *tdTomato* in a representative CN sagittal section from Penk-Cre: Ai9 mice. Inset pie charts show the proportion of double-labeled cells in all *tdTomato*$^+$ cells across 7 consecutive sections. Colored lines along FISH images show the density of double-labeled neurons (yellow) or single-labeled cells (green or red) along two axes of the CN.

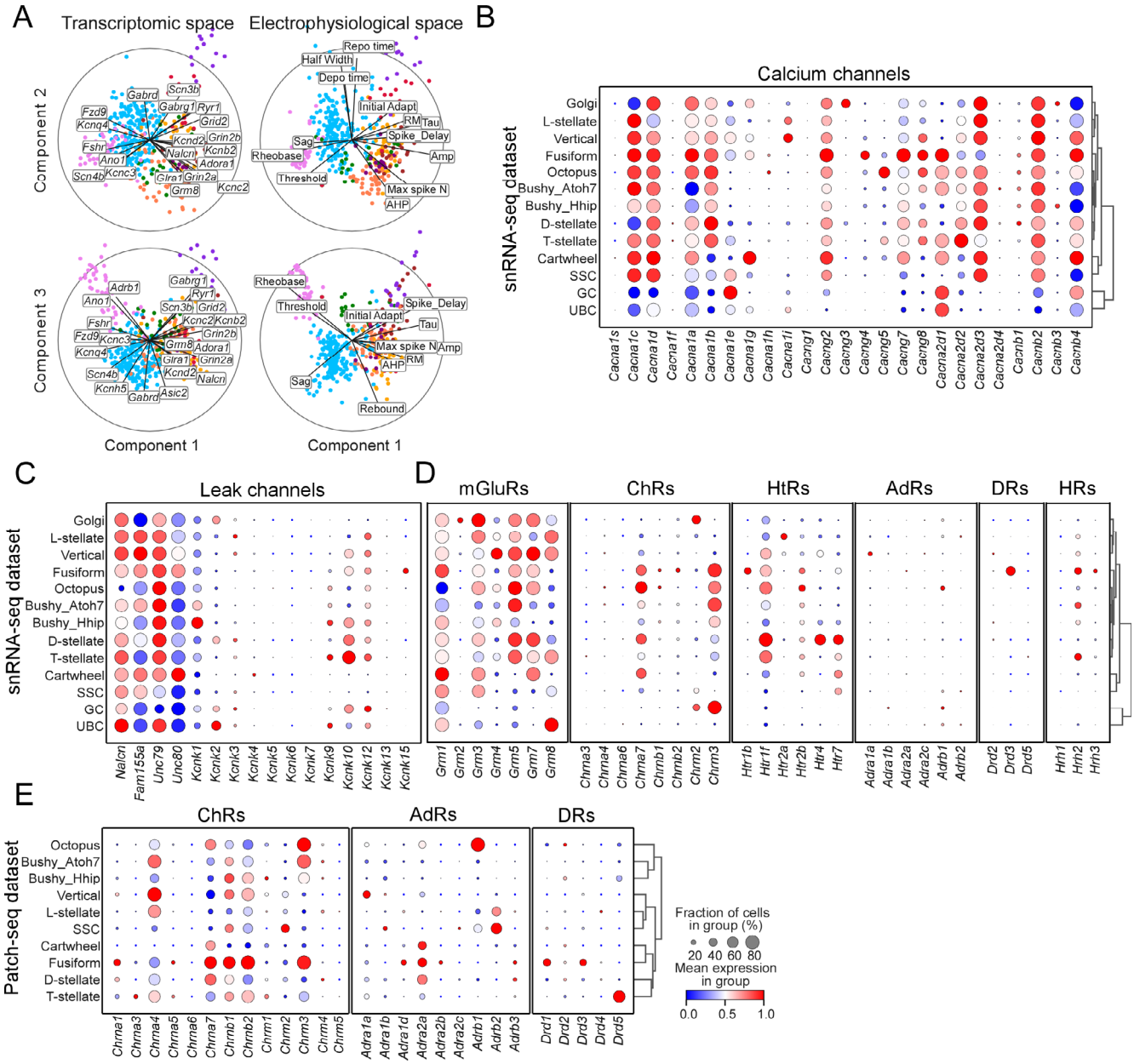


**Figure S7: Single-cell transcriptomes provide insights into functional specializations of CN cell types**

**(A)** A sparse reduced-rank regression (RRR) model to predict electrophysiological features using the expression patterns of 330 ion channels and 1415 GPCR genes. The model selected 25 genes. The cross-correlation results were presented as a pair of biplots, or bibiplot (left: transcriptome, right: electrophysiology). In each biplot, lines represent correlations between each electrophysiological property and two components; the circle corresponds to the maximum attainable correlation (r =1). Only features with an average correlation above 0.4 are shown.

**(B)** Dot plot showing scaled expression of the genes encoding calcium channels across CN cell types (from snRNA-seq dataset).

**(C)** Dot plot showing scaled expression of the genes encoding leak channels across CN cell types (from snRNA-seq dataset).

**(D)** Dot plot showing scaled expression of the genes encoding metabotropic glutamate receptors (mGluR), cholinergic receptors (ChRs), serotonergic receptors (HtRs), adrenergic receptors (AdRs), dopaminergic receptors (DRs), and histaminergic receptors (HRs) across CN cell types (from snRNA-seq dataset).

**(E)** Dot plot showing scaled expression of the genes encoding cholinergic (ChRs), adrenergic (AdRs), and dopaminergic (DRs) receptors across CN cell types (from Patch-seq dataset). The Patch-seq data generally agree with our snRNA-seq data but detected a higher expression of several receptors in additional cell types, consistent with the more sequencing depth in Patch-seq compared to the 10X drop-seq protocol.

## References


Akagi, H., Hirai, K., and Hishinuma, F. (1991). Cloning of a glycine receptor subtype expressed in rat brain and spinal cord during a specific period of neuronal development. FEBS Lett *281*, 160-166.

Akter, N., Adachi, R., Kato, A., Fukaya, R., and Kuba, H. (2018). Auditory Input Shapes Tonotopic Differentiation of Kv1.1 Expression in Avian Cochlear Nucleus during Late Development. J Neurosci *38*, 2967-2980.

Apostolides, P.F., and Trussell, L.O. (2014). Chemical synaptic transmission onto superficial stellate cells of the mouse dorsal cochlear nucleus. J Neurophysiol *111*, 1812-1822.

Bal, R., and Oertel, D. (2000). Hyperpolarization-activated, mixed-cation current (I(h)) in octopus cells of the mammalian cochlear nucleus. J Neurophysiol *84*, 806-817.

Bal, R., and Oertel, D. (2001). Potassium currents in octopus cells of the mammalian cochlear nucleus. J Neurophysiol *86*, 2299-2311.

Bellingham, M.C., Lim, R., and Walmsley, B. (1998). Developmental changes in EPSC quantal size and quantal content at a central glutamatergic synapse in rat. The Journal of physiology *511 ( Pt 3)*, 861-869.

Blum, J.A., Klemm, S., Shadrach, J.L., Guttenplan, K.A., Nakayama, L., Kathiria, A., Hoang, P.T., Gautier, O., Kaltschmidt, J.A., Greenleaf, W.J.*, et al.* (2021). Single-cell transcriptomic analysis of the adult mouse spinal cord reveals molecular diversity of autonomic and skeletal motor neurons. Nat Neurosci *24*, 572-583.

Borges-Merjane, C., and Trussell, L.O. (2015). ON and OFF unipolar brush cells transform multisensory inputs to the auditory system. Neuron *85*, 1029-1042.

Brownell, W.E. (1975). Organization of the cat trapezoid body and the discharge characteristics of its fibers. Brain Res *94*, 413-433.

Butler, B., and Lomber, S. (2013). Functional and structural changes throughout the auditory system following congenital and early-onset deafness: implications for hearing restoration. Frontiers in Systems Neuroscience *7*.

Cadwell, C.R., Palasantza, A., Jiang, X., Berens, P., Deng, Q., Yilmaz, M., Reimer, J., Shen, S., Bethge, M., Tolias, K.F.*, et al.* (2016). Electrophysiological, transcriptomic and morphologic profiling of single neurons using Patch-seq. Nat Biotechnol *34*, 199-203.

Cadwell, C.R., Scala, F., Fahey, P.G., Kobak, D., Mulherkar, S., Sinz, F.H., Papadopoulos, S., Tan, Z.H., Johnsson, P., Hartmanis, L.*, et al.* (2020). Cell type composition and circuit organization of clonally related excitatory neurons in the juvenile mouse neocortex. Elife *9*.

Cadwell, C.R., Scala, F., Li, S., Livrizzi, G., Shen, S., Sandberg, R., Jiang, X., and Tolias, A.S. (2017). Multimodal profiling of single-cell morphology, electrophysiology, and gene expression using Patch-seq. Nat Protoc *12*, 2531-2553.

Calhoun, J.D., and Isom, L.L. (2014). The role of non-pore-forming β subunits in physiology and pathophysiology of voltage-gated sodium channels. Handbook of experimental pharmacology *221*, 51-89.

Callaway, E.M., Dong, H.-W., Ecker, J.R., Hawrylycz, M.J., Huang, Z.J., Lein, E.S., Ngai, J., Osten, P., Ren, B., Tolias, A.S.*, et al.* (2021). A multimodal cell census and atlas of the mammalian primary motor cortex. Nature *598*, 86-102.

Campbell, J.N., Macosko, E.Z., Fenselau, H., Pers, T.H., Lyubetskaya, A., Tenen, D., Goldman, M., Verstegen, A.M., Resch, J.M., McCarroll, S.A.*, et al.* (2017). A molecular census of arcuate hypothalamus and median eminence cell types. Nat Neurosci *20*, 484-496.

Campos, M.L., de Cabo, C., Wisden, W., Juiz, J.M., and Merlo, D. (2001). Expression of GABAA receptor subunits in rat brainstem auditory pathways: cochlear nuclei, superior olivary complex and nucleus of the lateral lemniscus. Neuroscience *102*, 625-638.
Cant, N.B. (1993). The synaptic organization of the ventral cochlear nucleus of the cat: the peripheral cap of small cells. In The Mammalian Cochlear Nuclei (Springer), pp. 91-105.
Cao, X.J., and Oertel, D. (2010). Auditory nerve fibers excite targets through synapses that vary in convergence, strength, and short-term plasticity. J Neurophysiol *104*, 2308-2320.
Cao, X.J., and Oertel, D. (2011). The magnitudes of hyperpolarization-activated and low-voltage-activated potassium currents co-vary in neurons of the ventral cochlear nucleus. J Neurophysiol *106*, 630-640.
Cao, X.J., Shatadal, S., and Oertel, D. (2007). Voltage-sensitive conductances of bushy cells of the Mammalian ventral cochlear nucleus. J Neurophysiol *97*, 3961-3975.
Cembrowski, M.S., Bachman, J.L., Wang, L., Sugino, K., Shields, B.C., and Spruston, N. (2016). Spatial Gene-Expression Gradients Underlie Prominent Heterogeneity of CA1 Pyramidal Neurons. Neuron *89*, 351-368.
Das, G., Yu, Q., Hui, R., Reuhl, K., Gale, N.W., and Zhou, R. (2016). EphA5 and EphA6: regulation of neuronal and spine morphology. Cell & Bioscience *6*, 48.
DeFelipe, J., López-Cruz, P.L., Benavides-Piccione, R., Bielza, C., Larrañaga, P., Anderson, S., Burkhalter, A., Cauli, B., Fairén, A., Feldmeyer, D.*, et al.* (2013). New insights into the classification and nomenclature of cortical GABAergic interneurons. Nature Reviews Neuroscience *14*, 202-216.
Dobin, A., Davis, C.A., Schlesinger, F., Drenkow, J., Zaleski, C., Jha, S., Batut, P., Chaisson, M., and Gingeras, T.R. (2013). STAR: ultrafast universal RNA-seq aligner. Bioinformatics *29*, 15-21.
Doucet, J.R., and Ryugo, D.K. (1997). Projections from the ventral cochlear nucleus to the dorsal cochlear nucleus in rats. The Journal of comparative neurology *385*, 245-264.
Englund, C., Kowalczyk, T., Daza, R.A.M., Dagan, A., Lau, C., Rose, M.F., and Hevner, R.F. (2006). Unipolar Brush Cells of the Cerebellum Are Produced in the Rhombic Lip and Migrate through Developing White Matter. The Journal of Neuroscience *26*, 9184-9195.
Ferragamo, M.J., Golding, N.L., and Oertel, D. (1998). Synaptic inputs to stellate cells in the ventral cochlear nucleus. J Neurophysiol *79*, 51-63.
Fujino, K., and Oertel, D. (2001). Cholinergic modulation of stellate cells in the mammalian ventral cochlear nucleus. J Neurosci *21*, 7372-7383.
Futai, K., Okada, M., Matsuyama, K., and Takahashi, T. (2001). High-fidelity transmission acquired via a developmental decrease in NMDA receptor expression at an auditory synapse. J Neurosci *21*, 3342-3349.
Gardner, S.M., Trussell, L.O., and Oertel, D. (1999). Time course and permeation of synaptic AMPA receptors in cochlear nuclear neurons correlate with input. J Neurosci *19*, 8721-8729.
Gardner, S.M., Trussell, L.O., and Oertel, D. (2001). Correlation of AMPA receptor subunit composition with synaptic input in the mammalian cochlear nuclei. J Neurosci *21*, 7428-7437.
Gates, T.S., Weedman, D.L., Pongstaporn, T., and Ryugo, D.K. (1996). Immunocytochemical localization of glycine in a subset of cartwheel cells of the dorsal cochlear nucleus in rats. Hear Res *96*, 157-166.
Golding, N.L., Ferragamo, M.J., and Oertel, D. (1999). Role of intrinsic conductances underlying responses to transients in octopus cells of the cochlear nucleus. J Neurosci *19*, 2897-2905.
Golding, N.L., and Oertel, D. (1997). Physiological identification of the targets of cartwheel cells in the dorsal cochlear nucleus. J Neurophysiol *78*, 248-260.
Gouwens, N.W., Sorensen, S.A., Baftizadeh, F., Budzillo, A., Lee, B.R., Jarsky, T., Alfiler, L., Baker, K., Barkan, E., Berry, K.*, et al.* (2020). Integrated Morphoelectric and Transcriptomic Classification of Cortical GABAergic Cells. Cell *183*, 935-953 e919.

Goyer, D., Kurth, S., Gillet, C., Keine, C., Rübsamen, R., and Kuenzel, T. (2016). Slow Cholinergic Modulation of Spike Probability in Ultra-Fast Time-Coding Sensory Neurons. eNeuro *3*.
Griffiths, T.D. (2002). Central auditory processing disorders. Curr Opin Neurol *15*, 31-33.
Guo, C., Huson, V., Macosko, E.Z., and Regehr, W.G. (2021). Graded heterogeneity of metabotropic signaling underlies a continuum of cell-intrinsic temporal responses in unipolar brush cells. Nature Communications *12*, 5491.
Hancock, K.E., and Voigt, H.F. (2002). Intracellularly labeled fusiform cells in dorsal cochlear nucleus of the gerbil. II. Comparison of physiology and anatomy. J Neurophysiol *87*, 2520-2530.
Harris, K.D., Hochgerner, H., Skene, N.G., Magno, L., Katona, L., Bengtsson Gonzales, C., Somogyi, P., Kessaris, N., Linnarsson, S., and Hjerling-Leffler, J. (2018). Classes and continua of hippocampal CA1 inhibitory neurons revealed by single-cell transcriptomics. PLoS biology *16*, e2006387.
Henze, D.A., and Buzsaki, G. (2001). Action potential threshold of hippocampal pyramidal cells in vivo is increased by recent spiking activity. Neuroscience *105*, 121-130.
Irie, T., Fukui, I., and Ohmori, H. (2006). Activation of GIRK channels by muscarinic receptors and group II metabotropic glutamate receptors suppresses Golgi cell activity in the cochlear nucleus of mice. J Neurophysiol *96*, 2633-2644.
Isaacson, J.S., and Walmsley, B. (1995). Receptors underlying excitatory synaptic transmission in slices of the rat anteroventral cochlear nucleus. J Neurophysiol *73*, 964-973.
Jiang, X., Shen, S., Cadwell, C.R., Berens, P., Sinz, F., Ecker, A.S., Patel, S., and Tolias, A.S. (2015). Principles of connectivity among morphologically defined cell types in adult neocortex. Science *350*, aac9462.
Johnston, J., Forsythe, I.D., and Kopp-Scheinpflug, C. (2010). Going native: voltage-gated potassium channels controlling neuronal excitability. The Journal of physiology *588*, 3187-3200.
Johnston, J., Griffin, S.J., Baker, C., and Forsythe, I.D. (2008a). Kv4 (A-type) potassium currents in the mouse medial nucleus of the trapezoid body. European Journal of Neuroscience *27*, 1391-1399.
Johnston, J., Griffin, S.J., Baker, C., Skrzypiec, A., Chernova, T., and Forsythe, I.D. (2008b). Initial segment Kv2.2 channels mediate a slow delayed rectifier and maintain high frequency action potential firing in medial nucleus of the trapezoid body neurons. The Journal of physiology *586*, 3493-3509.
Joshi, I., and Wang, L.Y. (2002). Developmental profiles of glutamate receptors and synaptic transmission at a single synapse in the mouse auditory brainstem. The Journal of physiology *540*, 861-873.
Karmakar, K., Narita, Y., Fadok, J., Ducret, S., Loche, A., Kitazawa, T., Genoud, C., Di Meglio, T., Thierry, R., Bacelo, J.*, et al.* (2017). Hox2 Genes Are Required for Tonotopic Map Precision and Sound Discrimination in the Mouse Auditory Brainstem. Cell Rep *18*, 185-197.
Kato, K. (1990). Novel GABAA receptor α subunit is expressed only in cerebellar granule cells. Journal of Molecular Biology *214*, 619-624.
Kharkovets, T., Hardelin, J.-P., Safieddine, S., Schweizer, M., El-Amraoui, A., Petit, C., and Jentsch, T.J. (2000). KCNQ4, a K<sup>+</sup> channel mutated in a form of dominant deafness, is expressed in the inner ear and the central auditory pathway. Proceedings of the National Academy of Sciences *97*, 4333-4338.
Kim, D.W., Yao, Z., Graybuck, L.T., Kim, T.K., Nguyen, T.N., Smith, K.A., Fong, O., Yi, L., Koulena, N., Pierson, N.*, et al.* (2019). Multimodal Analysis of Cell Types in a Hypothalamic Node Controlling Social Behavior. Cell *179*, 713-728 e717.
Kobak, D., and Berens, P. (2019). The art of using t-SNE for single-cell transcriptomics. Nature Communications *10*, 5416.
Kobak, D., Bernaerts, Y., Weis, M.A., Scala, F., Tolias, A.S., and Berens, P. (2021). Sparse reduced‐rank regression for exploratory visualisation of paired multivariate data. Journal of the Royal Statistical Society Series C *70*, 980-1000.

Koch, U., Braun, M., Kapfer, C., and Grothe, B. (2004). Distribution of HCN1 and HCN2 in rat auditory brainstem nuclei. The European journal of neuroscience *20*, 79-91.
Kolston, J., Osen, K.K., Hackney, C.M., Ottersen, O.P., and Storm-Mathisen, J. (1992). An atlas of glycine- and GABA-like immunoreactivity and colocalization in the cochlear nuclear complex of the guinea pig. Anat Embryol (Berl) *186*, 443-465.
Korsunsky, I., Millard, N., Fan, J., Slowikowski, K., Zhang, F., Wei, K., Baglaenko, Y., Brenner, M., Loh, P.R., and Raychaudhuri, S. (2019). Fast, sensitive and accurate integration of single-cell data with Harmony. Nat Methods *16*, 1289-1296.
Kossl, M., and Vater, M. (1989). Noradrenaline enhances temporal auditory contrast and neuronal timing precision in the cochlear nucleus of the mustached bat. J Neurosci *9*, 4169-4178.
Kozareva, V., Martin, C., Osorno, T., Rudolph, S., Guo, C., Vanderburg, C., Nadaf, N., Regev, A., Regehr, W.G., and Macosko, E. (2021). A transcriptomic atlas of mouse cerebellar cortex comprehensively defines cell types. Nature *598*, 214-219.
Krishnaswami, S.R., Grindberg, R.V., Novotny, M., Venepally, P., Lacar, B., Bhutani, K., Linker, S.B., Pham, S., Erwin, J.A., Miller, J.A.*, et al.* (2016). Using single nuclei for RNA-seq to capture the transcriptome of postmortem neurons. Nat Protoc *11*, 499-524.
Laturnus, S., von Daranyi, A., Huang, Z., and Berens, P. (2020). MorphoPy: A python package for feature extraction of neural morphologies. Journal of Open Source Software *5*, 2339.
Lau, D., Miera, E.V.-S.d., Contreras, D., Ozaita, A., Harvey, M., Chow, A., Noebels, J.L., Paylor, R., Morgan, J.I., Leonard, C.S.*, et al.* (2000). Impaired Fast-Spiking, Suppressed Cortical Inhibition, and Increased Susceptibility to Seizures in Mice Lacking Kv3.2 K<sup>+</sup> Channel Proteins. The Journal of Neuroscience *20*, 9071-9085.
Lauer, A.M., Connelly, C.J., Graham, H., and Ryugo, D.K. (2013). Morphological characterization of bushy cells and their inputs in the laboratory mouse (Mus musculus) anteroventral cochlear nucleus. PLoS One *8*, e73308.
Lehman, A., Thouta, S., Mancini, G.M.S., Naidu, S., van Slegtenhorst, M., McWalter, K., Person, R., Mwenifumbo, J., Salvarinova, R., Guella, I.*, et al.* (2017). Loss-of-Function and Gain-of-Function Mutations in KCNQ5 Cause Intellectual Disability or Epileptic Encephalopathy. American journal of human genetics *101*, 65-74.
Lein, E.S., Hawrylycz, M.J., Ao, N., Ayres, M., Bensinger, A., Bernard, A., Boe, A.F., Boguski, M.S., Brockway, K.S., Byrnes, E.J.*, et al.* (2007). Genome-wide atlas of gene expression in the adult mouse brain. Nature *445*, 168-176.
Li, Y., Lopez-Huerta, V.G., Adiconis, X., Levandowski, K., Choi, S., Simmons, S.K., Arias-Garcia, M.A., Guo, B., Yao, A.Y., Blosser, T.R.*, et al.* (2020). Distinct subnetworks of the thalamic reticular nucleus. Nature *583*, 819-824.
Liao, Y., Smyth, G.K., and Shi, W. (2014). featureCounts: an efficient general purpose program for assigning sequence reads to genomic features. Bioinformatics *30*, 923-930.
Liberman, M.C. (1991). Central projections of auditory-nerve fibers of differing spontaneous rate. I. Anteroventral cochlear nucleus. The Journal of comparative neurology *313*, 240-258.
Lin, S., and Xie, R. (2019). Principal Neurons in the Anteroventral Cochlear Nucleus Express Cell-Type Specific Glycine Receptor alpha Subunits. Neuroscience *415*, 77-88.
Lu, H.W., Balmer, T.S., Romero, G.E., and Trussell, L.O. (2017). Slow AMPAR Synaptic Transmission Is Determined by Stargazin and Glutamate Transporters. Neuron *96*, 73-80.e74.
Lu, H.W., Smith, P.H., and Joris, P.X. (2022). Mammalian octopus cells are direction selective to frequency sweeps by excitatory synaptic sequence detection. Proceedings of the National Academy of Sciences of the United States of America *119*, e2203748119.
Lu, T., Rubio, M.E., and Trussell, L.O. (2008). Glycinergic transmission shaped by the corelease of GABA in a mammalian auditory synapse. Neuron *57*, 524-535.

Luecken, M.D., and Theis, F.J. (2019). Current best practices in single-cell RNA-seq analysis: a tutorial. Mol Syst Biol *15*, e8746.
Macosko, E.Z., Basu, A., Satija, R., Nemesh, J., Shekhar, K., Goldman, M., Tirosh, I., Bialas, A.R., Kamitaki, N., Martersteck, E.M.*, et al.* (2015). Highly Parallel Genome-wide Expression Profiling of Individual Cells Using Nanoliter Droplets. Cell *161*, 1202-1214.
Manis, P.B., Kasten, M.R., and Xie, R. (2019). Classification of neurons in the adult mouse cochlear nucleus: Linear discriminant analysis. PLoS One *14*, e0223137.
Manis, P.B., and Marx, S.O. (1991). Outward currents in isolated ventral cochlear nucleus neurons. J Neurosci *11*, 2865-2880.
Martin, M.R. (1981). Morphology of the cochlear nucleus of the normal and reeler mutant mouse. The Journal of comparative neurology *197*, 141-152.
Martin, M.R., and Rickets, C. (1981). Histogenesis of the cochlear nucleus of the mouse. The Journal of comparative neurology *197*, 169-184.
McGinley, M.J., Liberman, M.C., Bal, R., and Oertel, D. (2012). Generating synchrony from the asynchronous: compensation for cochlear traveling wave delays by the dendrites of individual brainstem neurons. J Neurosci *32*, 9301-9311.
McGinley, M.J., and Oertel, D. (2006). Rate thresholds determine the precision of temporal integration in principal cells of the ventral cochlear nucleus. Hear Res *216-217*, 52-63.
Meadows, L.S., Malhotra, J., Loukas, A., Thyagarajan, V., Kazen-Gillespie, K.A., Koopman, M.C., Kriegler, S., Isom, L.L., and Ragsdale, D.S. (2002). Functional and biochemical analysis of a sodium channel beta1 subunit mutation responsible for generalized epilepsy with febrile seizures plus type 1. J Neurosci *22*, 10699-10709.
Mickelsen, L.E., Bolisetty, M., Chimileski, B.R., Fujita, A., Beltrami, E.J., Costanzo, J.T., Naparstek, J.R., Robson, P., and Jackson, A.C. (2019). Single-cell transcriptomic analysis of the lateral hypothalamic area reveals molecularly distinct populations of inhibitory and excitatory neurons. Nat Neurosci *22*, 642-656.
Middlebrooks, J.C., Nick, H.S., Subramony, S.H., Advincula, J., Rosales, R.L., Lee, L.V., Ashizawa, T., and Waters, M.F. (2013). Mutation in the kv3.3 voltage-gated potassium channel causing spinocerebellar ataxia 13 disrupts sound-localization mechanisms. PLoS One *8*, e76749.
Ming Hu, X.J. (2022). PatchView: A Python Package for Patch-clamp Data Analysis and Visualization. Journal of Open Source Software *7*, 4706.
Moosmang, S., Stieber, J., Zong, X., Biel, M., Hofmann, F., and Ludwig, A. (2001). Cellular expression and functional characterization of four hyperpolarization-activated pacemaker channels in cardiac and neuronal tissues. Eur J Biochem *268*, 1646-1652.
Muniak, M.A., Rivas, A., Montey, K.L., May, B.J., Francis, H.W., and Ryugo, D.K. (2013). 3D model of frequency representation in the cochlear nucleus of the CBA/J mouse. Journal of Comparative Neurology *521*, 1510-1532.
Muñoz-Manchado, A.B., Bengtsson Gonzales, C., Zeisel, A., Munguba, H., Bekkouche, B., Skene, N.G., Lönnerberg, P., Ryge, J., Harris, K.D., Linnarsson, S.*, et al.* (2018). Diversity of Interneurons in the Dorsal Striatum Revealed by Single-Cell RNA Sequencing and PatchSeq. Cell Rep *24*, 2179-2190.e2177.
Ngodup, T., Goetz, J.A., McGuire, B.C., Sun, W., Lauer, A.M., and Xu-Friedman, M.A. (2015). Activity-dependent, homeostatic regulation of neurotransmitter release from auditory nerve fibers. Proceedings of the National Academy of Sciences of the United States of America *112*, 6479-6484.
Ngodup, T., Romero, G.E., and Trussell, L.O. (2020). Identification of an inhibitory neuron subtype, the L-stellate cell of the cochlear nucleus. Elife *9*.
Nornes, H.O., and Morita, M. (2011). Time of Origin of the Neurons in the Caudal Brain Stem of Rat: An Autoradiographic Study. Developmental Neuroscience *2*, 101-114.

Oertel, D., McGinley, M., and and Cao, X.-J. (2009). Temporal processing in the auditory pathway. In Encylopedia of Neuroscience.
Oertel, D., Wright, S., Cao, X.J., Ferragamo, M., and Bal, R. (2011). The multiple functions of T stellate/multipolar/chopper cells in the ventral cochlear nucleus. Hear Res *276*, 61-69.
Oertel, D., Wu, S.H., Garb, M.W., and Dizack, C. (1990). Morphology and physiology of cells in slice preparations of the posteroventral cochlear nucleus of mice. The Journal of comparative neurology *295*, 136-154.
Palmer, A.R. (1987). Physiology of the cochlear nerve and cochlear nucleus. British Medical Bulletin *43*, 838-855.
Parpaite, T., Brosse, L., Sejourne, N., Laur, A., Mechioukhi, Y., Delmas, P., and Coste, B. (2021). Patch-seq of mouse DRG neurons reveals candidate genes for specific mechanosensory functions. Cell Rep *37*, 109914.
Perney, T.M., and Kaczmarek, L.K. (1997). Localization of a high threshold potassium channel in the rat cochlear nucleus. The Journal of comparative neurology *386*, 178-202.
Petilla Interneuron Nomenclature, G., Ascoli, G.A., Alonso-Nanclares, L., Anderson, S.A., Barrionuevo, G., Benavides-Piccione, R., Burkhalter, A., Buzsaki, G., Cauli, B., Defelipe, J.*, et al.* (2008). Petilla terminology: nomenclature of features of GABAergic interneurons of the cerebral cortex. Nat Rev Neurosci *9*, 557-568.
Petralia, R.S., Rubio, M.E., Wang, Y.X., and Wenthold, R.J. (2000). Differential distribution of glutamate receptors in the cochlear nuclei. Hear Res *147*, 59-69.
Petralia, R.S., Wang, Y.X., Zhao, H.M., and Wenthold, R.J. (1996). Ionotropic and metabotropic glutamate receptors show unique postsynaptic, presynaptic, and glial localizations in the dorsal cochlear nucleus. The Journal of comparative neurology *372*, 356-383.
Phillips, R.A., 3rd, Tuscher, J.J., Black, S.L., Andraka, E., Fitzgerald, N.D., Ianov, L., and Day, J.J. (2022). An atlas of transcriptionally defined cell populations in the rat ventral tegmental area. Cell Rep *39*, 110616.
Pierce, E.T. (1967). Histogenesis of the dorsal and ventral cochlear nuclei in the mouse. An autoradiographic study. The Journal of comparative neurology *131*, 27-54.
Pliss, L., Yang, H., and Xu-Friedman, M.A. (2009). Context-dependent effects of NMDA receptors on precise timing information at the endbulb of Held in the cochlear nucleus. J Neurophysiol *102*, 2627-2637.
Polański, K., Young, M.D., Miao, Z., Meyer, K.B., Teichmann, S.A., and Park, J.-E. (2019). BBKNN: fast batch alignment of single cell transcriptomes. Bioinformatics *36*, 964-965.
Polleux, F., Morrow, T., and Ghosh, A. (2000). Semaphorin 3A is a chemoattractant for cortical apical dendrites. Nature *404*, 567-573.
Rhode, W.S., and Greenberg, S. (1992). Physiology of the Cochlear Nuclei. In The Mammalian Auditory Pathway: Neurophysiology, A.N. Popper, and R.R. Fay, eds. (New York, NY: Springer New York), pp. 94-152.
Rodrigues, A.R., and Oertel, D. (2006). Hyperpolarization-activated currents regulate excitability in stellate cells of the mammalian ventral cochlear nucleus. J Neurophysiol *95*, 76-87.
Romero, G.E. (2021). CENTRAL CIRCUITRY UNDERLYING THE MEDIAL OLIVOCOCHLEAR EFFERENT SYSTEM. In Department of Physiology & Pharmacology (Oregon Health & Science University School of Medicine).
Roos, M.J., and May, B.J. (2012). Classification of unit types in the anteroventral cochlear nucleus of laboratory mice. Hear Res *289*, 13-26.
Rothman, J.S., and Manis, P.B. (2003). The roles potassium currents play in regulating the electrical activity of ventral cochlear nucleus neurons. J Neurophysiol *89*, 3097-3113.
Rubio, M.E., Matsui, K., Fukazawa, Y., Kamasawa, N., Harada, H., Itakura, M., Molnár, E., Abe, M., Sakimura, K., and Shigemoto, R. (2017). The number and distribution of AMPA receptor channels

containing fast kinetic GluA3 and GluA4 subunits at auditory nerve synapses depend on the target cells. Brain structure & function *222*, 3375-3393.
Rudy, B., and McBain, C.J. (2001). Kv3 channels: voltage-gated K+ channels designed for high-frequency repetitive firing. Trends in Neurosciences *24*, 517-526.
Ryugo, D.K., and Parks, T.N. (2003). Primary innervation of the avian and mammalian cochlear nucleus. Brain research bulletin *60*, 435-456.
Saint Marie, R.L., Benson, C.G., Ostapoff, E.M., and Morest, D.K. (1991). Glycine immunoreactive projections from the dorsal to the anteroventral cochlear nucleus. Hearing Research *51*, 11-28.
Santoro, B., Chen, S., Luthi, A., Pavlidis, P., Shumyatsky, G.P., Tibbs, G.R., and Siegelbaum, S.A. (2000). Molecular and functional heterogeneity of hyperpolarization-activated pacemaker channels in the mouse CNS. J Neurosci *20*, 5264-5275.
Saunders, A., Macosko, E.Z., Wysoker, A., Goldman, M., Krienen, F.M., de Rivera, H., Bien, E., Baum, M., Bortolin, L., Wang, S.*, et al.* (2018). Molecular Diversity and Specializations among the Cells of the Adult Mouse Brain. Cell *174*, 1015-1030.e1016.
Scala, F., Kobak, D., Bernabucci, M., Bernaerts, Y., Cadwell, C.R., Castro, J.R., Hartmanis, L., Jiang, X., Laturnus, S., Miranda, E.*, et al.* (2021). Phenotypic variation of transcriptomic cell types in mouse motor cortex. Nature *598*, 144-150.
Scala, F., Kobak, D., Shan, S., Bernaerts, Y., Laturnus, S., Cadwell, C.R., Hartmanis, L., Castro, J., Tan, Z.H., Sandberg, R.*, et al.* (2018). Neocortical layer 4 in adult mouse differs in major cell types and circuit organization between primary sensory areas. bioRxiv, 507293.
Schweitzer, L., and Cant, N.B. (1985). Differentiation of the giant and fusiform cells in the dorsal cochlear nucleus of the hamster. Brain Res *352*, 69-82.
Shekhar, K., Lapan, S.W., Whitney, I.E., Tran, N.M., Macosko, E.Z., Kowalczyk, M., Adiconis, X., Levin, J.Z., Nemesh, J., Goldman, M.*, et al.* (2016). Comprehensive Classification of Retinal Bipolar Neurons by Single-Cell Transcriptomics. Cell *166*, 1308-1323 e1330.
Shepard, A.R., Scheffel, J.L., and Yu, W.M. (2019). Relationships between neuronal birthdates and tonotopic positions in the mouse cochlear nucleus. The Journal of comparative neurology *527*, 999-1011.
Smith, R.D., and Goldin, A.L. (1998). Functional Analysis of the Rat I Sodium Channel inXenopus Oocytes. The Journal of Neuroscience *18*, 811 - 820.
Stanley, G., Gokce, O., Malenka, R.C., Südhof, T.C., and Quake, S.R. (2020). Continuous and Discrete Neuron Types of the Adult Murine Striatum. Neuron *105*, 688-699.e688.
Szczurkowska, J., Guo, A., Martin, J., Lee, S.I., Martinez, E., Chien, C.T., Khan, T.A., Singh, R., Dadson, D., Tran, T.S.*, et al.* (2022). Semaphorin3A/PlexinA3 association with the Scribble scaffold for cGMP increase is required for apical dendrite development. Cell Rep *38*, 110483.
Tasic, B., Yao, Z., Graybuck, L.T., Smith, K.A., Nguyen, T.N., Bertagnolli, D., Goldy, J., Garren, E., Economo, M.N., Viswanathan, S.*, et al.* (2018). Shared and distinct transcriptomic cell types across neocortical areas. Nature *563*, 72-78.
Tolbert, L.P., Morest, D.K., and Yurgelun-Todd, D.A. (1982). The neuronal architecture of the anteroventral cochlear nucleus of the cat in the region of the cochlear nerve root: horseradish peroxidase labelling of identified cell types. Neuroscience *7*, 3031-3052.
Trussell, L.O. (2019). 123In Vitro Studies of Neuromodulation and Plasticity in the Dorsal Cochlear Nucleus. In The Oxford Handbook of the Auditory Brainstem, K. Kandler, ed. (Oxford University Press), p. 0.
Trussell, L.O., and Oertel, D. (2018). Microcircuits of the Dorsal Cochlear Nucleus. In The Mammalian Auditory Pathways: Synaptic Organization and Microcircuits, D.L. Oliver, N.B. Cant, R.R. Fay, and A.N. Popper, eds. (Cham: Springer International Publishing), pp. 73-99.

Varecka, L., Wu, C.-H., Rotter, A., and Frostholm, A. (1994). GABAA/benzodiazepine receptor α6 subunit mRNA in granule cells of the cerebellar cortex and cochlear nuclei: Expression in developing and mutant mice. Journal of Comparative Neurology *339*, 341-352.
Wang, L.Y., Gan, L., Forsythe, I.D., and Kaczmarek, L.K. (1998a). Contribution of the Kv3.1 potassium channel to high-frequency firing in mouse auditory neurones. The Journal of physiology *509 ( Pt 1)*, 183-194.
Wang, Y.-X., Wenthold, R.J., Ottersen, O.P., and Petralia, R.S. (1998b). Endbulb Synapses in the Anteroventral Cochlear Nucleus Express a Specific Subset of AMPA-Type Glutamate Receptor Subunits. The Journal of Neuroscience *18*, 1148-1160.
Wang, Y., and Manis, P.B. (2006). Temporal coding by cochlear nucleus bushy cells in DBA/2J mice with early onset hearing loss. Journal of the Association for Research in Otolaryngology : JARO *7*, 412-424.
Watanabe, D., Inokawa, H., Hashimoto, K., Suzuki, N., Kano, M., Shigemoto, R., Hirano, T., Toyama, K., Kaneko, S., Yokoi, M.*, et al.* (1998). Ablation of cerebellar Golgi cells disrupts synaptic integration involving GABA inhibition and NMDA receptor activation in motor coordination. Cell *95*, 17-27.
Webster, D.B., and Trune, D.R. (1982). Cochlear nuclear complex of mice. The American journal of anatomy *163*, 103-130.
Wickesberg, R.E., and Oertel, D. (1989). Auditory nerve neurotransmitter acts on a kainate receptor: evidence from intracellular recordings in brain slices from mice. Brain Res *486*, 39-48.
Wickesberg, R.E., and Oertel, D. (1990). Delayed, frequency-specific inhibition in the cochlear nuclei of mice: a mechanism for monaural echo suppression. J Neurosci *10*, 1762-1768.
Wickesberg, R.E., Whitlon, D., and Oertel, D. (1991). Tuberculoventral neurons project to the multipolar cell area but not to the octopus cell area of the posteroventral cochlear nucleus. The Journal of comparative neurology *313*, 457-468.
Wolf, F.A., Angerer, P., and Theis, F.J. (2018). SCANPY: large-scale single-cell gene expression data analysis. Genome Biol *19*, 15.
Wolock, S.L., Lopez, R., and Klein, A.M. (2019). Scrublet: Computational Identification of Cell Doublets in Single-Cell Transcriptomic Data. Cell Syst *8*, 281-291 e289.
Wu, S.H., and Oertel, D. (1984). Intracellular injection with horseradish peroxidase of physiologically characterized stellate and bushy cells in slices of mouse anteroventral cochlear nucleus. J Neurosci *4*, 1577-1588.
Xie, R., and Manis, P.B. (2013). Target-Specific IPSC Kinetics Promote Temporal Processing in Auditory Parallel Pathways. The Journal of Neuroscience *33*, 1598-1614.
Xie, R., and Manis, P.B. (2017). Radiate and Planar Multipolar Neurons of the Mouse Anteroventral Cochlear Nucleus: Intrinsic Excitability and Characterization of their Auditory Nerve Input. Frontiers in neural circuits *11*, 77.
Yaeger, D.B., and Trussell, L.O. (2015). Single granule cells excite Golgi cells and evoke feedback inhibition in the cochlear nucleus. J Neurosci *35*, 4741-4750.
Yang, H., and Xu-Friedman, M.A. (2008). Relative roles of different mechanisms of depression at the mouse endbulb of Held. Journal of neurophysiology *99*, 2510-2521.
Yang, Y., Ramamurthy, B., Neef, A., and Xu-Friedman, M.A. (2016). Low Somatic Sodium Conductance Enhances Action Potential Precision in Time-Coding Auditory Neurons. J Neurosci *36*, 11999-12009.
Yaylaoglu, M.B., Titmus, A., Visel, A., Alvarez-Bolado, G., Thaller, C., and Eichele, G. (2005). Comprehensive expression atlas of fibroblast growth factors and their receptors generated by a novel robotic in situ hybridization platform. Dev Dyn *234*, 371-386.
Yin, T.C.T., Smith, P.H., and Joris, P.X. (2019). Neural Mechanisms of Binaural Processing in the Auditory Brainstem. Comprehensive Physiology *9*, 1503-1575.

Young, E.D. (1998). Parallel processing in the nervous system: evidence from sensory maps. Proceedings of the National Academy of Sciences of the United States of America *95*, 933-934.
Yu, F.H., and Catterall, W.A. (2003). Overview of the voltage-gated sodium channel family. Genome Biol *4*, 207.
Zeilhofer, H.U., Studler, B., Arabadzisz, D., Schweizer, C., Ahmadi, S., Layh, B., Bösl, M.R., and Fritschy, J.M. (2005). Glycinergic neurons expressing enhanced green fluorescent protein in bacterial artificial chromosome transgenic mice. The Journal of comparative neurology *482*, 123-141.
Zeng, H., and Sanes, J.R. (2017). Neuronal cell-type classification: challenges, opportunities and the path forward. Nature Reviews Neuroscience *18*, 530-546.
Zhao, J., O'Leary, M.E., and Chahine, M. (2011). Regulation of Nav1.6 and Nav1.8 peripheral nerve Na+ channels by auxiliary β-subunits. J Neurophysiol *106*, 608-619.
Zhao, Y., Chen, S., Swensen, A.C., Qian, W.J., and Gouaux, E. (2019). Architecture and subunit arrangement of native AMPA receptors elucidated by cryo-EM. Science *364*, 355-362.
Zheleznova, N.N., Sedelnikova, A., and Weiss, D.S. (2009). Function and modulation of delta-containing GABA(A) receptors. Psychoneuroendocrinology *34 Suppl 1*, S67-73.
Zheng, G.X., Terry, J.M., Belgrader, P., Ryvkin, P., Bent, Z.W., Wilson, R., Ziraldo, S.B., Wheeler, T.D., McDermott, G.P., Zhu, J.*, et al.* (2017). Massively parallel digital transcriptional profiling of single cells. Nat Commun *8*, 14049.

## Supplemental materials

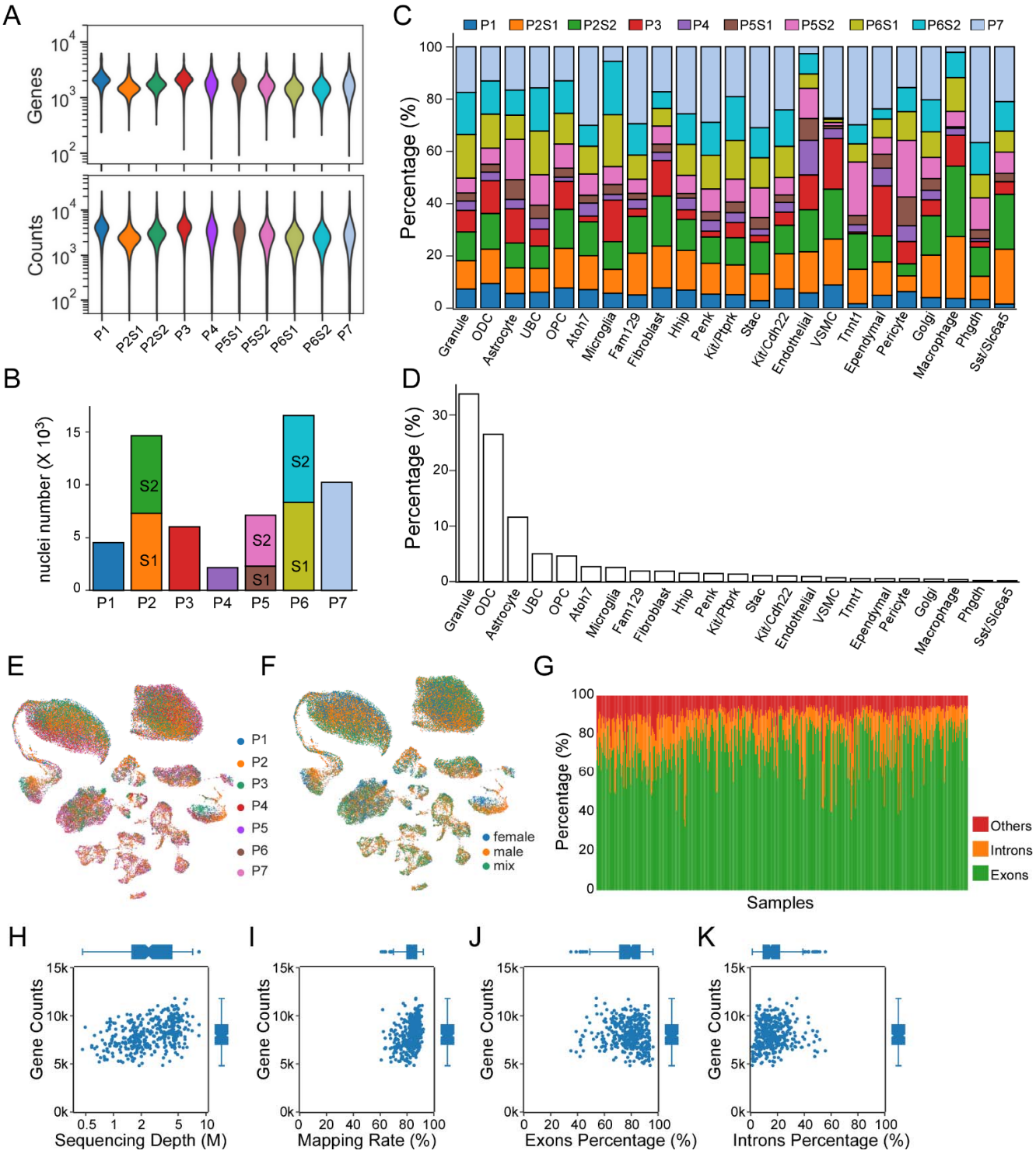


**Data S1. Quality control analysis for snRNA-seq and Patch-seq data. Related to Figures 1-2. (A)** Violin plots of the gene counts (top) and UMI counts (bottom) of each sample sequenced with Drop-seq. P1, P3, P5, P7: the sample from Preparation 1, 3, 5, and 7 respectively. P2S1 and P2S2: Sample 1 and 2 from Preparation 2; P5S1 and P5S2: Sample 1 and 2 from Preparation 5; P6S1 and

P6S2: Sample 1 and 2 from Preparation 6. (**B)** Sample size (the number of nuclei) of each preparation and sample in snRNA-seq. Preparation 2, 5, and 6 has two samples (S1, S2). **(C)** The contribution of each sample (represented as a percentage) to the total population of each cell type (or cluster). See Figure 1 and Figure S1 for annotation of cell types and clusters. **(D)** The proportion of each cell type (or cluster) in the total sequenced population (i.e., combining all samples). **(E)** UMAP visualization of all nuclei from CN, colored by preparations (P1-P7). **(F**) UMAP visualization of all nuclei from CN, colored by gender. **(G)** The proportion of sequencing reads mapped to exons (CDS, 5'UTR, 3'UTR), introns, and other intergenic regions in each Patch-seq cell. As expected, most reads map to exons regions rather than introns and intergenic regions. **(H**) Correlations of gene counts with sequencing depth in Patch-seq cells. **(I)** Correlations of gene counts with STAR mapping rate in Patch-seq cells. **(J)** Correlations of gene counts with the percentage of reads mapped to exons in Patch-seq cells. (**K)** Correlations of gene counts with the percentage of reads mapped to introns in Patch-seq cells.

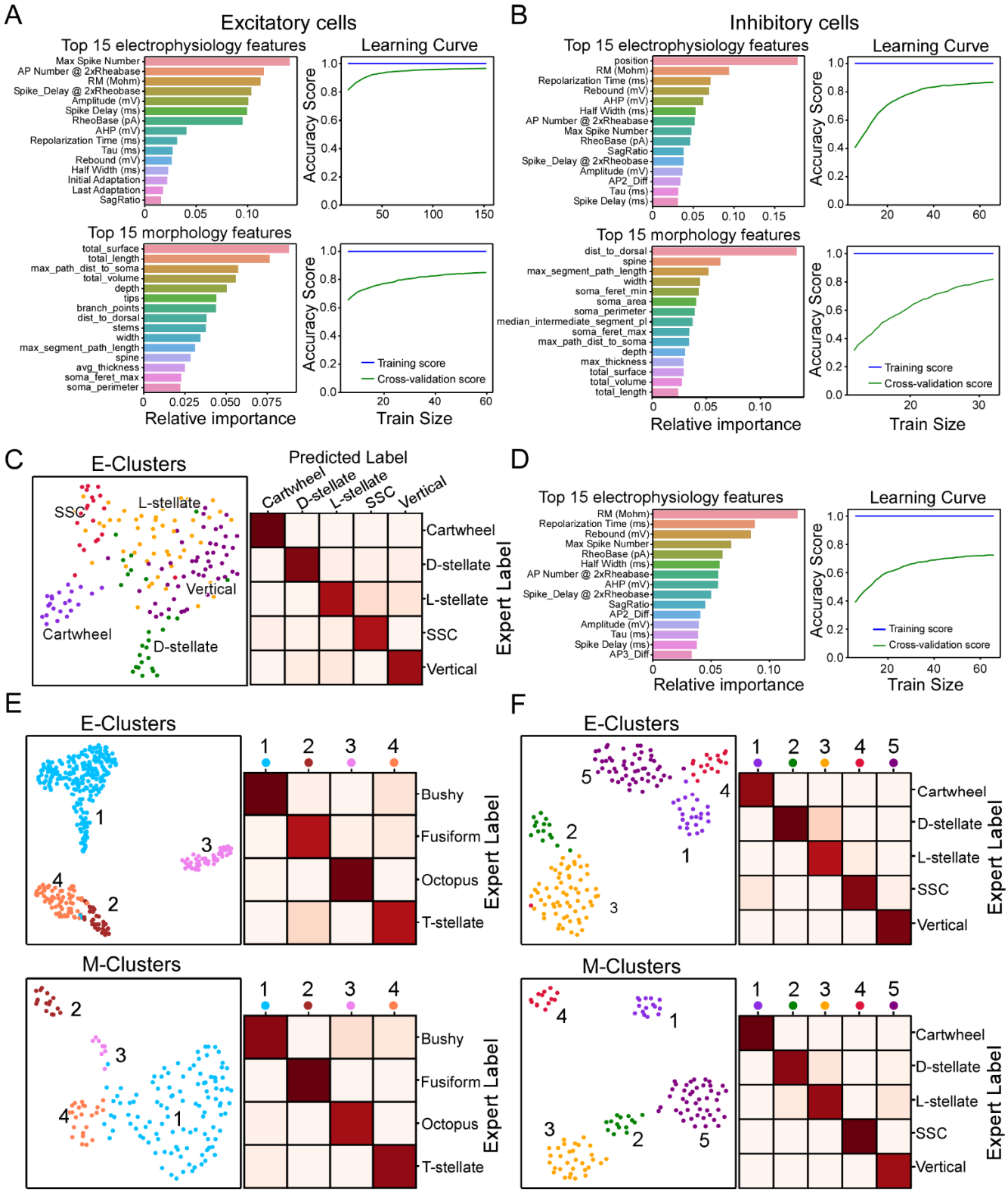


**Data S2. Distinguish cell types by electrophysiological or morphological features. Related to Figure 2**

**(A)** Left: Weights of the top 15 electrophysiological (top) or morphological (bottom) features contributing to the overall performance of the cell type classifier (for excitatory cell types). Right: The performance of the classifier trained with electrophysiological (top) or morphological (bottom) features. Note: its performance improves as the training dataset size increases, indicating a good cell

type classifier. **(B)** Left: Weights of top 15 electrophysiological (top) or morphological (bottom) features contributing to the overall performance of the cell type classifier (for inhibitory cell types). Right: The performance of the classifier trained with electrophysiological (top) or morphological (bottom) features. The performance with electrophysiological features is weighted in with location supervision. **(C)** Left: UMAP visualization of CN inhibitory neurons (n = 163) clustered by selected electrophysiological features (without location supervision). Each cell type is colored as in Figure 2C. Right: Confusion matrix shows the performance (an average of 86.18% accuracy) of the cell-type classifier trained with electrophysiological features only (without location supervision). **(D)** Right: Weights of the top 15 electrophysiology features contributing to the overall performance of the cell-type classifier (for inhibitory cell types). Right: The performance of the classifier trained with electrophysiological features only (without location supervision). **(E)** Top left: UMAP visualization of 404 CN excitatory neurons clustered by selected electrophysiological features, colored by k-means clusters. Top right: Confusion matrix shows the performance of k-means clustering (with electrophysiological features) in distinguishing CN excitatory cell types as labeled manually (an average of 92.33% accuracy). Bottom left: UMAP visualization of 157 CN excitatory neurons clustered by selected morphological features, colored by k-means clusters. Bottom right: Confusion matrix shows the performance of k-means clustering (with morphological features) in distinguishing CN excitatory cell types (an average of 92.99% accuracy). **(F)** Top left: UMAP visualization of 163 CN inhibitory neurons clustered by selected electrophysiological features, colored by k-means clusters. Top right: Confusion matrix shows the performance of k-means clustering (with electrophysiological features) in distinguishing CN inhibitory cell types as labeled manually (an average of 90.18% accuracy). Bottom left: UMAP visualization of 95 CN inhibitory neurons clustered by selected morphological features, colored by k-means clusters. Bottom right: Confusion matrix shows the performance of k-means clustering (with morphological features) in distinguishing CN inhibitory cell types (an average of 90.53% accuracy).

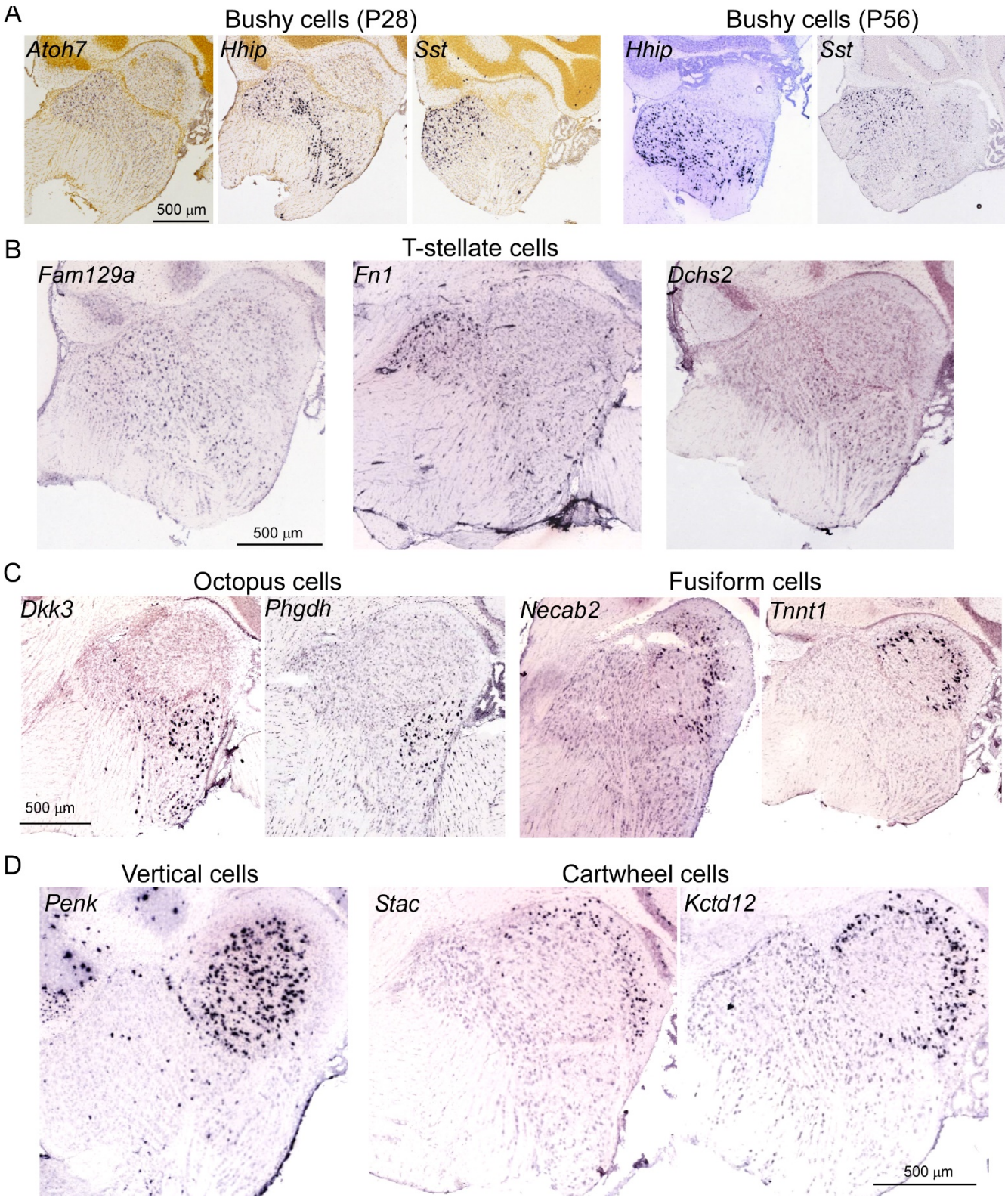


**Data S3. Allen Brain Atlas ISH expression of single discriminatory markers identified for major cell types in the CN. Related to Figures 3-6.**

**(A)** Representative micrographs of ISH expression of single discriminatory markers (*Atoh7*, *Hhip,* and *Sst*) for bushy cell subtypes in sagittal sections containing CN (corresponding to middle CN) at P28 (left) and P56 (right). The expression data of *Atoh7* at P56 are not available. **(B)** Representative micrographs of ISH expression of *Fam129a*, a general discriminatory marker for T-stellate cells

(right), and of the subtype-specific markers (*Fn1* and *Dchs2*) in the CN sagittal sections. **(C)** Representative micrographs of ISH expression of single discriminatory markers (*Dkk3* and *Phgdh*) for octopus cells or single discriminatory markers for fusiform cells (*Necab2* and *Tnnt1*) in the CN sagittal sections. **(D)** Representative micrographs of ISH expression of single discriminatory marker for vertical cells (*Penk*, Left) or for cartwheel cells (*Stac* and *Kctd12*) in CN sagittal sections. Image credit for all ISH images: Allen Institute.

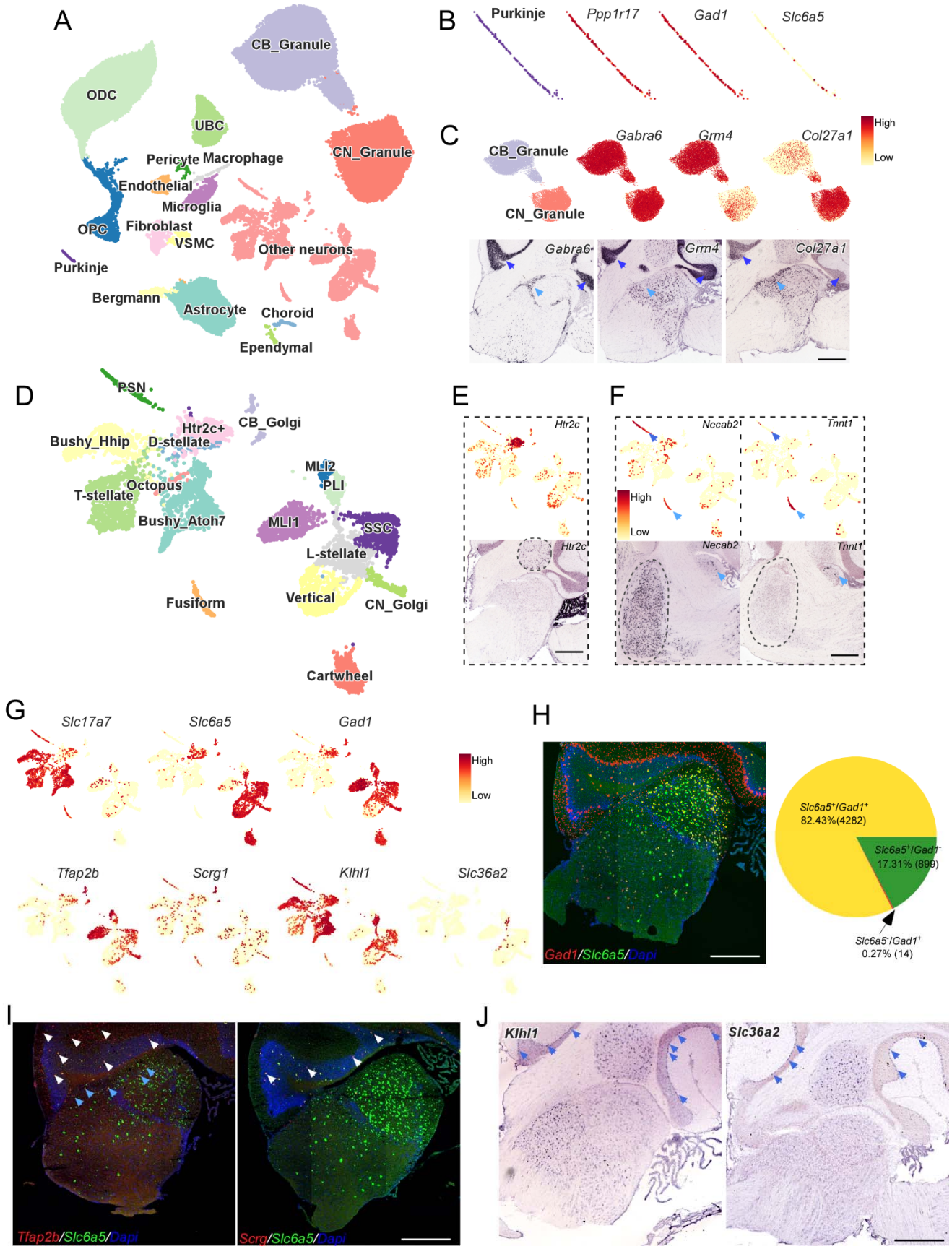


**Method S1. Identification of cell populations from adjoining brain tissues. Related to Figure 1.**

**(A)** UMAP visualization of 93,644 nuclei (after quality control) reveals major cell types and clusters from the cochlear nuclei (CN) and neighboring cerebellum (CB). Cell type and cluster identity is color coded. Identification of cell types and clusters from CB, including cerebellar granule cells (CB_Granule), Purkinje cells, and Bergmann cells was based on their previously-identified molecular signatures (Kozareva et al. 2021) and ISH data from Allen Brain Atlas. **(B)** UMAP visualization of the expression of *Ppp1r17*, *Gad1*, and *Slc6a5* in the cluster as labeled as Purkinje in (A). **(C)** Top: UMAP visualization of the expression of *Gabra6*, *Grm4*, and *Col27a1* in two clusters assigned to granule cells in (A) reveals a granule cell population from CB (CB_Granule) (i.e., *Grm4*$^+$/*Col27a1*$^-$, Kozareva et al. 2021). Bottom: Representative Allen Brain Atlas micrographs of ISH expression of Gabra6, Grm4, and Col27a1 in representative sagittal sections containing the CN and CB indicate that granule cells in CN (CN_Granule ) could be discriminated from CB granule cells (CB_Granule) by their lack of *Grm4* expression. Note: Dark blue arrows point to granule cell layers in CB and light blue arrows point to granule cell layers in CN. Image credit for all ISH images: Allen Institute. **(D)** Subclustering of the neuronal population (except for granule cells and UBC) reveals distinct neuronal clusters from the CN and adjoining regions including CB, the principal sensory nucleus of the trigeminal nerve (PSN), and the dentate nucleus. Cell type and cluster identity is color coded. Identification of neuronal clusters from CB, PSN and the dentate nucleus is based on identified molecular signatures of CB cell types (Kozareva et al. 2021) and ISH data from Allen Brain Atlas. **(E)** Top: UMAP visualization of the expression of *Htr2c* reveals a *Htr2c*-enriched cluster corresponding to cells from the dentate nucleus. Bottom: A representative micrograph (from Allen Brain Atlas) of ISH expression of *Htr2c* in a sagittal section containing CN and CB shows that *Htr2c* expression is restricted to the dentate nucleus (dash circle). **(F)** Top: UMAP visualization of the expression of *Necab2* and *Tnnt1* reveals two *Necab2*-enriched clusters, one of which corresponds to cells from the PSN (*Necab2*$^+$/*Tnnt1*$^-$ cluster). Bottom: Micrograghs of ISH expression of *Necab2* (right) or *Tnnt1* (left) in a sagittal section containing a small region of DCN and PSN show that *Necab2*$^+$/*Tnnt1*$^-$ cells are restricted to the PSN (dash circles), while *Necab2*$^+$/*Tnnt1*$^+$ cells (light blue arrows) are restricted to the DCN (i.e., fusiform cells; see Figure 2) **(G)** UMAP visualization of the expression of gene markers for excitatory neurons (*Slc17a7*), for inhibitory neurons (*Gad1* and *Slc6a5*), for CB interneuron cell types (*Tfap2b*, *Scrg1*, *Klhl1*, and *Slc36a2*) reveals four *Tfap2b*-enriched inhibitory clusters, and one inhibitory cluster co-enriched with Klhl1 and Slc36a2. Two of *Tfap2b*-enriched clusters are pure GABAergic (*Gad1*$^+$/*Slc6a5*$^-$), which correspond to MLI1 and MLI2 from the CB (Kozareva et al. 2021, also see below). The other two *Tfap2b*-enriched are glycine/GABA combinatorial clusters (*Scrg1*$^+$or *Scrg1*$^-$), which correspond to Golgi cells in the CB (CB_Golgi, Kozareva et al. 2021, also see below) and CN (CN_Golgi, also see below). An inhibitory cluster is co-enriched with *Klhl1* and *Slc36a2*, reminiscent of PLI in the CB (Kozareva et al. 2021). **(H)** Left: Double FISH staining of Gad1 and Slc6a5 in a sagittal section containing CN and CB. Right: Pie chart indicates the proportion of pure GABAergic neurons (*Gad1*$^+$/*Slc6a5*$^-$), pure glycinergic neurons (*Gad1*$^-$/*Slc6a5*$^+$), and glycine/GABA neurons (*Gad1*$^+$/*Slc6a5*$^+$). Note: *Gad1*$^+$/*Slc6a5*$^-$ neurons in the CN are absent or very sparse. **(I)** Double FISH staining of Golgi cell marker gene (*Tfap2b* or *Scrg1*) and *Slc6a5* in representative sagittal sections containing CN and CB. Note: *Scrg1* expression is restricted to the CB. White arrows indicate the gene expression in CB and light blue arrows indicate the expression in CN. **(J)** Representative micrographs (from Allen Brain Atlas) of ISH expression of *Klhl1* and *Slc36a2* (CB PLI marker gene) in the sagittal section containing the CN and CB. Note: *Slc36a2* is not expressed in CN. Arrows indicate the gene expression in CB Purkinje cell layer.

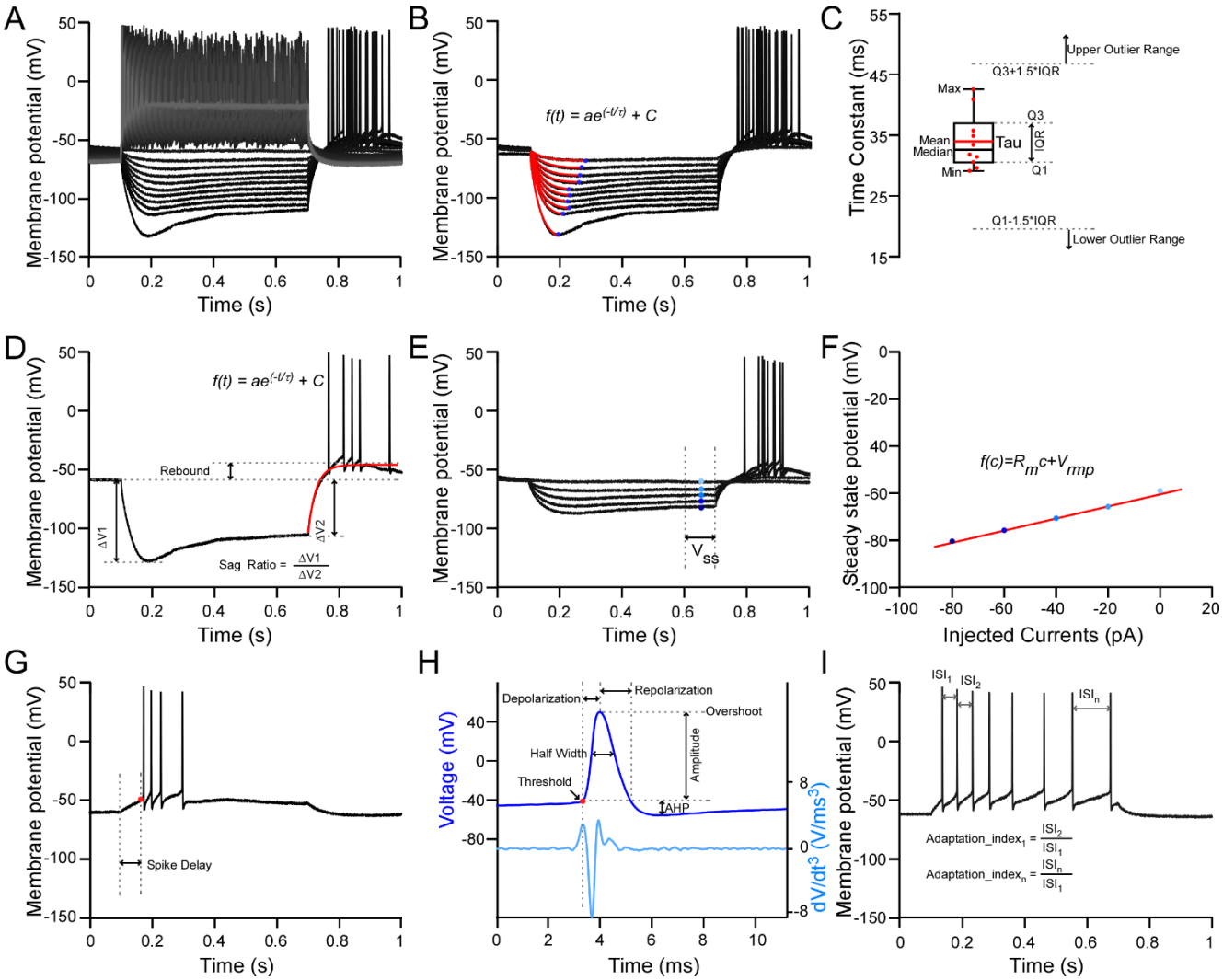


**Method S2. Extraction of the electrophysiological features. Related to Figures 2, 4-6**
(**A**) Membrane potential responses of an example neuron to the consecutive step current injections. (**B**) A series of membrane potential traces in response to hyperpolarizing current steps are fitted with an exponential function. The tau (t) is calculated for each trace. (**C**) A box plot shows a series of Tau values from one sample neuron, including maximum (Max), minimum (Min), mean, median, the first quartile (Q1), the third quartile (Q3), the interquartile range (IQR) values. The Tau values falling above the upper range (> Q3+1.5*IQR) or below the low range (< Q1-1.5*IQR) are considered outliers and removed before averaging for the mean value. (**D**) The first hyperpolarizing trace in the step protocol is used to calculate the sag ratio and rebound voltage as shown with inset equations. (**E**) The membrane potential responses to the last five negative current injections in the step protocol. The steady-state potential for each trace ($V_{ss}$) is indicated with dash lines. (**F**) The steady-state potentials ($V_{ss}$) are fitted with a linear function by the injected currents. The rest membrane potential ($V_{rmp}$) and input resistance ($R_m$) are calculated with the inset equation. (**G**) A representative trace with action potentials (AP) evoked during consecutive step current injections. Spike delay is defined as a time duration between two dash lines. (**H**) A representative AP trace (top) and its third derivative ($dV/dt^3$, bottom). The AP threshold is the membrane potential where the third derivative of the AP trace is maximal, as indicated with a red dot. AP depolarization time, AP amplitude, AP repolarization time, AP half-width, and the afterhyperpolarization (AHP) amplitude are defined as shown with double-arrow lines and dash lines. (**I**) The membrane potential trace in response to 2X rheobase current

injection. The initial (adaptation_index1) and last adaptation index (adaptation_index2) are calculated with inset equations after the interspike interval (ISI) between each AP is determined.

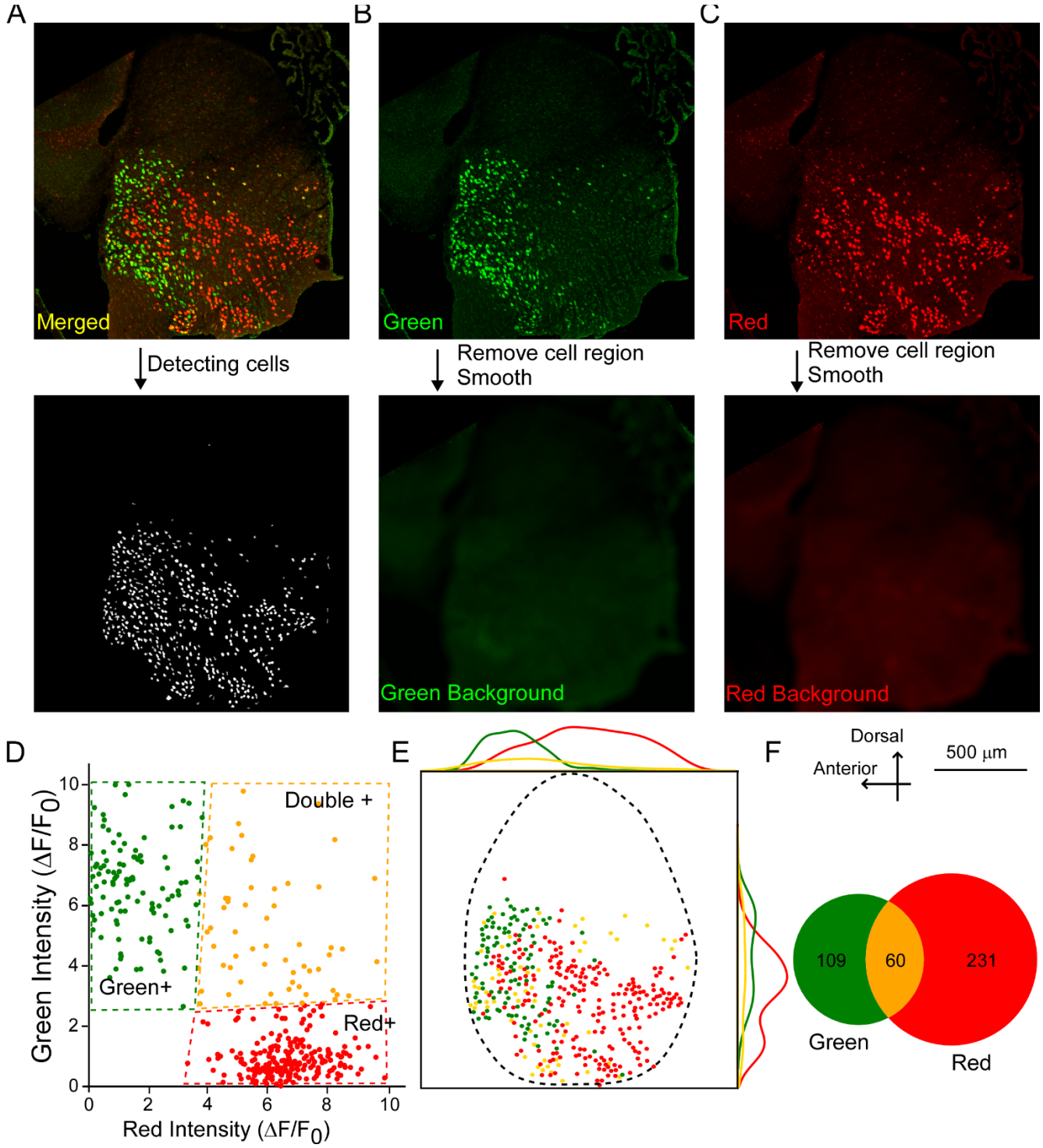


**Method S3. Analysis of dual-color fluorescence in situ hybridization (FISH). Related to Figures 3-6**

(**A**) Top: A representative dual-color FISH staining image (merged). Green channel represents the FITC-labeled RNA probe and red channel represents the DIG-labeled RNA probe. Bottom: each cell with green and/or red signals (F) is detected with a custom-made IDL code, as indicated with a white dot. (**B**) Top: A green signal-only image. Bottom: the image indicates the background green signals (Green $F_0$), derived by subtracting the signals of detected cells from the images on the top, smoothed by a 60 μm length window. (**C**) Top: A red signal-only image. Bottom: the image indicates the background red signals (Red $F_0$), derived by subtracting the signals of detected cells from the images

on the top, smoothed by a 60 μm length window. (**D**) A 2-D scatter plot: the intensity differences ($\Delta F$) between F and $F_0$ divided by $F_0$ of a detected cell from one channel ($\Delta F/F_0$) are plotted against $\Delta F/F_0$ from another channel. Quadrilateral gates are drawn on the plot to determine whether a cell was single-labeled or double-labeled. (**E**) Each identified cells ($Red^+$, $Green^+$, or $Double^+$) in their real CN anatomic location, and 2-D density histograms are plotted through the anterior to posterior and dorsal to the ventral axis to show the distribution of $Red^+$, $Green^+$, and $Double^+$ cells along the two axes. (**F**) Venn diagrams show the number of $Red^+$, $Green^+$, and $Double^+$ cells in the images shown in A.